In-Situ Gamma-Ray Spectrometry and Associated Radiometric Assessment of the Mrima-Kiruku Complex (Kenya) High Background Radiation Anomaly

by

Muchai Ian Kaniu

A Thesis Submitted in Fulfilment of the Requirements for Award of the Degree of Doctor of Philosophy in Physics of the University of Nairobi.

Declaration

I declare that this thesis is my original work and has not been submitted elsewhere for examination, award of a degree or publication. Where other people's work or my own work has been used, this has properly been acknowledged and referenced in accordance with the University of Nairobi's policy requirements.

Signature: _____ Date: _____

Muchai Ian Kaniu
I80/93083/2013
Department of Physics
School of Physical Sciences
University of Nairobi.

This thesis is submitted for examination with our approval as research supervisors:

	Signature:	Date:
Dr. Angeyo H. Kalambuka Department of Physics University of Nairobi.	_____	_____
Dr. Iain G. Darby Nuclear Applications, Physics Section International Atomic Energy Agency Vienna, Austria.	_____	_____
Prof. Lavi M. Muia Department of Physics and Space Science Technical University of Kenya.	_____	_____

"*Strange and varied are the ways of life, and stranger still are the way of Infinite Intelligence, through which men are sometimes forced to undergo all sorts of punishment before discovering their own brains, and their own capacity to create useful ideas through imagination.*" - Napoleon Hill

This thesis is dedicated to my mum, Jane Nancy Wangare and immediate relatives, Mr & Mrs T. K. Mutiso. In appreciation for their unwavering and loving support.

Acknowledgements

The work embodied herein lays to rest a consistently challenging yet self-rewarding experience. For this I thank the Almighty God for giving me the strength and passion throughout the period this work was undertaken.

I wish to express my heartfelt gratitude foremost to Dr. H. K. Angeyo, for his proposal of the topic of present study, and the immense intellectual guidance that he exhibited in working on it with me. I remain eternally indebted to his quality mentorship, which stands in its own class. Next in the same connection I wish to thank Dr. I. G. Darby, for accommodating me into his research group and graciously giving full access to radiometric and associated instruments, his relentless support and supervision, not to mention his expert comments and advice throughout the course of this work - I will forever be in his intellectual debt. Many thanks also go to Prof. L. M. Muia for his guidance and useful suggestions throughout the course of the research.

I would be remiss if I did not acknowledge the IAEA/ICTP sandwich training educational programme (STEP) fellowship award and internship at the IAEA Nuclear Science and Instrumentation Laboratory (NSIL) which enabled the timely completion of this work. I owe a debt of gratitude to Prof. Dr. Ralf Kaiser, IAEA Physics Section Head for a lot of support in my research work not least administrative. Many thanks to Mrs. Rosmery Duran, Mr. Mladen Bogovac, Drs. Milan Matos, Alessandro Milgoiri, Roman Padilla and Janos Osan of the NSIL, and Marcel Ohera of Envinet - for their technical assistance throughout the time I pitched camp in the labs.

I wish to also thank the Chairman and administrative staff of the Department of Physics, University of Nairobi for their support during the period this study was undertaken. I am greatly indebted to the International Science Program (ISP) for generously sponsoring part of the field work activities undertaken in this study. I thank the Kwale County Commissioner's office for administrative support and facilitation during the field work activities conducted in June 2014.

Special thanks to my fellow physics PhD student at NSIL, Akmal Safarov of the Samarkand State University, Uzbekistan, and NSIL interns Tsegah Belacheow, Phillip Ortega and Robert Zedric, for their helpful ideas and suggestions, and more importantly, for making life exciting and worthwhile at the NSIL grad room.

Last but not least, I doubt that the successful completion of my studies would have been possible without the encouragement, prayers and support of my family.

Abstract

The Mrima-Kiruku complex of south coastal Kenya is highly heterogeneous in terms of the underlying geology, mineralogy and topography. It is hypothesized to have a unique rock-modulated high background radiation (HBR) anomaly that is attributable to presence of deeply weathered carbonatite rocks with elevated concentrations of thorium-rich monazite and pyrochlore minerals. There are also a number of ongoing human activities such as mining, land cultivation, hand dug wells and settlement at the foothills of both Mrima and Kiruku Hills that are local occupations for which radiation exposure risk needs to be assessed. This study presents the results of a wide-ranging *in-situ* (carborne and mobile backpack) $\gamma-$ray spectrometric survey conducted in the Mrima-Kiruku complex and the adjoining environs to determine radioactivity levels and assess the radiation exposure as well as associated radiological risk factors. Energy dispersive X-ray fluorescence spectrometric analysis of selected surface soil samples for elemental concentrations was performed in order to compliment the *in-situ* measurements and to enable ascertain the mineralogy of the study area. In addition, the principal component analysis technique and ternary plots were used to assess the variability of *in-situ* radiometric measurements in the study area. The absorbed dose-rates measured in air were found to range $<$ 60 - 2368 nGy h^{-1}. It was observed that ^{232}Th is generally abundant in the complex compared to ^{40}K and ^{238}U: The mean activity concentrations of ^{40}K, ^{238}U and ^{232}Th in the surveyed areas ranged $<$ 202 - 603$\pm$28, 54$\pm$7 - 900$\pm$20 Bq kg^{-1} and 54$\pm$8 - 1817$\pm$51 Bq kg^{-1}, respectively. Correlation analysis of the measured activity concentration values and absorbed gamma dose-rates indicated that the anomalous gamma dose-rate values are due to elevated levels of

^{238}U and ^{232}Th associated with murram roadbeds underlying the south coast road and the side-road intersections from Gazi (Mukurumudzi river bridge approach) to the Menzamwenye road junction (past Mrima TM center), and elevated levels of ^{232}Th associated with the soil and rocks of the Mrima-Kiruku complex. A high correlation of monazite constituent elements, namely Ce, La, Nd and Th was found between the south coast paved road shoulder and Mrima foothills soil samples which indicates that the murram used in paving the south coast road could have originated from the Mrima Hill area. From an external dose perspective, it was concluded that there is significant radiological hazard (> 1 mSv/y) to merchants operating businesses in NORM enhanced areas along the south coast paved road, as well as inhabitants of the Mrima-Kiruku complex area, particularly those who reside at the foothills of both Mrima and Kiruku Hills. It was also concluded that the spatial variability of the HBR anomaly in the Mrima-Kiruku complex and adjoining environs is mainly constrained by anthropogenic activities, underlying geology and geochemical processes in the terrestrial environment. The findings of this work are useful to inform radio-protection policy and regulatory framework for both public and occupational exposures associated with high background radiation areas in Kenya.

Contents

List of Figures

List of Tables

Acronyms and Abbreviations

ADC	analog to digital converter
AEDE	annual effective dose estimate
ASL	above sea level
BDL	below detection limit
cps	counts per second
CRM	certified reference material
DL	detection limit
ECLR	excess lifetime cancer risk
EDA	exploratory data analysis
EDXRF	energy dispersive X-ray fluorescence
eTh	equivalent thorium
eU	equivalent uranium
FSA	full spectrum analysis
GIS	geographic information system
GPS	global positioning system
HBR	high background radiation
HBRA	high background radiation area
HOPG	highly oriented pyrolytic graphite
HPGe	high purity germanium
IAEA	International Atomic Energy Agency
ICRP	International Centre for Radiation Protection
ICTP	International Centre for Theoretical Physics

LREE	light rare earth elements
MAD	median absolute deviation
MCA	multi-channel analyzer
MDA	minimum detectable activities
NaI(Tl)	thallium doped sodium iodide
NCRP	National Council on Radiation Protection & Measurements
NORM	naturally occuring radioactive material
PC	principal component
PCA	principal component analysis
PEI	Pico Envirotec Inc.
PMT	photomultiplier tube
ppb	parts per billion
ppm	parts per million
REE	rare earth elements
ROS	regression on order statistics
RSD	relative standard deviation
SARM	South African Reference Materials
SD	standard deviation
SNR	signal to noise ratio
TENORM	technologically enhanced NORM
TM	(Mrima Hill) Tractor Machinery
UNSCEAR	United Nations Scientific Committee on the Effects of Atomic Radiation
USGS	United States Geological Survey
XRF	X-ray fluorescence

Chapter 1

Introduction

1.1 Environmental gamma-ray spectroscopy

Gamma-ray spectroscopic measurements of environmental radioactivity are important in radiological and geogenic studies but challenging mainly due to the complexity in the composition of the radionuclides (primordial, anthropogenic, cosmogenic) and low radiation field intensities (NCRP, 1976). There is also a significant contribution of background radiation (from terrestrial sources, detector and shielding materials, cosmic rays interactions, and instrumental noise) which reduces the photon signal to noise ratio, lowering the quantitative accuracy of determining concentrations of environmental radionuclides by γ-ray spectroscopy (L'Annunziata, 2003; Gilmore, 2008).

Other factors that complicate the measurements include Compton scatter, spectral interference due to coincident summing and pile-up effects as well as geometrical efficiency limitations. As a result, counting times are extended and thus the analyses have long turn-around times. Furthermore, the interpretation and analysis of acquired spectra is time consuming due to complexities in spectral decomposition. High efficiency gamma detectors such as NaI(Tl) are mostly used to maximize sensitivity. However, the relatively high Compton continuum, presence of coincidence photo-peaks and low resolution result in interference with the detection of low-energy photons (< 500 keV). The HPGe detector in most cases affords the required high photo-peak resolution

especially at low energies but has lower efficiency, and also suffers from Compton scatter interference and high background (Debertin and Helmer, 1988).

In contrast to laboratory based (*ex-situ*) γ-ray spectrometry, where a soil/rock sample representing a few square centimeters is measured, *in-situ* γ-ray spectrometry measurements are carried out with a portable detector placed approximately 1 m above the ground surface. The radioactivity measured in this case is typically within a 10 m radius and 30 cm depth, depending on the detector crystal size, gamma energy and distribution of radioactivity on the ground surface (Beck *et al.*, 1972; Miller and Shebell, 1993; ICRU, 1994). This represents a relatively large volume source compared to a typical soil sample, and comparable counting statistics can be obtained in a small fraction of the time required for the *ex-situ* analysis. Furthermore, the high spatial resolution realized in the measurements enables the assessment of environmental radioactivity in greater detail and precision, as well as its geospatial mapping (IAEA, 2003; Beamish, 2016).

1.2 The high background radiation anomaly in the Mrima-Kiruku complex

The alkaline igneous complex of Jombo in south coastal Kenya consists of the main intrusion at Jombo Hill, three associated satellite intrusions at Mrima, Kiruku and Nguluku, and several dykes (Baker, 1953), as shown in Fig. 1.1. The complex is characterized by a number of rock formations such as alkaline, igneous, and sedimentary rocks of the Duruma sandstone series (Fig. 1.1). It is also naturally rich in Fe, Mn, Nb and many REE which are closely associated with U and Th bearing minerals, namely monazite and pyrochlore (Loupekine, 1968; Horkel *et al.*, 1984; Mangala, 1987). Detailed description of the soil and rocks of the complex is given by Baker (1953) and JICA (1993).

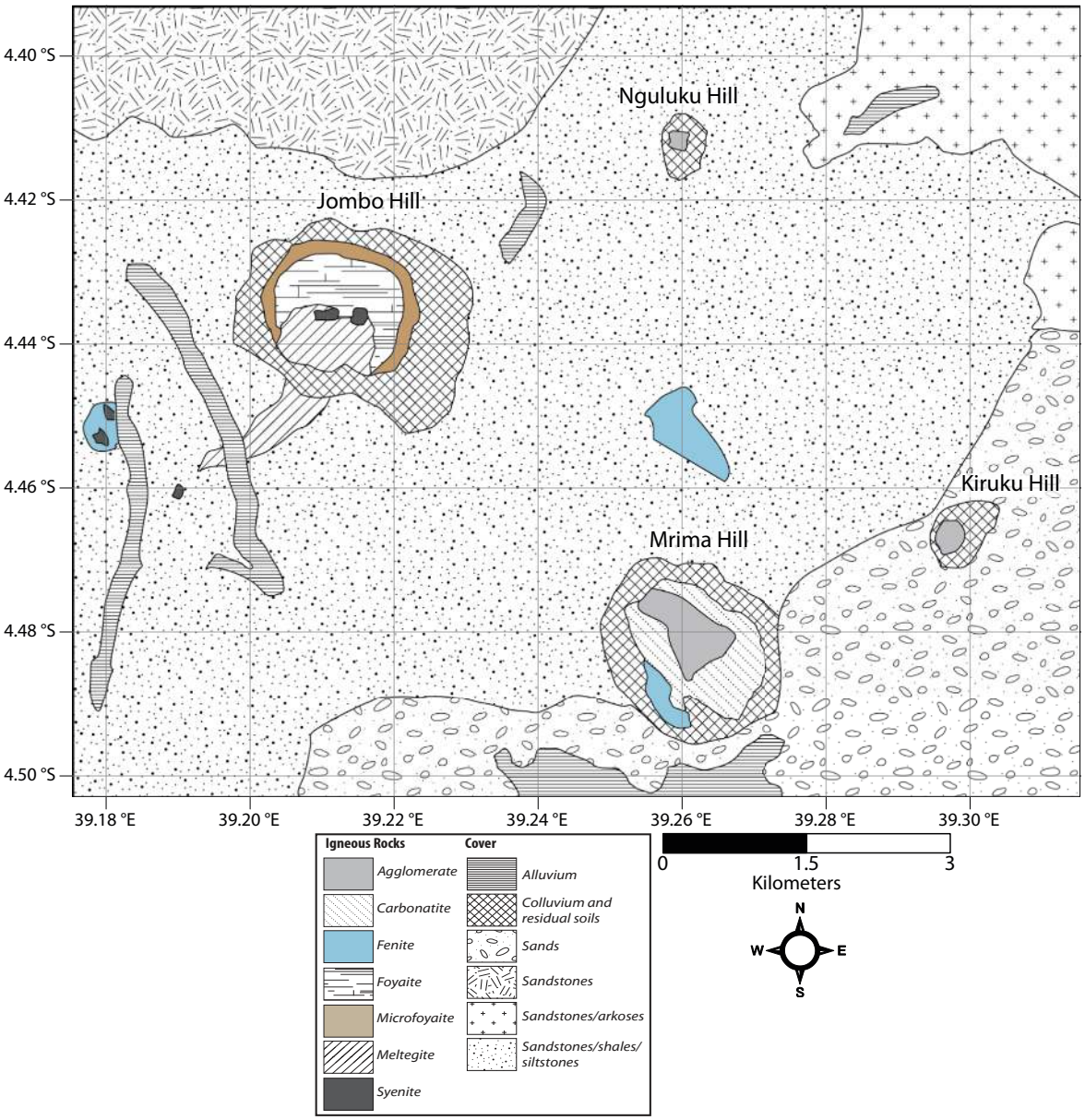

Fig. 1.1: Map indicating the geology of the alkaline igneous complex of Jombo (adapted from: JICA (1993)).

The elevated background radiation in Mrima Hill is attributed to presence of deeply weathered carbonatite rock with high concentrations of thorium-rich monazite and pyrochlore minerals (Baker, 1953; Patel, 1991; Mustapha, 1999). Preliminary estimation of absorbed dose-rates in air in Mrima Hill found 200 - 14,000 nGy h^{-1} (Patel, 1991), which is approximately up to 233 times higher compared to the world population weighted average value of 60 nGy h^{-1} (UNSCEAR, 2000). In a later study, soil samples

from villages surrounding Mrima Hill were analyzed in order to determine the natural radioactivity levels and absorbed dose-rates in air. The average activity concentrations for ^{40}K, ^{238}U and ^{232}Th were 805±21, 207±11 and 501±20 Bq kg^{-1}, respectively and average absorbed dose-rate value reported was 441±17 nGy h^{-1} (Kebwaro *et al.*, 2011). These values were found to be above the world population weighted averages, and higher than values reported in related studies (Hashim *et al.*, 2004; Maina, 2008; Osoro *et al.*, 2011) within the region.

In view of the elevated radiation exposure levels in Mrima Hill and its surroundings, more research is required in the area and the wider Jombo complex so as to assess the environmental and human health risks associated with potential naturally occurring radioactive materials (NORM) contamination. Moreover, there are also a number of human activities such as land cultivation, hand dug wells and settlement at the foothills of the Jombo, Mrima, Kiruku and Nguluku Hills that are local occupations for which radiation exposure risk and radiological hazards need to be assessed. Recently, several mineral prospecting activities for Nb and REE have been re-initiated in the complex as a follow up to JICA (1993). However commercial mining has not been actualized mainly due to the in-homogeneity of the mineral ores as a result of alteration caused by weathering and mineralization (Baker, 1953; Loupekine, 1968).

In the context of this thesis, only the Mrima and Kiruku Hills and adjoining environments were studied. Mrima Hill, located at 4° 29'10" S; 39° 15'10" E, 323 m ASL and approximately 80 km south-west of the port city of Mombasa, is the carbonatite portion of the complex and lies about 8 km south-east of Jombo. It is a broad dome-shaped hill approximately 3.8 km^2 in area, and is covered by undergrowth and dense tropical forest. Kiruku Hill located at 4° 28'1" S; 39° 17'44" E, 167 m ASL is a carbonitized-agglomerate intrusion and lies about 5 km north-east of Mrima Hill. It is a conical-shaped hill approximately 0.3 km^2 in area, and is covered by thick vegetation.

1.3 Research hypothesis

The elevated natural background radiation in the Mrima-Kiruku complex of south coastal Kenya is a high background radiation anomaly that is both constrained and modulated by the underlying deeply weathered carbonatite geological and mineralogical structure as well as anthropogenic activities, namely mining, land cultivation and hand-dug wells. This anomaly (and its radiative field characteristics) is feasible to quantitatively delineate and better geo-spatially delineate.

1.4 Statement of the research problem

Accurate measurement and evaluation of ionizing radiation in the Mrima-Kiruku complex high background radiation anomaly is necessary to among other reasons, establish the base-line values for radioactivity levels and assess radiological hazards associated with the elevated radiation exposure. *In-situ* γ-ray spectrometry offers a low-cost and spatially representative method for rapid assessment of radioactivity levels and exposure in such rugged terrestrial environments compared to *ex-situ* analysis techniques that have so far been employed in the area.

1.5 Objectives of the research

1.5.1 General objective

The goal of this work was to determine radioactivity levels and assess radiation exposure and associated radiological risk factors in the Mrima-Kiruku complex and adjoining environs using *in-situ* γ-ray spectrometry and associated radiometric techniques.

1.5.2 Specific objectives

(i) To perform *in-situ* (carborne and mobile backpack) γ-ray spectrometric measurements and spatial mapping in the Mrima-Kiruku complex and adjoining environs utilizing GPS equipped portable NaI(Tl) detectors and GIS software.

(ii) To determine the activity concentrations of ^{40}K, ^{238}U and ^{232}Th and assess external exposure levels as well as associated radiological risk factors.

(iii) To perform sampling of geological matrices from selected gamma radiation hotspots and undertake laboratory EDXRF analysis in order to ascertain mineralogy of the study area in relation to that obtained using *in-situ* radiometric measurements.

(iv) To utilize multivariate data analysis techniques to assess the variability of natural radionuclide concentrations using the data obtained from specific objectives (i) and (ii).

1.6 Significance and justification of the research

Although high background levels of natural radioactivity have been reported in and around the Mrima Hill, no extensive and systematic investigations have been carried out so far in the area and the wider Jombo complex to ascertain and resolve the spatial variability of elevated radiation exposure and natural radioactivity levels in terms of topography, mineralogy and geology, etc.

In addition to variability of geology and topography associated with the Mrima-Kiruku complex, human activities such as land cultivation, hand dug wells and mining make the accurate radiogenic and radiological characterization of the complex challenging. The present work was undertaken to ultimately assess and understand the occurrence, levels and distribution pattern of ionizing radiation and establish base-line levels of natural radionuclides in the Mrima-Kiruku complex and adjoining environs, utilizing *in-situ* γ-ray spectrometry and associated radiometric measurements (EDXRF spectrometry).

1.7 Thesis structure

The work presented in this thesis is as follows: Chapter 2 provides a summary of literature review allied to the occurrence and distribution of NORM in the terrestrial environment, utility of *in-situ* γ-ray spectrometry in environmental radioactivity monitoring, and the potential application of exploratory data analysis techniques in the multivariate assessment of *in-situ* radiometric measurements. Chapter 3 provides a theoretical background on radioactive decay series and mechanisms for photon interaction with matter as well as an overview of gamma and X-ray spectrometry principles. Chapter 4 describes the experimental procedure for *in-situ* γ-ray spectrometric measurements, laboratory EDXRF analysis of field samples and data analysis techniques employed. Chapter 5 provides the results and discussion of the *in-situ* γ-ray and EDXRF spectrometric measurements, and multivariate analysis of the measured natural radionuclide concentrations. Chapter 6 provides a summary of the study together with the conclusions and recommendations. Supplementary data used in the study and pictorial representations are provided in the appendices.

Chapter 2

Literature Review

This chapter discusses the occurrence of NORM and factors which are responsible for their anomalous distribution in the terrestrial environment. The application of *in-situ* γ-ray spectrometry in the survey of gamma radiation exposure and assessment of NORM, is also discussed. In the end, utility of multivariate exploratory data analysis techniques in the assessment of NORM is explained.

2.1 Occurrence and distribution of NORM in the terrestrial environment

The greatest contribution (approximately 80%) to ionizing radiation exposure comes from natural background; the world average annual effective dose from exposure to natural sources of radiation is 2.4 mSv (UNSCEAR, 2008). This radiation originates from cosmic rays, cosmogenic radionuclides in the ambient atmosphere and NORM. Human exposure to NORM in the environment (indoors and outdoors) is approximately 16% of the annual ionizing radiation exposure and derives primarily from primordial radionuclides in the earth's crust, namely ^{40}K and radioactive progenies of the ^{238}U and ^{232}Th decay series, and radon in air and water. The ICRP recommended dose limits are normally implemented by national regulatory authorities with the aim of controlling human exposure to natural sources of ionizing radiation (ICRP, 2007).

Levels of NORM in the terrestrial environment depend on the distribution of rocks and soil from which they originate and the processes which concentrate and immobilize them. The composition of NORM in soil should ideally correspond to that of the original underlying parent rock. However, this is usually not the case. This is due to geochemical processes such as weathering and erosion which normally cause enhancement and redistribution of NORM, and disequilibrium in the U decay series (Navas *et al.*, 2011). An informative view of immobilization of U in the environment may be found elsewhere (IAEA, 1990). The distribution of NORM may also be varied due to lithological changes, soil pedogenesis and mineralization (Dickson and Scott, 1997).

2.1.1 Radioactivity anomalies in the terrestrial environment

The worldwide average values for outdoor and indoor gamma dose-rates are 60 and 84 nGy h^{-1}, while worldwide average concentration values for ^{40}K, ^{238}U and ^{232}Th in soil are 420, 33 and 45 Bq kg^{-1}, respectively. The average annual effective dose estimate related to indoor and outdoor occupancy is 0.41 and 0.07 mSv, respectively (UNSCEAR, 2000). However around the world there are some areas with elevated levels of NORM and where inhabitants are continuously exposed to relatively high doses; these areas are known as high background radiation areas (HBRA) (Eisenbud and Gesell, 1997).

Investigation of NORM levels in and around HBRA is thus necessary to among other goals, establish the base-line values for NORM and assess environmental and human health risks associated with the elevated radiation exposure. In addition, anthropogenic activities related for instance to quarrying, energy production from coal and geothermal, U and Th mining, production and use of phosphate fertilizers, use of stones and bricks as building materials, etc could lead to enhancement of NORM levels and consequently radiation exposure in the environment (Melville *et al.*, 1981; Landa, 2007; Okeji *et al.*, 2012; Ćujić *et al.*, 2015). In such cases, this becomes known as technologically enhanced naturally occurring radioactive materials (TENORM) (Landa, 2007).

The various exposure and transfer pathways of TENORM in the environment together with the associated radiological impacts on humans have been presented in detail by O'Brien and Cooper (1998). Furthermore, an informative view of the typical volumes of NORM waste generated from such technological processes, the potential environmental and regulatory implications as well as recommendations for NORM waste disposal and remediation of contaminated sites, are given elsewhere (Paschoa, 1998; van Velzen, 2015).

2.1.2 High background radiation anomalies in Kenya and elsewhere

There are several HBRA in Kenya such as Mrima Hill (Patel, 1991; Mustapha, 1999), Gwasi (Achola, 2009), Mt. Homa (Otwoma, 2012), Ruri Hills, Homa Bay (Winnam Gulf), Tinderet and Koru. In these areas, the HBR anomaly is mostly attributed to deeply weathered sedimentary formations, which contain elevated levels of U and Th. Most of the available information on these HBRA is derived from geological and mineral exploration surveys (Caswell, 1953; Baker, 1953; McCall, 1958; Binge *et al.*, 1966; Loupekine, 1968; Horkel *et al.*, 1984; JICA, 1993). However, hardly has this HBR anomaly been systematically assessed and delineated with regard to the spatial, geological, geochemical as well as anthropogenic variability and co-dependencies.

Elevated natural radiation exposure levels have also been reported in a number of countries around the world such as Guarapari in Brazil (Cullen and Franca, 1977), Yangjiang in China (Luxin *et al.*, 1990), Kerala in India (Sunta, 1993) and Ramsar in Iran (Sohrabi, 1993). In the case of Ramsar for instance, annual effective doses reported are as high as 132 mGy/y, which is approximately 55 times higher than the world average. The high background radiation levels in this case are mainly due to enhanced ^{226}Ra concentrations and its decay products in hot springs around Ramsar. A comprehensive review of worldwide radiological studies in HBRA as well as criteria used in their classification can be found elsewhere (Sohrabi, 1998, 2013).

2.2 Application of *in-situ* gamma-ray spectrometry for environmental radioactivity monitoring

The collection of environmental samples, test sample preparations and *ex-situ* analysis for environmental radioactivity estimation can be time consuming and costly. *In-situ* γ-ray spectrometry is more applicable for this task as the gamma radiation is representative of a large area, thus source in-homogeneities are integrated, and analysis results are instantaneous. The method is therefore considered to be more sensitive, spatially representative, rapid and less costly compared to *ex-situ* analysis (Beck *et al.*, 1972). Nevertheless, *ex-situ* γ-ray spectrometry measurements are usually considered to be more reliable than *in-situ* measurements (Rostron *et al.*, 2014). This is because samples are processed and measured in reproducible geometries and controlled environment. Analytical uncertainties for *in-situ* measurements are approximately 50% higher compared to those by *ex-situ* measurements because of the relatively shorter counting times and as a result of field conditions. Uncertainties for *ex-situ* analysis are mostly attributed to sampling and counting statistics (Tsujimoto, 1988).

Accurate interpretation of *in-situ* γ-ray spectrometry measurements depends on proper detector calibration, calculation of radiation flux striking the detector and knowledge of radioactivity distribution on the ground (Laedermann *et al.*, 1998). The accuracy is also severely influenced by several factors including, disequilibrium in the ^{238}U decay series due to the relative mobility of ^{238}U and its decay products in the environment, soil moisture and vegetation, inability to meet standard geometry conditions in the field, instrument stability in the rugged terrestrial environment and atmospheric ^{222}Rn contribution to measurement results (Hendriks *et al.*, 2001; Klusoň and Thinova, 2011).

Conventional application of *in-situ* γ-ray spectrometry has relied upon the deployment of static measuring stations in a manner similar to traditional sampling strategies (Beck *et al.*, 1972; Anspaugh, 1976; Macdonald *et al.*, 1996; Tyler and Copplestone,

2007). While these detectors were portable, the logistical deployment of measurement teams still carried a large overhead from the cost of the equipment and personnel time coupled to the length of measurements, typically 30 - 60 mins per measurement point due to the efficiency of the available detectors. The advent of mobile computing resources has enabled a range of GPS equipped detectors to become readily available and combined with large volume detectors, an efficient continuous γ-ray measurement system is readily deployable for airborne and ground-based radiometric surveys.

Airborne systems although expensive are cost effective for large area surveys and mapping (Dickson, 1990; Wilford *et al.*, 1997; Beamish, 2016) but provide limited spatial resolution. Carborne systems are relatively cheaper and are thus alternatively used for contamination mapping of road networks and areas with off-road access (Cesar and Moreira, 1991; Karlsson *et al.*, 2000; Sanderson *et al.*, 2002; Aage *et al.*, 2006; Bezuidenhout, 2015; Kobayashi *et al.*, 2015), radioactive source search and recovery (Hjerpe *et al.*, 2001; Aage and Korsbech, 2003), and radioactive mineral prospecting (Grasty and Cox, 1997). Mobile backpack systems are used to provide detailed radiometric mapping especially in areas with limited vehicular access and provide high spatial resolution of up to a few meters, depending on the density of measurements (Cresswell and Sanderson, 2009; Kock and Samuelsson, 2011; Nilsson *et al.*, 2014).

2.3 Utility of multivariate exploratory data analysis techniques in the assessment of NORM

The interpretation of radioactivity anomalies in HBRA with respect to space, time and geology can be a challenging task (e.g. among others, separation of anthropogenic and geochemical influences from the natural background). Many of the independent variables such as NORM, geology and mineralogy are often correlated and thus require multivariate techniques to untangle, isolate, study and interpret the underlying phenomena. Consequently, multivariate exploratory data analysis (EDA) techniques (Jobson, 2012; Varmuza and Filzmoser, 2016), such as regression and pattern recognition may be exploited to help overcome these challenges via data mining and modeling due to their robustness, versatility and multivariate capabilities. The performance of the techniques in the determination of variability in (complex) environmental data-sets is superior compared to classical data analysis approaches (Wenning and Erickson, 1994; Einax *et al.*, 1997).

Towards the exploratory analysis of environmental radioactivity data-sets for instance, principal component analysis (PCA), hierarchical clustering analysis (HCA) and artificial neural networks (ANN) techniques have been successfully applied in the classification of soil according to geographical origin (Dragović and Onjia, 2006; Dragovic and Onjia, 2007), determination of provenance for coastal sediments and beach sand (De Meijer and Donoghue, 1995; De Meijer *et al.*, 2001), investigation of the spatial distribution and origin of radioactivity contamination in coal-fired power plants environs (Tsikritzis, 2005; Charro *et al.*, 2013), estimation of geogenic radon potential in a multiple geological setting (Forkapic *et al.*, 2017), etc.

In spite of their usefulness and cost-effectiveness, EDA techniques have hardly been fully exploited in the spatial modeling and data mining of *in-situ* radiological survey data-sets e.g. assessment of NORM and TENORM distribution in complex terrestrial environ-

ments and for radioactivity source attribution. Kanevski *et al.* (2004) demonstrated in a case study on radioactivity contamination in soil from the Chernobly fallout, that EDA techniques (i.e. ANN and support vector regression) are more robust in modeling non-linear and non-stationary spatial trends compared to conventional geo-statistical modeling (variography) techniques. Astel (2007) showed that fuzzy logic techniques can be used in the development of decision support systems for environmental applications i.e. environmetrics.

2.4 Summary on literature review

The studies reviewed demonstrate the importance of monitoring radiation exposure and radioactivity levels in HBRA, and the suitability of *in-situ* γ-ray spectrometry method for measurement of NORM in typical rugged terrestrial environments. However, the multiple geochemical processes in the natural environment and anthropogenic activities can complicate the accurate interpretation of the radiometric measurements. EDA techniques can be useful to overcome these challenges via data mining and multivariate assessment of HBR anomaly distribution.

Chapter 3

Theoretical Background

This chapter provides the basic concepts of γ-ray spectroscopy allied to *in-situ* analysis of NORM. The modes of radioactive decay, mechanisms of gamma-ray photon interaction with matter and how these relate to γ-ray spectrometry are discussed. A brief summary is provided on the complimentary application of X-ray fluorescence (XRF) spectroscopy in the determination by mass measurement of elemental compositions in geological samples. In the end, utility of unsupervised EDA techniques for the multivariate analysis of NORM and the Kriging technique for geo-statistical interpolation of radiometric measurements, is also provided.

3.1 Radioactive decay series

Radioactive decay (or radioactivity) is a spontaneous process by which an unstable (parent) nucleus emits a particle and transforms into another (daughter) nucleus that may or may not be stable. The energy difference (decay energy), as a result of transition is emitted in the form of electromagnetic radiation or kinetic energy of the reaction products (Gilmore, 2008; Podgorsak, 2010). Decay chains can be more complex when the granddaughter and several of its progenies are also radioactive.

The decay kinetics of a radioactive parent nuclide P with decay constant λ_P into a daughter nuclide D, that in turn decays with λ_D into a stable granddaughter nuclide

G (Eq. 3.1), are described as

$$P \xrightarrow{\lambda_P} D \xrightarrow{\lambda_D} G \tag{3.1}$$

The number of P atoms at time t, assuming a constant λ_P and number of daughter nuclei D present at time t are given by Eq. 3.2 and Eq. 3.3, respectively

$$N_P(t) = N_P(0)e^{-\lambda_P t} \tag{3.2}$$

where $N_P(0)$ is the number of P atoms at time $t = 0$.

$$N_D(t) = N_P(0)\frac{\lambda_P}{\lambda_D - \lambda_P}\left[e^{-\lambda_P t} - e^{-\lambda_D t}\right] \tag{3.3}$$

Activity ($\mathcal{A}$) of a source is defined as the rate at which decays occur in the source. In this case, activity of D at time t ($\mathcal{A}_D(t)$) is given by

$$\mathcal{A}_D(t) = \lambda_D N_D(t) = \mathcal{A}_P(t)\frac{\lambda_P}{\lambda_D - \lambda_P}\left[1 - e^{-(\lambda_D - \lambda_P)t}\right] \tag{3.4}$$

where $\mathcal{A}_P(t)$ is activity of P at time t ($\lambda_P N_P(t)$).

The radioactive decay chain described by Eq. 3.1 can be extended to a general chain of decaying nuclei using Bateman equations which stipulate that at $t = 0$, only parent nuclei $N_1(0)$ are present while all other descendant nuclei are not present, i.e. $N_2(0) = N_3(0) = \ldots = N_{i-1}(0) = N_i(0) = 0$.

3.1.1 Equilibrium in radioactive decay series

Radioactive equilibrium between P and D may occur after a certain time when the activities of P and D reach a constant ratio independent of a further increase in time as described by Eq. 3.5.

$$\xi = \frac{\mathcal{A}_P(t)}{\mathcal{A}_D(t)} = \frac{1}{1-m}\left[1 - 2^{\frac{m-1}{m}x}\right] \tag{3.5}$$

where $x = \frac{t}{\left(t_{\frac{1}{2}}\right)_P}$, m is the decay factor $m = \frac{\lambda_P}{\lambda_D} = \frac{\left(t_{\frac{1}{2}}\right)_D}{\left(t_{\frac{1}{2}}\right)_P}$, $t_{\frac{1}{2}}$ is the half-life.

Eq. 3.5 is used to set the conditions for radioactive equilibrium (see Table 3.1) by varying the values for the decay factor m. For $m > 1$, ξ rises exponentially with x, implying that $\mathcal{A}_D(t)/\mathcal{A}_P(t)$ increases exponentially with time and thus *no equilibrium* ensues between P and D. No condition ($m = 1$) has been observed in nature where the half-lives of P and D are equal ($\lambda_D = \lambda_P$).

Table 3.1: Conditions for parent-daughter (radionuclide) equilibrium (source: Podgorsak (2010))

Decay factor	Relative value	Equilibrium	Relationship for ξ
$m \approx 0$	$\lambda_D \gg \lambda_P$	Secular	$\xi = 1$
$0 < m < 1$	$\lambda_D > \lambda_P$	Transient	$\xi = \frac{\lambda_P}{\lambda_D - \lambda_P}$
$m > 1$	$\lambda_D < \lambda_P$	No	$\xi = \frac{1}{m-1}\left[e^{\left(\frac{m-1}{m}\frac{tln2}{\left(t_{\frac{1}{2}}\right)_P}\right)} - 1\right]$

When $0 < m < 1$, the exponential term in Eq. 3.5 diminishes with increasing x and exponentially approaches zero. This implies that at large x, ξ approaches a constant value that is independent of x and equal to $1/1-m$. Under this condition $\mathcal{A}_P(t)$ and $\mathcal{A}_D(t)$ are said to be in *transient equilibrium.*

$$\xi = \frac{1}{1-m} = \frac{\lambda_P}{\lambda_D - \lambda_P} \tag{3.6}$$

As m decreases (i.e. $\lambda_D \gg \lambda_P$), $\mathcal{A}_P(t)$ and $\mathcal{A}_D(t)$ at relatively large time t become approximately equal ($m \to 0 : \ \xi \to 1$). This represents a special case of transient equilibrium in which the parent and daughter are said to be in *secular equilibrium.*

In the natural decay series, radioactive decay and emissions from the daughter products

of ^{238}U and ^{232}Th are used to estimate their (^{238}U and ^{232}Th) activity concentrations with the assumption that secular equilibrium exists. However, disequilibrium especially in the uranium decay series occurs due to escape of radon gas (^{222}Rn) and removal or addition of members of the series by processes such as dissolution or precipitation e.g. leaching of ^{230}Th and ^{226}Ra (IAEA, 2003).

3.1.2 Internal conversion and gamma emission

Nuclear stability depends on the neutron-proton ratio (N/Z), thus an unstable nucleus may undergo several decay processes to reach stability. Whereas a slight imbalance of the ratio causes the radionuclide to undergo beta (β) decay, a large imbalance causes alpha (α) decay. Both the α and β decay modes may produce a daughter nucleus in an excited state which will instantaneously ($\approx 10^{-12}s$) de-excite to reach its ground state, via internal conversion or γ emission processes. Within the context of this work the internal conversion and gamma emission processes are briefly discussed.

3.1.2.1 Internal conversion

Internal conversion (IC) is often preceded by beta decay of a parent nucleus, and occurs when de-excitation energy is transferred from the excited parent nucleus to an orbital electron of the same atom.

$$ {}^{A}_{Z}X^{*} \rightarrow {}^{A}_{Z}X^{+} + e^{-} + Q_{IC} \tag{3.7} $$

Where ${}^{A}_{Z}X^{*}$ is the excited state as a result of α or β decay, ${}^{A}_{Z}X^{+}$ is a singly ionized state of atom ${}^{A}_{Z}X$ following IC, and Q_{IC} is decay energy for IC.

3.1.2.2 Gamma emission

Gamma emission refers to de-excitation of the daughter nucleus by emission of the excitation energy in the form of a γ-ray photon. P and D represent the same nucleus

except P is in an excited state and D is in a lower excited state or ground state.

$$ {}^{A}_{Z}X^{*} \rightarrow {}^{A}_{Z}X + \gamma + Q_{\gamma} \tag{3.8} $$

The energy of γ-ray photon emitted (Eq. 3.9) is well defined and equal to energy difference between the initial $\left({}^{A}_{Z}X^{*}\right)$ and final $\left({}^{A}_{Z}X\right)$ nuclear states. This is a preferred method for identifying radioactive isotopes with energies ranging 100 keV - 10 MeV (Gilmore, 2008).

$$ Q_{\gamma} = E_{\gamma} + (E_K)_D = E_{\gamma}\left(1 + \frac{E_{\gamma}}{2M_D c^2}\right) \tag{3.9} $$

Where Q_{γ} is the gamma emission energy, E_{γ} is the photon energy, and $(E_K)_D$ is the recoil kinetic energy of D.

3.1.3 Naturally occurring radioactive decay series

Natural radioactivity of the terrestrial environment originates from long-lived primordial radionuclides, namely potassium (^{40}K), actinium (^{235}U and its daughters), uranium (^{238}U and its daughters) and thorium (^{232}Th and its daughters). Terrestrial materials i.e. soil, rocks, minerals that contain these radionuclides are referred to as naturally occurring radioactive materials (NORM) (Gilmore, 2008). U and Th are members of the four naturally occurring radioactive heavy elements ($4n$) series (Table 3.2) that begin with heavy and long-lived parents that have half lives of the order of the age of the earth (Podgorsak, 2010). Most of the transitions in each of the series toward the stable nuclides are inter-spaced by $\alpha-$ and few $\beta-$decays. The mass number for each of the Th series are multiples of 4, consequently Th is referred to as the $4n$ series and the rest follow the same rule. Neptunium no longer occurs naturally as it has completely decayed since the formation of the earth $\approx 4.9 \times 10^9$ years ago.

The isotope ^{238}U decays to stable ^{206}Pb via 17 intermediates which emit at 72 energy levels while ^{232}Th decays to ^{208}Pb through 10 intermediates, emitting 46 energy levels. ^{40}K $\left(t_{1/2} = 1.277 \times 10^9\, y\right)$ present in all foods, decays to ^{40}Ar and accounts for

the largest proportion of NORM load among humans through ingestion. Details on the NORM decay series and their schematics can be found in Gilmore (2008).

Table 3.2: Characteristics of the four naturally occurring radioactive element ($4n$) series (source: Podgorsak, 2010); N_α refers to number of $\alpha-$ decays in the chain required to reach the final stable nucleus

Series	Type[†]	Parent	First decay	N_α	$t_{1/2}$ (10^9 years)	Stable end-product
Thorium	$4n$	${}^{232}_{90}Th$	${}^{228}_{88}Ra + \alpha$	6	14.05	${}^{208}_{82}Pb$
Actinium	$4n+3$	${}^{235}_{92}U$	${}^{231}_{90}Th + \alpha$	7	0.704	${}^{207}_{82}Pb$
Neptunium	$4n+1$	${}^{237}_{93}Np$	${}^{233}_{91}Pa + \alpha$	7	2.144×10^{-3}	${}^{209}_{83}Bi$
Uranium	$4n+2$	${}^{238}_{92}U$	${}^{234}_{90}Th + \alpha$	8	4.47	${}^{206}_{82}Pb$

[†] n is an integer

3.2 Interaction of photons with matter

Gamma-ray (and X-ray) photons interaction with matter (the detector) involve either the nuclei or orbital electrons of the absorbing medium (Debertin and Helmer, 1988; Knoll, 2010). The photon-orbital electron interactions are between the photon and either (i) loosely bound electron in *Thomson* and *Compton scattering* processes or (ii) tightly bound electron via *photoelectric absorption* and *Rayleigh scattering* processes. Interactions between the photon and electrostatic field of the nucleus occur via the *pair production* process. The three most relevant interactions discussed in this section are photo-electric absorption, Compton scattering and pair-production.

3.2.1 Photo-electric absorption

When a photon interacts with a bound electron, all of its energy is absorbed by the electron which is then ejected with kinetic energy E_e (Eq. 3.10). The ejected electron leaves a vacancy in the atomic shell resulting in the de-excitation of the atom and

emission of $\gamma-$ray photons.

$$E_e = E_\gamma - E_b \tag{3.10}$$

Where E_b is the electron binding energy and E_γ the photon energy. The cross-section of photo-electric absorption expressed by Eq. 3.11, has a high dependence on atomic number, suggesting that high Z materials are effective in absorption of photons.

$$\tau = \text{const} \times Z^{4.5} \times E_\gamma^{-3} \tag{3.11}$$

Interaction probability of $\gamma-$ray photons with matter depends on photon energy and is described by attenuation coefficients. For photoelectric effect, the attenuation coefficient is expressed by Eq. 3.12

$$\mu_\tau = \tau \times \rho \times \frac{N_A}{M} \tag{3.12}$$

where ρ and M are density and molar mass, respectively of the absorbing medium, N_A is the Avogadro's number.

3.2.2 Compton scattering

In a Compton scattering process, part of the photon energy is transferred to a loosely bound electron scattering it, while the rest of the energy is scattered in the form of a secondary photon. This implies that the total energy of the incident photon is not deposited at the location of first interaction but is distributed over a significant volume. For high energy photons, a series of Compton scattering events ensues each of which reduces the secondary photon energy before terminating it with a photo-electric absorption event. Both energy and momentum are conserved, thus the Compton electron and scattered photon are related to the angles at which they are emitted (Eqs.

3.13 - 3.15).

$$E^{'} = E\left[1+\alpha\left(1-\cos\theta\right)\right] \tag{3.13}$$

$$E_e = E\left[1-\frac{1}{\left(1+\alpha\left(1-\cos\theta\right)\right)}\right] \tag{3.14}$$

$$\tan\phi = \frac{1}{\left[1+\alpha\tan\left(\theta/2\right)\right]} \tag{3.15}$$

Where E, E_e and $E^{'}$ are the energy of incident photon, Compton electron and scattered photon, respectively, while θ and ϕ are the photon and electron scattering angle respectively, and $\alpha = {}^{E}/_{m_0c^2}$ (m_0c^2 is electron rest mass = 511 keV). For very small photon scattering angles, $E_e \rightarrow 0$ and $E^{'} \approx E$, while for a scattering angle of 180°, $E^{'} \approx {}^{E}/_{(1+2\alpha)}$. A summary of various energy and angle dependencies of Compton scattering can be found elsewhere (Debertin and Helmer, 1988). The attenuation coefficient of Compton scattering is expressed by Eq. 3.16, where σ is the scatter cross-section.

$$\mu_\sigma = \sigma \times \rho \times \frac{N_A}{M} \tag{3.16}$$

3.2.3 Pair production

In a pair production process, a $\gamma-$ray with energy greater than twice the energy corresponding to electron rest mass i.e. $\geqslant 1.022$ MeV is converted to an electron-positron pair in a nuclear Coulomb field. The excess energy ($E_\gamma - 2m_oc^2$) is shared between the two particles as kinetic energy before losing it to the absorbing medium. The positron subsequently annihilates with the electron, and the result is two photons that are emitted in opposite directions in order to conserve energy and momentum.

Similar to Compton scattering, the original incident $\gamma-$ray is not deposited at the location of first interaction. Each of the 511 keV photon carries its energy to another location where it interacts further by Compton scattering or photo-electric absorption. The attenuation coefficient of pair production is expressed by Eq. 3.17, where κ is the

interaction cross-section.

$$\mu_\kappa = \kappa \times \rho \times \frac{N_A}{M} \tag{3.17}$$

Photo-electric absorption events have high probability for lower energies (< 150 keV) while Compton scattering events are highly probable for mid-energy ranges (> 150 keV to 1.022 MeV). Single and double escape peaks as a result of pair production events occur for higher energies (> 1.022 MeV), as illustrated in Fig. 3.1.

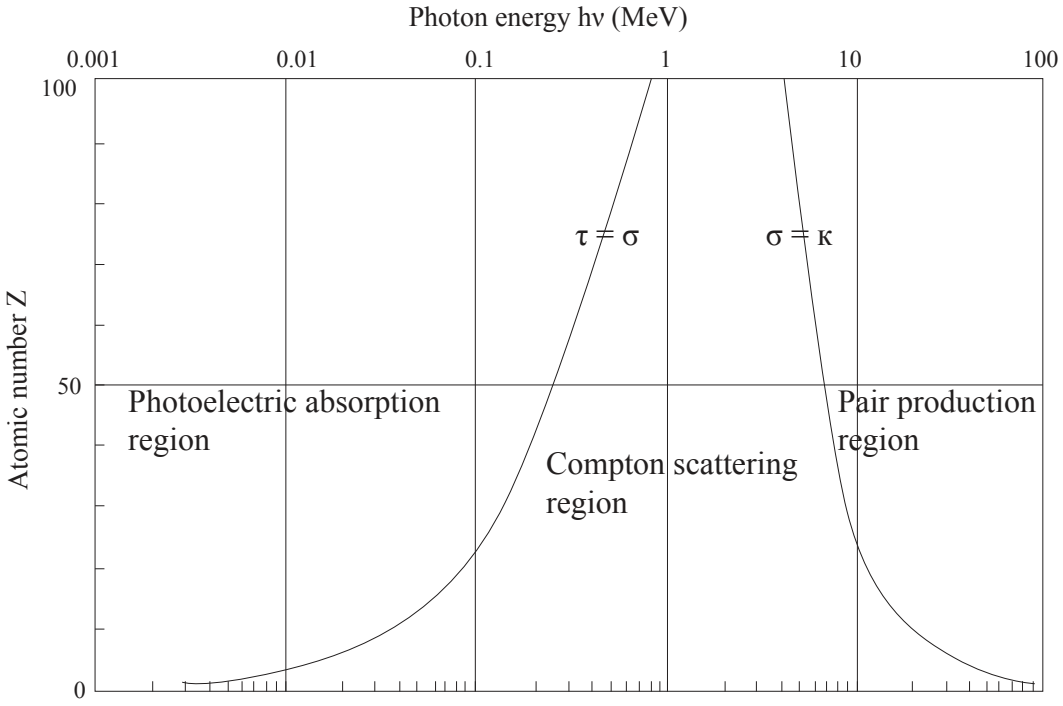

Fig. 3.1: Representation of relative predominance of the three main photon interaction processes (adapted from: Podgorsak (2010)). The curved lines show the values of Z and $h\nu$ for which the two neighbouring effects are equal.

3.3 Gamma-ray spectroscopy

Gamma-rays emitted during a radioactive decay process may be used to among other utilities, identify radionuclides responsible for the emission by determining their energies and quantifying their activity concentrations. Gamma-ray spectroscopy is a direct

technique (does not require chemical separations) for radionuclide identification and activity quantification. The photo-peak corresponds to an event where the $\gamma-$ray has deposited almost all its energy in the detector. The method is established for both laboratory and *in-situ* measurements (Gilmore, 2008; Beck *et al.*, 1972).

Incident $\gamma-$rays interact in the detector's active volume mainly via photo-electric absorption, Compton scattering and pair production, and transfer all or part of their energy to electrons of the detector resulting in the generation of excited electrons. These excited electrons loose energy through ionization and excitation of detector atoms, giving rise to multiple electron-hole pairs proportional to the energy of the electrons produced during the primary interaction (Knoll, 2010). Most $\gamma-$ray spectroscopy is realized using semiconductor (i.e. HPGe) and scintillation (i.e. NaI(Tl)) detectors designed to convert the electron-hole pairs into electrical signals for pulse processing. The number of events taking place in a detector depends on the energy of interacting $\gamma-$rays.

3.3.1 Attenuation of gamma-rays

In γ-ray spectroscopy, only the fraction of mono-energetic photons that penetrate the detector medium without any interaction (i.e. have their original energy and direction intact) are considered. Attenuation therefore refers to the remaining photons that have either been absorbed or scattered in the detector (Debertin and Helmer, 1988). The total linear attenuation coefficient is expressed by Eq. 3.18.

$$\mu = \mu_\tau + \mu_\sigma + \mu_\kappa \tag{3.18}$$

When a beam of photons enters a layer of thickness t, perpendicular to the surface, the number of transmitted photons N is given in terms of the original number of photons N_o.

$$N = N_o \exp^{-\left(\frac{\mu}{\rho}\right)\rho t} \tag{3.19}$$

Where $\dfrac{\mu}{\rho}$ is the mass attenuation coefficient.

3.3.2 *In-situ* gamma-ray spectrometry

For standard *in-situ* γ-ray spectrometry measurements, the detector is placed at a height of approximately 1 m above the ground, thereby enlarging the detector's field of view for higher energy photons and for photons closer to the ground (Beck *et al.*, 1972; Miller and Shebell, 1993), as illustrated in Fig. 3.2(a). In practice, the arrangement is simplified by assuming a flat air-ground interface and an infinite volume of soil known as infinite half-space (ICRU, 1994). The detector is positioned at the origin with the air-ground interface located a distance h below the detector, as illustrated in Fig. 3.2(b).

For a gamma source of energy E, total unscattered flux is given by Eq. 3.20. Let r_D be the vector which designates the position of the detector relative to the origin O, r the position of a differential volume of soil, and r_i the location of the air-ground interface

$$\phi = \int_V \frac{f(r)}{4\pi \left(r_D - r\right)^2} \exp\left[-\frac{\mu_s}{\rho}\rho\left(r_i - r\right) - \frac{\mu_a}{\rho_a}\rho_a\left(r_D - r_i\right)\right] dV \tag{3.20}$$

where $f(r)$ is source strength at r, μ_a, μ_s are air and soil total γ-ray attenuation coefficients, ρ_a, ρ are air and soil bulk density, $\frac{\mu_s}{\rho}$ is mass attenuation coefficient for soil, and $\frac{\mu_a}{\rho_a}$ is mass attenuation coefficient for air (Miller and Shebell, 1993).

The fundamental parameters used for *in-situ* γ-ray spectrometry include full absorption peak count rate (N), fluence rate (ϕ) and gamma source activity (A). From the quantities, a single factor (Eq. 3.21) is derived to convert the source activity or dose-rate in air from the measured peak count rate in a spectrum (Beck *et al.*, 1972).

$$\frac{N_f}{A} = \frac{N_f}{N_o}.\frac{N_o}{\phi}.\frac{\phi}{A} \tag{3.21}$$

where $\frac{N_f}{A}$ is full energy absorption peak, $\frac{N_f}{N_o}$ is angular correction factor, $\frac{N_o}{\phi}$ is full energy absorption peak count rate per fluence rate (peak response), and $\frac{\phi}{A}$ is the fluence rate due to a gamma transition for a particular nuclide.

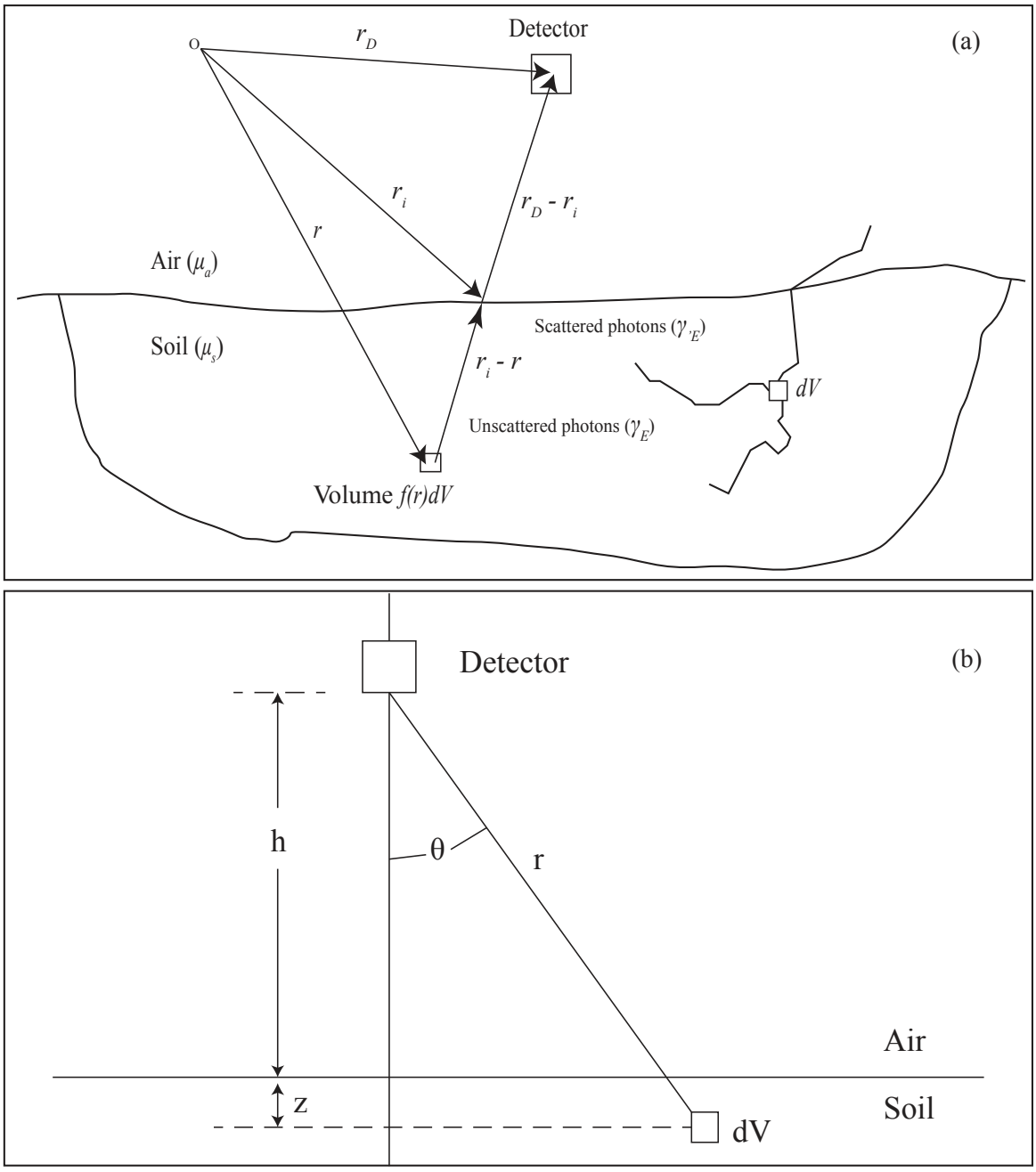

Fig. 3.2: Theoretical models for (a) typical *in-situ* γ-ray spectrometry measurement (adapted from: Miller and Shebell (1993)) and (b) an infinite half-space source geometry (adapted from: ICRU (1994)).

3.3.2.1 Distribution of natural radioactivity in the terrestrial environment

Natural radioactivity on the ground is assumed to be uniformly distributed, as illustrated in Fig. 3.3. The distribution of natural radionuclides is expressed by Eq. 3.22 and photon flux determined by Eq. 3.23. Soil composition and variations in soil density have minimal impact on the photon flux while excessive ground roughness provides additional self-absorption. Variations in air density only occur with altitude (Miller and Shebell, 1993).

$$f(z) = S_V \tag{3.22}$$

Where S_V is soil activity per unit volume (photons/ cm^3-s).

$$\frac{\phi}{S_V/\rho} = \frac{1}{2}\frac{\mu_a}{\rho_a}\frac{\rho}{\mu_s}\rho h\left(\frac{\exp\left[\mu_a/\rho_a\right]\rho_a h}{\left[\mu_a/\rho_a\right]\rho_a h}\right) - E_1\left(\frac{\mu_a}{\rho_a}\rho_a h\right) \tag{3.23}$$

Where $\rho_a h$ is mass depth of air and E_1 is exponential integral defined by $E_1(x) \cong \int_x^\infty \frac{e^{-t}}{t}dt$.

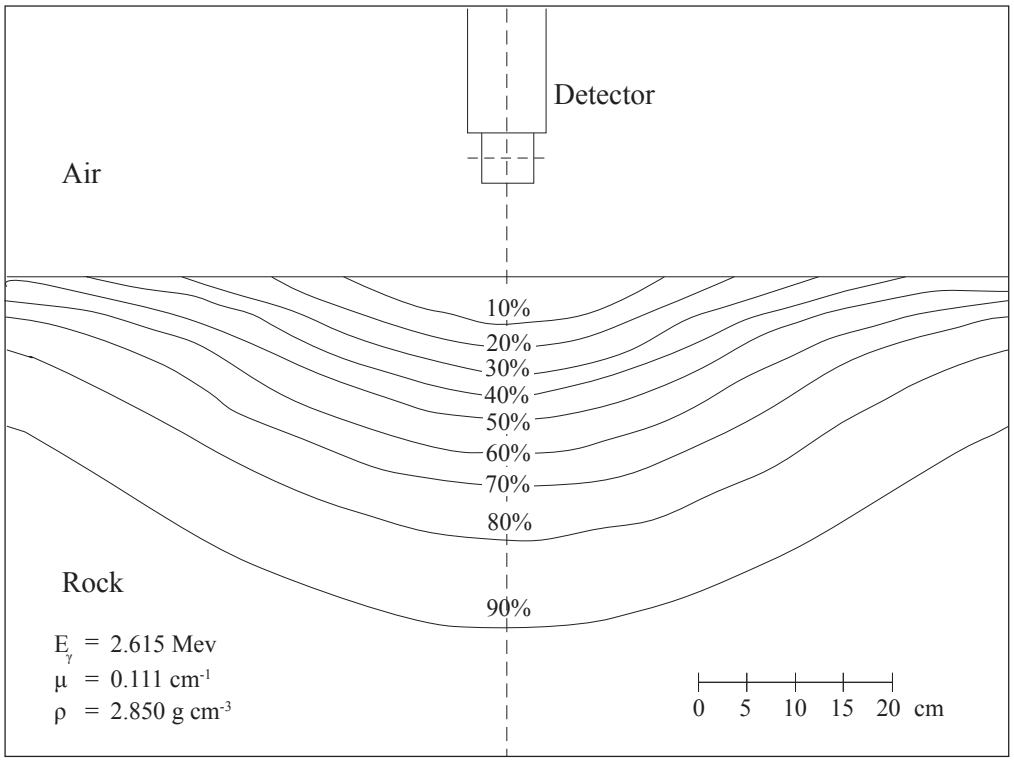

Fig. 3.3: Illustration of the typical distribution of ^{232}Th at ground level (adapted from: IAEA (1989)).

3.3.3 Gamma-ray spectrometry using a portable NaI(Tl) detector

The applicability of semiconductor detectors for *in-situ* measurements is hindered by the need of cooling, available detector sizes and high cost. Scintillation detectors are thus more preferred as they are relatively cheaper and available in large crystals with moderate resolution and are operable at ambient temperatures (Anspaugh, 1976). The acquired spectra are mostly processed using the windows method (IAEA, 2003) which entails monitoring photo-peaks of ^{40}K (1460 keV), ^{214}Bi (1765 keV), and ^{208}Tl (2614 keV) for determination of NORM. In the present work, the NaI(Tl) detector was utilized. NaI(Tl) crystals have a high density, with a detection efficiency of up to 100% for low energy $\gamma-$rays. The dead-time is of the order of 100 ns while energy resolution for ^{137}Cs at 662 keV is 10 %, and 7 % for ^{208}Tl at 2614 keV (IAEA, 2003).

Incident $\gamma-$rays interact with the crystal lattice of the NaI(Tl) detector to produce charged particles i.e. electrons and positrons through photo-electric absorption, Compton scattering and pair-production processes. The charged particles excite the NaI(Tl) crystals leading to the emission of visible light photons (scintillation). Approximately 11% of the incident $\gamma-$ray energy is converted into photons with an average of 3.0 eV in 0.23 μs with a maximum wavelength emission of 415 nm (Knoll, 2010).

Pulse height distribution of a $\gamma-$ray incident on the detector depends on the size of detector, and relative cross-sections for the photo-electric absorption, Compton scattering and pair-production processes (Ouseph, 1975). The contributions to pulse height distribution due to events occurring in a NaI(Tl) detector, are presented in Table 3.3. Typical $\gamma-$ray spectra obtained by a portable NaI(Tl) detector illustrating the various photon interaction events, are shown in Fig. A.2, Appendix A.1.

Table 3.3: Pulse height distribution due to events occurring in a NaI(Tl) detector (source: Ouseph (1975))

	Interaction process	Energy absorbed in crystal	Pulse height artefact
(a)	Photo-electric effect	E_γ	pulses in photo-peak
(b)	Compton effect (scattered γ escapes)	varies from 0 to E'_{max} $E'_{max} = E_\gamma \left(1 + \frac{m_0 c^2}{2E_\gamma}\right)$	pulses in the Compton continuum
(c)	Compton effect (scattered γ absorbed)	E_γ	pulses in the photo-peak
(d)	Pair production (annihilation $\gamma-$rays escape)	kinetic E of e^- e^+ pair $= E_\gamma - 1.022$ MeV	double escape peak $(E_\gamma - 1.022)$ MeV
(e)	Pair production (one annihilation γ escapes)	$E_\gamma - 1.022 + 0.511$ $= E_\gamma - 0.511$ MeV	single escape peak $(E_\gamma - 0.511)$ MeV
(f)	Pair production (both photons absorbed)	E_γ	pulses in the photo-peak
(g)	Pair production (one of the annihilation γ produces Compton electron)	Compton contribution of $E_\gamma - 0.511$ MeV	pulses in the Compton continuum
(h)	Compton backscattering	$E_\gamma - E'_{max} - E_{e(max)}$	backscatter peak (0.2 to 0.25 MeV)
(i)	Compton at $\theta \neq \pi$	energy variations between $E_\gamma - E'_{max}$ and E_γ	pulses in the Compton continuum
(j)	Pair production outside, and one γ scattered in detector	0.511 MeV	peak at 0.511 MeV

†Symbols explained in Section 3.2

3.4 X-ray fluorescence spectroscopy

Assessment of NORM by *in-situ* γ-ray spectrometry may be complemented by laboratory analyses of elemental compositions in field samples, utilizing the XRF spectroscopy technique. XRF provides for the direct determination of K, U and Th elemental concentrations by mass measurement. Thus the combination of *in-situ* γ-ray spectrometry and EDXRF analysis of field samples provides a more elaborate approach to the assessment of natural radioactivity in the environment. In this section, a brief summary on the principles of XRF spectroscopy is presented.

XRF spectroscopy is a non-destructive analytical technique which utilizes X-rays in elemental analysis. It enables simultaneous qualitative and quantitative analyses of the multi-elemental composition of materials, with element-dependent detection limits (DL) of as low as ppb concentrations depending on the sample type (solid, liquid) and spectrometric conditions. The analytical sample is excited in the core levels of its atoms by high energy photons, resulting in de-excitation by emission of characteristic fluorescent radiation with discrete energy (or wavelength) that is uniquely related to the element identity and concentration (van Grieken and Markowicz, 2001).

Three XRF spectrometry modalities mainly differentiated by their detection systems i.e. wavelength dispersive (WDXRF), energy dispersive (EDXRF) and particle-induced X-ray emission (PIXE), exist. Within the scope of this thesis, only the tube-excited EDXRF spectrometry in which the X-ray beam is polarized will be considered.

3.4.1 Polarization of primary X-ray radiation

In EDXRF spectrometry, it is the intensity of the characteristic fluoresced X-ray from the sample that provides the analyte signal for quantification; scattering of the excitation beam provides background contributions that often interferes with the analyte signal by introducing spectral noise and interference in the measured spectrum (Jenkins, 1995). Polarization of the X-ray beam reduces the background resulting in the improvement of

elemental DL due to enhanced SNR (van Grieken and Markowicz, 2001).

3.4.2 Absorption of primary X-ray radiation

When a beam of X-ray photons described by the intensity $I_o(\lambda_o)$ irradiates a specimen of thickness t, as illustrated in Fig 3.4, a portion of the beam is transmitted through the specimen whilst the remaining fraction is absorbed as determined by the Beer-Lambert law (Jenkins, 1995):

$$I_x(\lambda_o) = I_o(\lambda_o) \exp\left[-\mu(\lambda_o)\,\rho x\,(\csc\psi_1)\right] \tag{3.24}$$

Where $\mu(\lambda_o)$ is mass attenuation coefficient of specimen for photons with wavelength λ_o, ρ is density of specimen, x is distance travelled through the specimen.

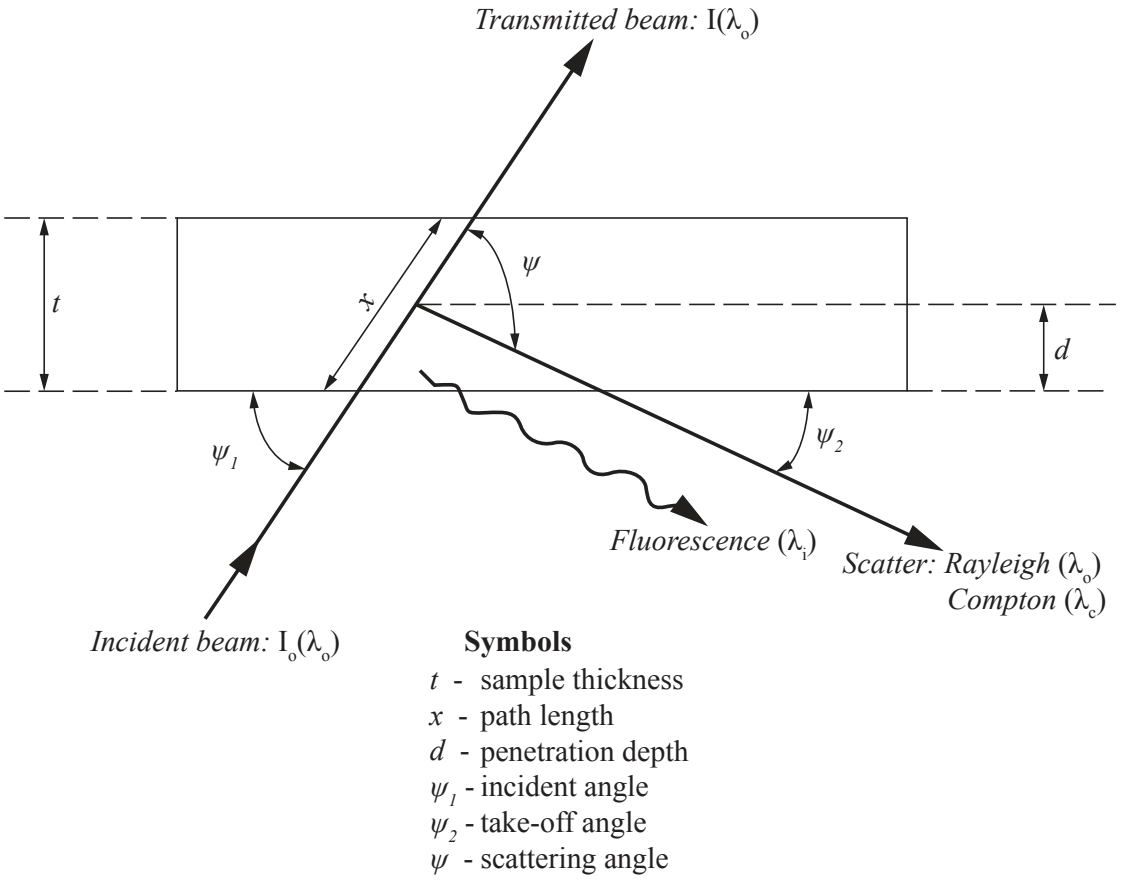

Fig. 3.4: A simplified representation of the geometry involved during interaction of primary X-ray beam with specimen (adapted from: Jenkins (1995)).

Only a fraction of the absorbed photons excites atomic electrons, via photo-electric absorption, to cause the emission of secondary fluorescent radiation having characteristic wavelengths and intensities related to analyte concentration, collimated at a solid angle Ω, toward the detector.

The quantification of analytes involves the conversion of measured X-ray fluorescent intensities to elemental concentrations in the sample. The intensity of analyte i in the specimen excited by the primary beam depends on its concentration and chemical composition of the specimen (matrix)

$$I_i(\lambda_o) = K_i I_o(\lambda_o) \frac{\mu_i(\lambda_o)}{\mu_s(\lambda_o) + G\mu_s(\lambda_i)} W_i \tag{3.25}$$

where $K_i = \left(\frac{\Omega}{4\pi}\right) Q_i(\lambda_o,\lambda_i)$ and $G = \frac{\sin\psi_1}{\sin\psi_2}.\ Q_i(\lambda_o,\lambda_i)$.

3.5 Exploratory data analysis and spatial data interpolation

The principal component analysis (PCA) technique was used in this work for multivariate exploratory analysis of the measured radioactivity concentrations, while ternary plots were used to investigate the variability of natural radionuclides in the study area. The Kriging technique was used to perform gridding (data interpolation using original observations) of the *in-situ* gamma dose-rate measurements for spatial mapping.

3.5.1 Principal component analysis

PCA is a well-established technique for unsupervised EDA (Brereton, 2003). In this technique, the original data set ($\boldsymbol{X}$ with n observations and m variables) is mean-centered ($\boldsymbol{X_c}$) and decomposed orthogonally into a score matrix $\boldsymbol{T}$, loading matrix $\boldsymbol{P}$ and matrix of residuals $\boldsymbol{E}$ (Eq. 3.26). A graphical two-dimensional (2-D) scatter plot of the scores and loadings vectors in different combinations helps in the description of covariance between observations, thus providing an easily understood interpretable overview of the data (Varmuza and Filzmoser, 2016).

$$X_c = T.P^T + E \tag{3.26}$$

The scores matrix $\boldsymbol{T}\,(n \times A)$ expresses relationships in the observations (in this case, measured radionuclide concentrations) in new orthogonal coordinate axes, known as principal components (PC). The first principal component (PC1) is the linear latent variable with the maximum possible variance, while the direction of PC2 is orthogonal to the direction of PC1. A is the intrinsic dimension i.e., number of PCs necessary to describe the variance present in the data; the importance of a PC is expressed as a percentage of the total variance. The loadings matrix $\boldsymbol{P}\,(A \times p)$ describes the data structure in terms of variable (in this case, natural radionuclides) correlations such that each variable has a loading on each PC.

3.5.2 Ternary plots of three variable measurements

Ternary diagrams are useful in the visualization and display of the variability of three-part compositional data $\boldsymbol{X} = (x_1, x_2, x_3)$ whose variables are depicted as positions in an equilateral triangle (Aitchison, 1986). Individual portions of any measurement are inferred by drawing a line through the investigated point, and parallel to the edge opposite to the corner of the variable of interest, as shown in Fig. 3.5.

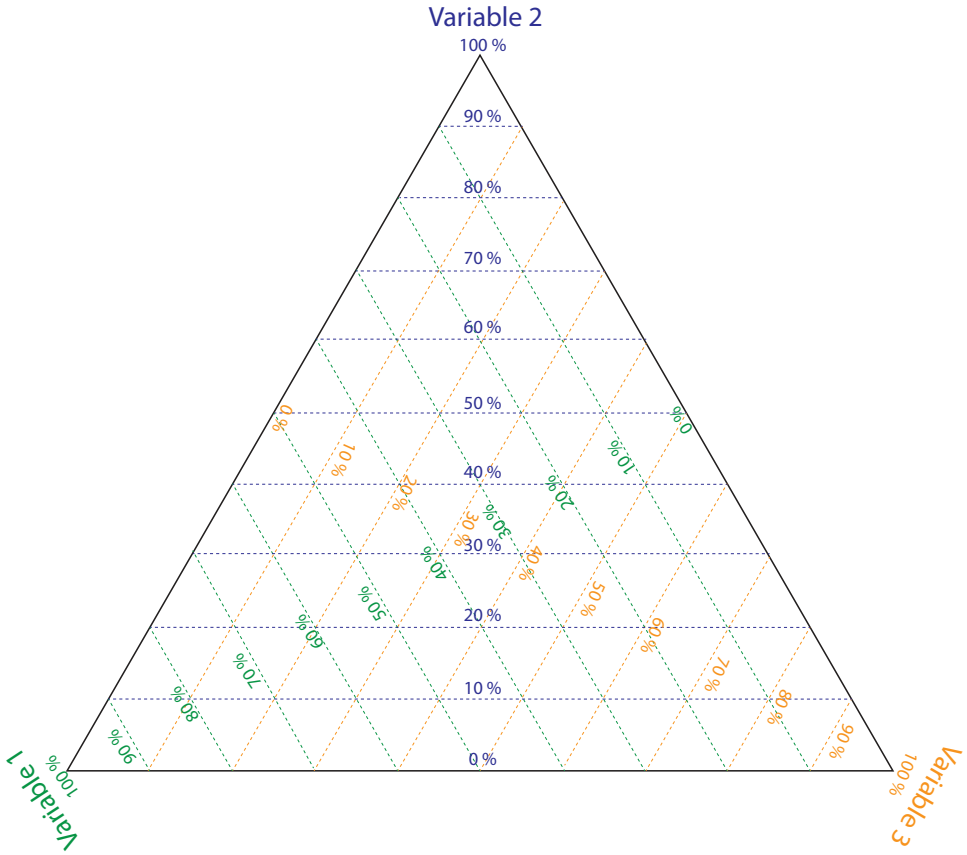

Fig. 3.5: Ternary plot for representing relative proportions of three-variables in 2-D.

It follows that, the perpendiculars from any point $\boldsymbol{P}$ (x_1, x_2, x_3) in the triangle to the sides opposite 1, 2, 3 satisfy Eq. 3.27. Furthermore, compositions with two components (x_2, x_3) in constant ratio can be represented by points on a straight line through the complementary vertex of 1.

$$x_i \geqslant 0 \quad (i = 1, 2, 3)\,, \qquad x_1 + x_2 + x_3 = 1 \tag{3.27}$$

Detailed explanation of the theory and applications of ternary diagrams in the geo-

sciences can be found elsewhere (Bucianti *et al.*, 2006). In the present study, the natural radionuclide concentration data-sets were plotted on ternary diagrams whose apexes are ^{40}K, ^{238}U and ^{232}Th, expressed in percent of the combined radionuclide concentrations.

3.5.3 Kriging technique

Geo-statistical techniques such as variograms and kriging are used to interpolate and investigate the distribution of spatial variables (Webster and Oliver, 2007). The ordinary kriging technique was used in this work to perform interpolation for spatial mapping of the *in-situ* radiometric measurements over non-sampled locations so as to investigate the spatial dependency in the surveyed areas. The technique uses the semi-varioagram function $\gamma(h)$ to describe the relationship of spatially correlated data.

For a set of data points $Z(X_i)$, $i = 1, 2, \ldots$, $\gamma(h)$ is expressed by

$$\gamma(h) = \frac{1}{2N(h)} \sum_{i=1}^{N(h)} \{Z(X_i) - Z(X_i + h)\}^2 \tag{3.28}$$

where $N(h)$ is number of data pairs separated by the lag vector h, $Z(X_i)$ data interpolation at location X_i, h is distance between data points, X_i is data position.

Mapping of the kriged values (i.e. interpolation) is achieved using the nearest sampling points (grid nodes) to create a fine grid using specialized computational and GIS software such as the Golden Software (GoldenSoftware, 2015).

Chapter 4

Materials and Methods

A wide-ranging *in-situ* radiometric survey using portable $\gamma-$ray spectrometers was conducted in the south-coastal region of Kenya for 5 days (09 - 15 June 2014), covering over 70 km of the south coast paved road and selected off-roads and 28 km^2 of the Mrima-Kiruku complex. A number of geological samples were collected from selected sites for laboratory XRF analysis for their elemental composition using a polarized EDXRF spectrometer. In this chapter, geographical and survey descriptions, sample processing procedures as well as the instrumentation and methodology aspects of the $\gamma-$ray and EDXRF spectrometers are provided.

4.1 *In-situ* gamma-ray spectrometric measurements

Two portable PGIS-2 $\gamma-$ray spectrometers of 0.33 l (PGIS-21) and 2.0 l (PGIS-128) NaI(Tl) crystal volumes from Pico Envirotec Inc. (pics shown in Fig. 4.1), were used in this work. They consists of a scintillation detector unit, integrated with GPS, and a data logger unit controlled by an Android based Tablet computer via wireless Bluetooth connection. The dimensions and weight for the PGIS-128 system are 46 cm $\times$ 22 cm $\times$16 cm and 12 kg, respectively, while dimensions and weight for the PGIS-21 system are 50 cm $\times$ 16 cm $\times$ 20 cm and 5.3 kg, respectively. A full description of the spectrometers capability and specifications can be found elsewhere (PEI, 2013a).

PGIS-128 consisting of a 2.0 l. NaI (Tl) detector.

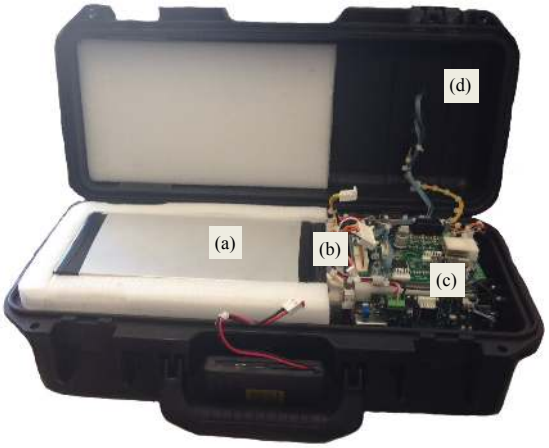

(a) - NaI(Tl) detector

(b) - PMT

(c) - Electronics and data acquisition

(d) - Spectrometer housing

PGIS-21 consisting of a 0.33 l. NaI (Tl) detector.

Fig. 4.1: PGIS-2 portable $\gamma-$ray spectrometers from Pico Envirotec Inc.

Carborne measurements were taken at 1 s interval while transiting the study area at speeds not exceeding 80 km h^{-1} and 60 km h^{-1} along the paved roads and the off-roads, respectively to increase the accuracy of the measurements. The PGIS-128 detector was laid horizontally on the vehicle floor, behind the gear compartment such that its sensitive volume was approximately 0.5 m above ground level.

Ground-based continuous measurements also taken at 1 s interval entailed systematic transverses over accessible parts of selected sites on foot with the detectors mounted on tightly strapped backpack casings, as illustrated in Fig. 4.2. In this configuration, the detectors pointed downwards with distance between the ground level and the center of the sensitive volume of the detectors being approximately 1 m. The two field personnel operating the systems were required to be physically fit given the weight and harsh terrain encountered. It took an average of 60 - 90 mins per individual at a walking pace of 0.5 - 1.0 m s^{-1} to conduct continuous measurements before taking a break.

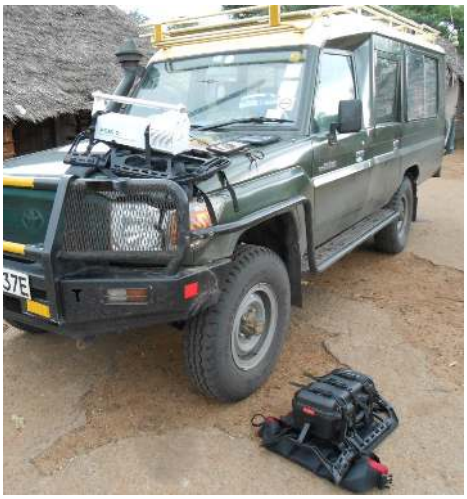

Motor vehicle used for *in-situ* vehicular radiometric measurements. Detector was laid horizontally inside the vehicle's floor.

PGIS-2 detectors mounted on backpack for *in-situ* ground-based radiometric measurements.

Fig. 4.2: Deployment of PGIS-2 spectrometers for *in-situ* field measurements.

4.1.1 Detector set-up and pulse processing

The detector unit comprises a NaI(Tl) scintillation crystal coupled to a photomultiplier tube (PMT), high voltage (HV) supply, preamplifier, analog-to-digital converter (ADC) and multi-channel analyzer (MCA), see Fig. 4.3.

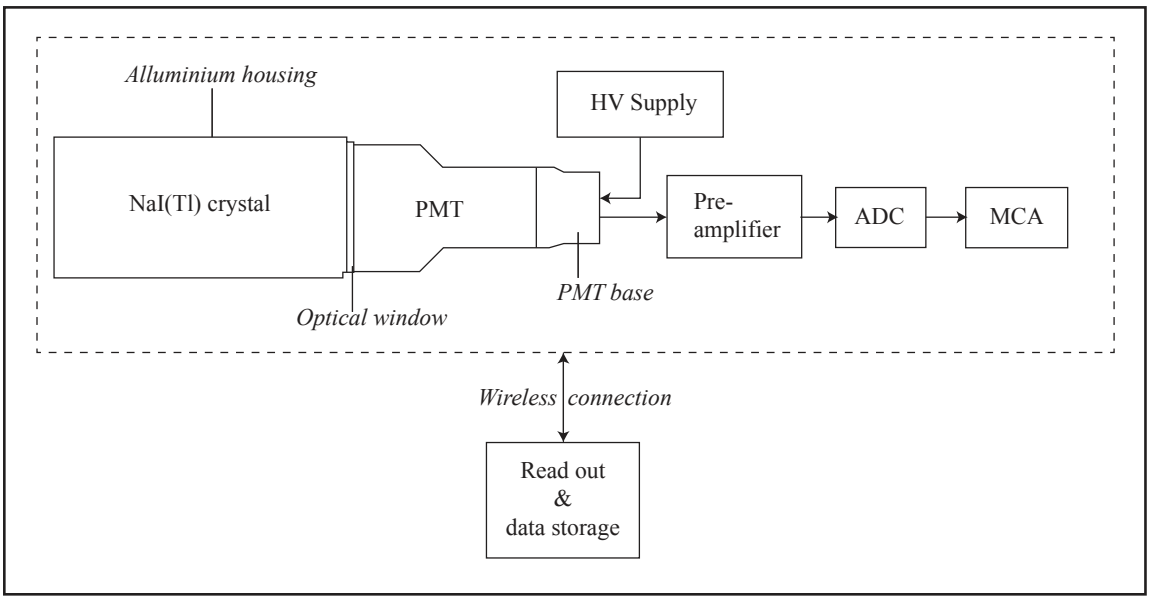

Fig. 4.3: Schematic diagram of the PGIS-2 portable $\gamma-$ray spectrometer.

The PMT facilitates the detection of visible light photons through the production of multiple photo-electrons and ultimately, a negative voltage pulse output with an amplitude proportional to the energy of the incident photon (Knoll, 2010). The pulse output is integrated by a charge sensitive preamplifier, producing slow decaying exponential pulse of approximately 50 μs which is digitized via the ADC (usually 14 bit, ≥50 MHz) and processed by the MCA.

4.1.2 Spectrometer calibration

4.1.2.1 Background correction

Background radiation refers to the internal radioactivity of a radiometric instrument, cosmic radiation and atmospheric radon (IAEA, 2003). Background correction is therefore necessary to minimize noise and increase accuracy of the measurement. The procedure for correction of the PGIS-2 spectrometer requires the adjustment of high voltage for linearity with natural radionuclide peaks based on the background radiation and detector volume (PEI, 2010). This procedure was carried out in Diani, Kenya several hundred meters from the Indian Ocean shore, an area identified with low natural background radiation.

4.1.2.2 Calibration for analysis of K, U and Th

In-situ $\gamma-$ray spectra can be complex due to the varying natural radionuclide compositions from wide-ranging field terrain, further complicated by multiple Compton scattering events. For instance, the counts in the U window originate not only from primary ^{214}Bi (1764 keV) photons, but also from scattered ^{208}Tl (2614 keV) photons. Stripping correction removes the scattered contributions, so that a specific energy window contains counts from the primary radiation of corresponding isotope (IAEA, 1989).

Calibration of portable spectrometers for analysis of natural radionuclides requires the estimation of stripping ratios and sensitivity constants, that relate detector count rates

to radionuclide concentration using calibration pads. A standard matrix approach, expressed by Eqs. 4.1 and 4.2 is used to correct for spectral interferences making use of the stripping ratios (IAEA, 2003).

$$n_i = s_{i\mathrm{K}}c_{\mathrm{K}} + s_{i\mathrm{U}}c_{\mathrm{U}} + s_{i\mathrm{Th}}c_{\mathrm{Th}} + n_{i\mathrm{BG}} \quad (4.1)$$

$$N = SC \quad (4.2)$$

Where n_i is count rate in the i^{th} energy window (K, U, Th), s_{ij} is sensitivity of the spectrometer for detection of the j^{th} element in the i^{th} energy window, c_j is concentration of the j^{th} element (% K, ppm eU, ppm eTh), and $n_{i\mathrm{BG}}$ is background count rate in the i^{th} energy window.

Eq. 4.2 is the matrix form of Eq. 4.1 based on the three energy windows whose background count rates are subtracted from $n_{i\mathrm{BG}}$. N is the column vector of background-corrected count rates ($n_i - n_{iBG}$), S is a 3×3 matrix of sensitivities (S_{ij}), and C is column vector of concentrations ($c_{\mathrm{K}}, c_{\mathrm{U}}, c_{\mathrm{Th}}$).

The PGIS-2 spectrometers were calibrated by taking 600 s measurements on transportable concrete calibration pads of dimensions: 1 m $\times$ 1 m $\times$ 0.3 m thick, as shown in Fig. A.1 in Appendix A.1, containing known K, Th and U concentrations and a fourth pad which served as background, see also Table A.1, Appendix A.1. The K, U and Th window sensitivities (see Table A.2, Appendix A.1) were estimated using Eq. 4.3.

$$n_i - n_{i\mathrm{BG}} = s_{i\mathrm{K}}\triangle c_{\mathrm{K}} + s_{i\mathrm{U}}\triangle c_{\mathrm{U}} + s_{i\mathrm{Th}}\triangle c_{\mathrm{Th}} \quad (4.3)$$

Where $\triangle c_j$ is the difference between the concentrations of the j^{th} element in a calibration pad and the concentration of the j^{th} element in the background pad. Due to the finite dimensions of the calibration pads, a geometry correction factor of 1 was applied to the derived sensitivities.

For K, U and Th energy windows (i=1, 2 and 3), the stripping ratios (α, β, γ, a, b and g) were calculated from the ratio of sensitivities (see Table A.3, Appendix A.1) using Eqs. 4.4 and 4.5.

$$\alpha = \frac{s_{2\mathrm{Th}}}{s_{3\mathrm{Th}}} \qquad \beta = \frac{s_{1\mathrm{Th}}}{s_{3\mathrm{Th}}} \qquad \gamma = \frac{s_{1\mathrm{U}}}{s_{2\mathrm{U}}} \tag{4.4}$$

$$a = \frac{s_{3\mathrm{U}}}{s_{2\mathrm{U}}} \qquad b = \frac{s_{3\mathrm{K}}}{s_{1\mathrm{K}}} \qquad g = \frac{s_{2\mathrm{K}}}{s_{1\mathrm{K}}} \tag{4.5}$$

Where, α is the Th into U stripping ratio, a is the U into Th stripping ratio, β is the Th into K stripping ratio, b is the K into Th stripping ratio, γ is the U into K stripping ratio, and g is the K into U stripping ratio.

4.1.2.3 Energy calibration

Measured PGIS-2 $\gamma-$ray spectra (0 - 3000 keV) were resolved into 256 channels, each channel width (i.e. resolution) ranging from 10 to 12 keV. Energy calibration was performed by relating strong photo-peaks in various energy windows to their corresponding centroid channel positions, using Eq. 4.6. For instace, the calibration curve used for PGIS-128 is shown in Fig. 4.4 and typical calibrated spectra obtained by the spectrometer are shown in Fig. A.2, Appendix A.1.

$$E(\mathrm{keV}) = I(\mathrm{keV}) + G \times C(\mathrm{channels}) \tag{4.6}$$

Where, I and G are intercept and gradient of the calibration line respectively, and C is channel position.

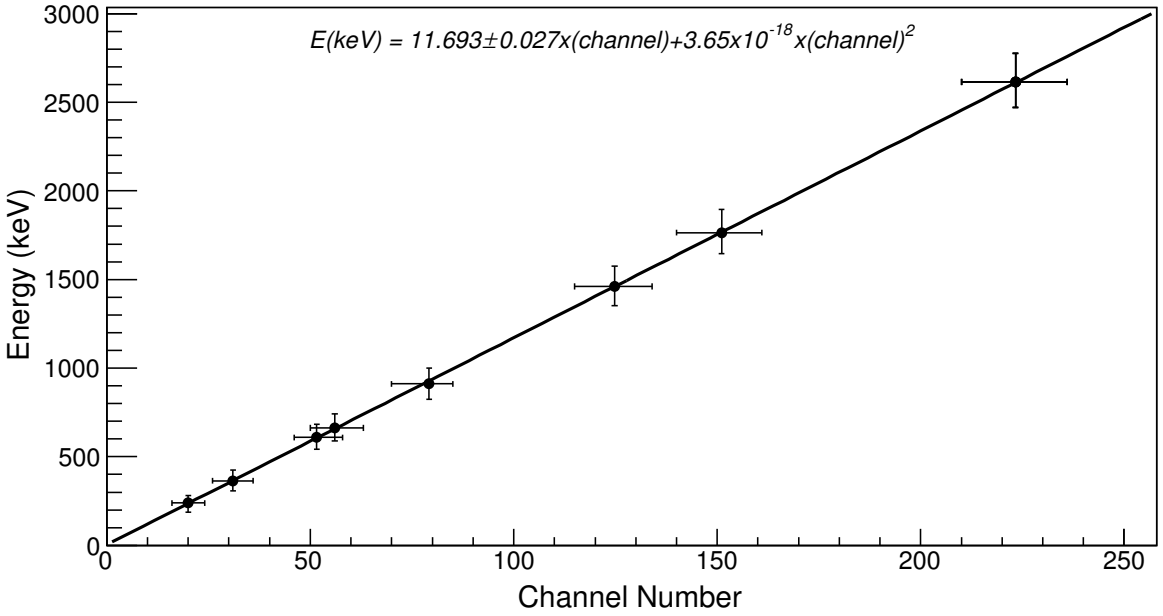

Fig. 4.4: Energy calibration curve for the PGIS-128 $\gamma-$ray spectra.

4.1.3 Spectral data processing

In this work, the window based approach (IAEA, 2003) in which elemental and activity concentrations are extracted from spectral windows of K, U and Th (see Table 4.1), was used to process the PGIS-2 spectra. Elemental results were reported in terms of equivalent uranium (eU), equivalent thorium (eTh) and potassium (K); eU and eTh imply that parent concentrations are inferred from decay products, assuming secular equilibrium and homogeneous activity distribution (ICRU, 1994; IAEA, 2003).

4.1.3.1 Spectrum fitting

The Praga4Ground software (PEI, 2013b) was used to perform least-squares (LSQ) fitting of natural radionuclide photo-peaks in the measured spectra utilizing model detector responses i.e. photo-peak resolution, amount of Compton scattering, derived prior by Monte Carlo simulations (PEI, 2013b). LSQ fitting requires the sum of squares random error (R^2) minimization (expressed by Eq. 4.7) to determine the net photo-peak

areas in specific energy windows (Debertin and Helmer, 1988).

$$R^2 = \sum_i \omega_i \left(N_i - f_i\right)^2 \tag{4.7}$$

Where $N_i \pm \sigma(N_i)$ are the measured peak areas, $\omega_i = \sigma \left(N_i\right)^{-2}$ is the weighting factor, and f_i the calculated peak areas.

Table 4.1: Standard $\gamma-$ray energy windows for determination of natural radionuclides (source: IAEA (2003)); energy of photo-peak is indicated in the brackets

Window	Radionuclide	Emission probability (%)	Energy range (keV)
Total counts	-	-	400 - 2810
Potassium	^{40}K (1460 keV)	10.7	1370 - 1570
Uranium	^{214}Bi (1764 keV)	15.3	1660 - 1860
Thorium	^{208}Tl (2614 keV)	99.7	2410 - 2810

4.1.3.2 Determination of specific activity and minimum detectable activity

Using the stripping method, stripping ratios are used to estimate the net count rates in natural radionuclide windows and the corresponding radio-element concentrations (IAEA, 2003). The stripping ratios b and g are assumed to be zero ($b = g = 0$) so that the net count rates, of the j^{th} element in specific window i are given by Eqs. 4.8 - 4.10, and the concentrations by Eq. 4.11.

$$n_{3\mathrm{Th}} = \frac{n_3 - n_{3\mathrm{BG}} - a\left(n_2 - n_{2\mathrm{BG}}\right)}{1 - \alpha a} \tag{4.8}$$

$$n_{2\mathrm{U}} = n_2 - n_{2\mathrm{BG}} - \alpha n_{3\mathrm{Th}} \tag{4.9}$$

$$n_{1\mathrm{K}} = n_1 - n_{1\mathrm{BG}} - \beta n_{3\mathrm{Th}} - \gamma n_{2\mathrm{U}} \tag{4.10}$$

$$c_{\mathrm{K}} = \frac{n_{1\mathrm{K}}}{s_{1\mathrm{K}}} \qquad c_{\mathrm{U}} = \frac{n_{2\mathrm{U}}}{s_{2\mathrm{U}}} \qquad c_{\mathrm{Th}} = \frac{n_{3\mathrm{Th}}}{s_{3\mathrm{Th}}} \tag{4.11}$$

As the PGIS-2 spectrometer provides for automatic correction of dead time (PEI, 2013a), the number of counts (N) in a particular window for a specific count time (t) are converted directly to count rate, $n = {}^{N}/_{t}$ (cps) and related to radio-element concentration using the stripping method (Eq. 4.2). Conversion of the radio-element concentrations to specific activity is specified in Table 4.2 by IAEA (1989).

Table 4.2: Conversion of radio-element concentration to specific activity (source: IAEA (1989))

Radio-element concentration	Specific activity
1 % K	313 Bq kg^{-1}(^{40}K)
1 ppm eU	12.35 Bq kg^{-1}(^{238}U or ^{226}Ra)
1 ppm eTh	4.06 Bq kg^{-1}(^{232}Th)

The Currie method (Currie, 1968) was used to calculate minimum detectable activity (MDA) of the PGIS-2 spectrometers. Relatively high MDA were obtained for real-time measurements at 90 % confidence level, as indicated in Table 4.3. Furthermore, the robust regression on order statistics (ROS) method (Helsel *et al.*, 2005) was used to summarize censored datasets i.e. data consisting of activity concentrations reported below the MDA. The method computes a linear regression equation on a probability plot using uncensored observations and uses model predicted values of both censored and uncensored data to compute summary statistics.

Table 4.3: MDA for PGIS-2 spectrometers for 1 s measurement, 1 m above the ground at 90 % confidence level (source: PEI (2015))

	^{40}K		^{238}U		^{232}Th	
Spectrometer	Bq kg^{-1}	% K	Bq kg^{-1}	ppm eU	Bq kg^{-1}	ppm eTh
PGIS-128	202	0.645	45	3.6	27	6.7
PGIS-21	470	1.502	112	9.1	64	15.8

4.1.4 Estimation of absorbed dose-rate and radiation risk factors

The total absorbed dose-rate, D (Eq. 4.12) in air (1 m above a plane assuming an infinite homogeneous soil medium) is calculated by transforming measured activity concentrations (A_U, A_{Th}, A_K) using conversion factors specified by UNSCEAR (2000). The annual effective dose estimate, $AEDE$ (Eq. 4.13) is a factor of D, the quotient of annual effective dose received by adults to absorbed dose-rate (0.7 Sv Gy^{-1}), the outdoor occupancy factor in this case, 0.4 determined for populations living in rural areas of Kenya by Mustapha (1999), and number of hours in a year (8,760).

$$D\left(nGy\,h^{-1}\right) = 0.462A_U + 0.604A_{Th} + 0.042A_K \tag{4.12}$$

$$AEDE\,(mSv) = D \times 0.7 \times 0.4 \times 8760 \tag{4.13}$$

The external hazard index of $\gamma-$ray radiation due to NORM, H_{ex} (Eq. 4.14), which must be less than unity in order to keep the radiation hazard insignificant, corresponds to an annual dose limit of 1.0 mSv for the general population, and is obtained from the upper limit of radium equivalent activity (370 Bq kg^{-1}) (Beretka and Mathew, 1985).

$$H_{ex} = \frac{A_U}{370} + \frac{A_{Th}}{259} + \frac{A_K}{4810} \tag{4.14}$$

Excess lifetime cancer risk ($ECLR$) representing the number of extra cancers expected within a given human population exposed to ionizing radiation at a given dose is defined by Eq. 4.15 (Abbaspour *et al.*, 2010).

$$ECLR = H \times LS \times PC \tag{4.15}$$

Where H is AEDE, LS is the average lifespan (estimated to 70 years) and PC is the nominal probability coefficient for detriment-adjusted cancer risk of 0.055 Sv^{-1} for members of the public (ICRP, 2007).

4.2 The study area

The south coastal region is located in the south-eastern corner of Kenya in Kwale County, and is bound by latitudes of 4° 15' and 4° 45' S and longitudes of 38° 59' and 39° 35' E, as shown in Fig. 4.5. The study area is categorized into two broad sites, namely south coast paved road and adjoining environs and the Mrima-Kiruku complex.

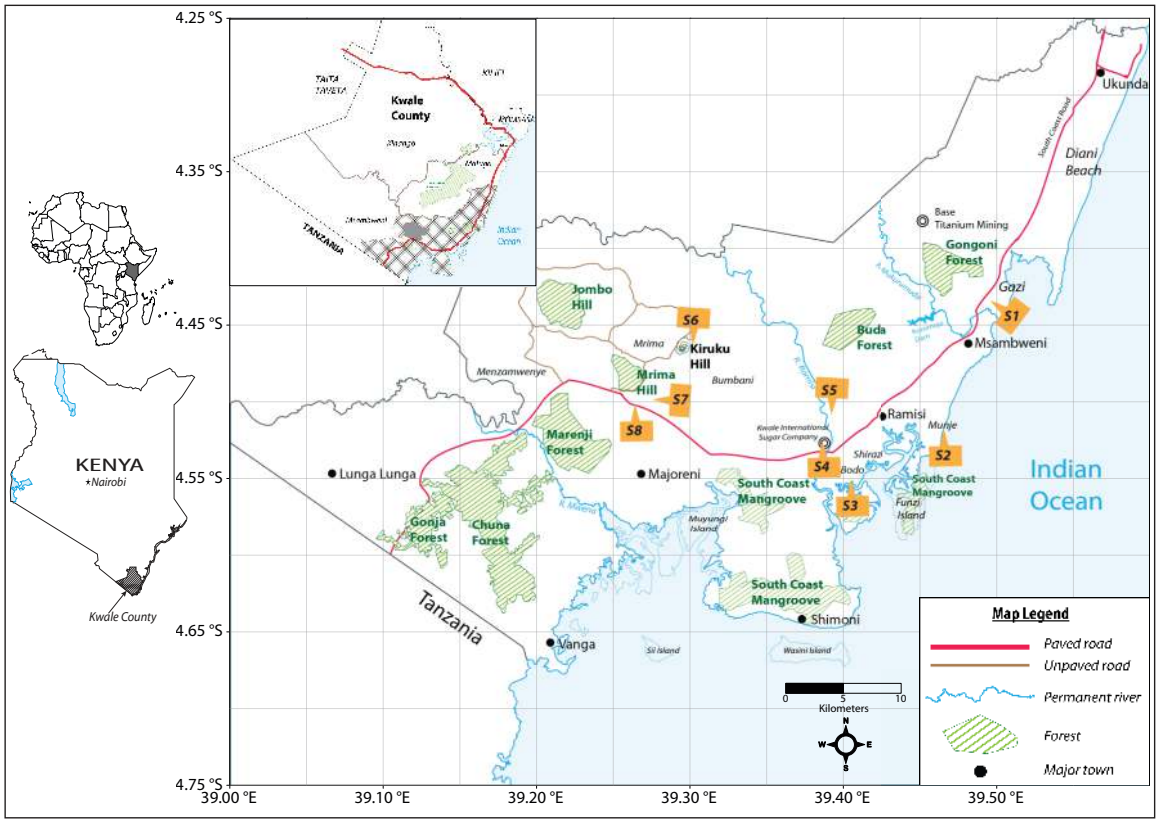

Fig. 4.5: Map of south coastal Kenya indicating various geographical features. Eight sites (S1 - S8) are also pictorially illustrated in Fig. B.1 in Appendix B.1.

4.2.1 Survey of the south coast paved road and environs

The south coast paved road section surveyed stretches approximately 40 km from Gazi to Mwangwei, almost 10 km inland from the Indian Ocean, as shown in Fig. 4.6. While transiting the south coast paved road, several stops were made at selected sites, namely Gazi, Ramisi Islamic Centre, Ramisi sand quarry (about 1.7 km from the main road)

and Bwiti Junction, to perform extended ground-based radiometric measurements. The Indian Ocean (Fig. 4.6) was also surveyed along the Munje and Bodo beaches.

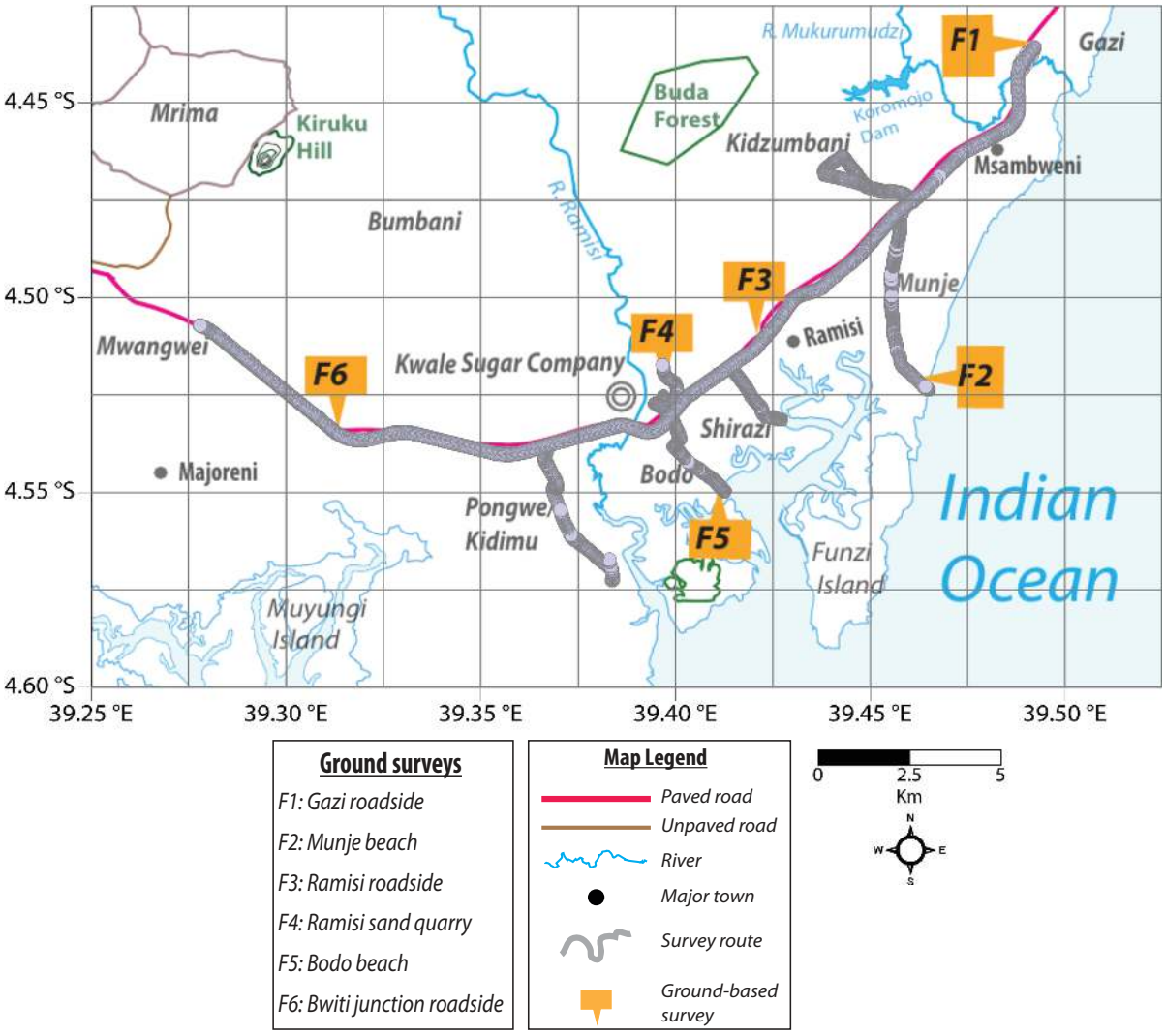

Fig. 4.6: Map indicating surveyed sites along the south coast road and environs. Field samples were collected from sites F2 - F6 (see Table B.1 in Appendix B.4).

4.2.2 Survey of the Mrima-Kiruku complex

At the time of the survey, a major part of Mrima Hill was inaccessible due to the dense vegetation and forest, so a vehicular survey was carried out from the western forest entrance up to the first saddle-back peak and along the off-roads surrounding the hill, as shown in Fig. 4.7. As follow up to an earlier study by Kebwaro (2009), ground based measurements were conducted in seven sites (Fig. 4.7) located around Mrima Hill.

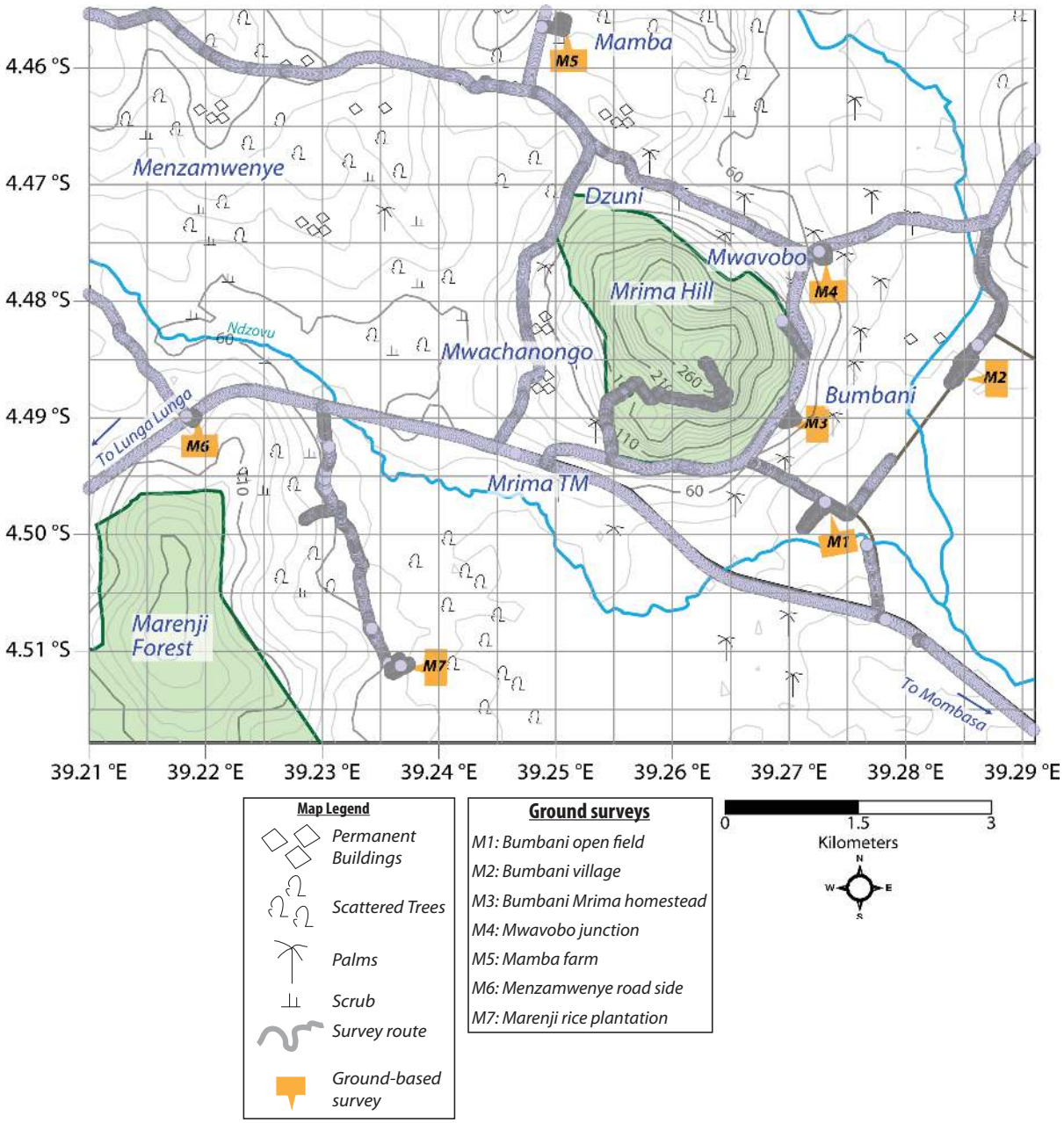

Fig. 4.7: Map indicating survey of Mrima Hill and the environs. Field samples were collected from sites M1, M3, M6 - M7 (see Table B.1 in Appendix B.4).

In Kiruku Hill, bare soil and rock outcrops on the hill summit in addition to multiple farming activities along the hill slopes were observed at the time of survey. Kiruku Secondary School is located approximately 300 m from the base of the hill and at the time was surrounded by ploughed fields and maize plantations. A ground based survey was carried out starting from the school covering the foot-accessible sections of the hill, and the dry weathered road leading to the trading center, as shown in Fig. 4.8.

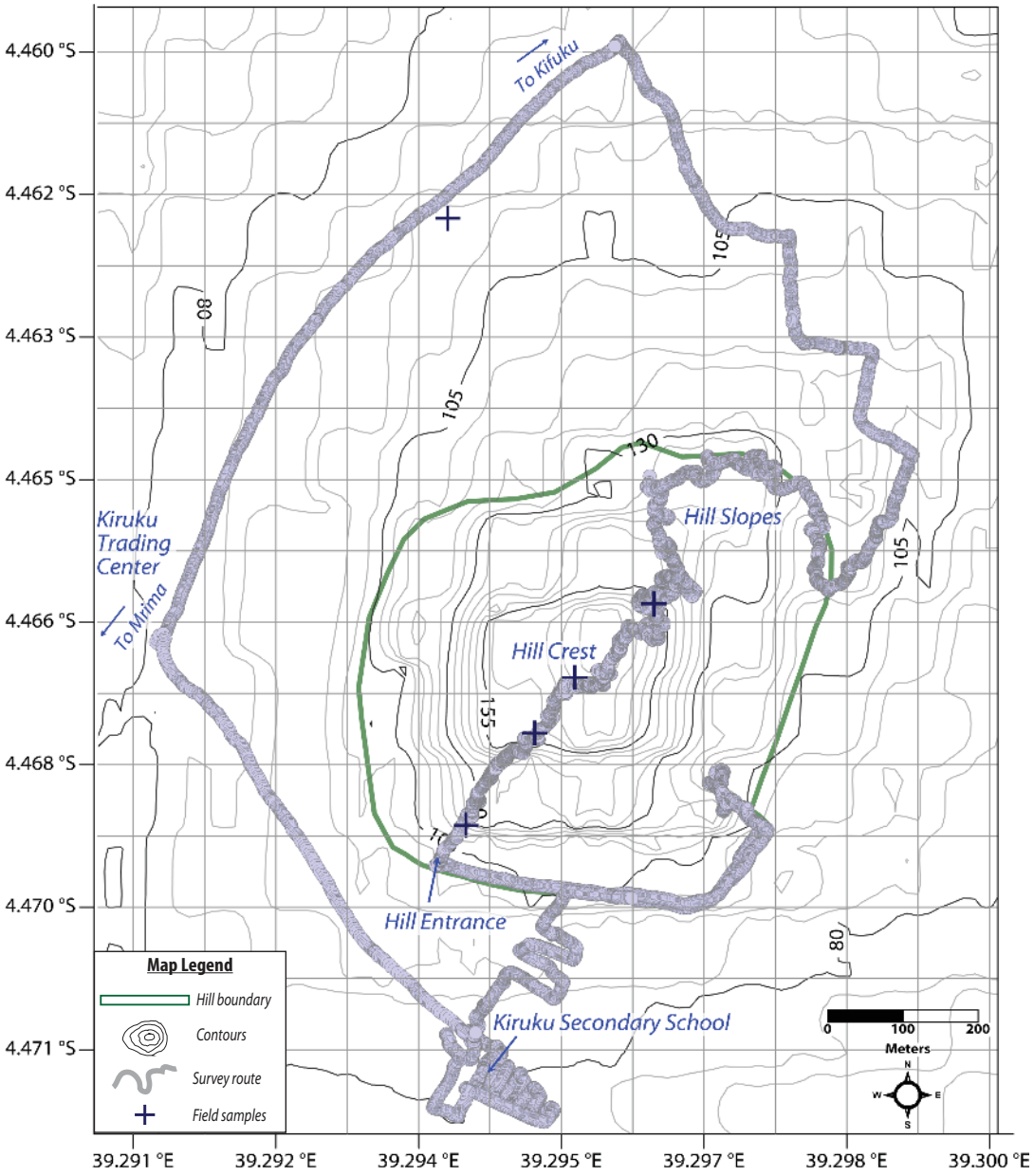

Fig. 4.8: Map indicating survey and field sampling on Kiruku Hill and the foothills (see sample descriptions in Table B.1 in Appendix B.4).

4.2.3 Spatial mapping of gamma dose-rates

Vectorized base maps were created using Adobe Illustrator CS5.1 (Adobe Systems) utilizing the available satellite imagery, geological raster maps and topographical sheets which were digitized using Didger5 (Golden Software, Inc.), while gamma dose-rate maps were created using Surfer13 (Golden Software, LLC).

The classed post map technique was applied to show spatial distribution of geo-referenced dose-rates using round symbols, and group them into colour coded discrete classes (see Table 4.4). The scheme used to represent specific dose-rate ranges was defined based on two regulatory limit criteria, namely world population weighted average of 60 nGy h^{-1} and dose-rate limit for the general public of 114 nGy h^{-1} (UNSCEAR, 2000). Gamma radiation hot spots in this work are defined as those that exceeded 5 times the dose-rate limit for the general public.

Table 4.4: Scheme for map colour coding of gamma dose-rate measurements

Colour	Dose rate range (nGy h^{-1})	Description
Blue	0 - 60	Within world population weighted average
Green	60 - 120	Within general public dose-rate limit (114 nGy h^{-1})
Yellow	120 - 360	Up to 3 times higher than general public dose-rate limit
Orange	360 - 600	3 - 5 times higher than general public dose-rate limit
Red	> 600	Over 5 times higher than general public dose-rate limit (hotspot)

The Kriging technique was used to perform interpolation (gridding) of measured gamma dose-rates in selected sites, using the nearest sampling points (grid nodes) and a maximum searching distance equal to the range distance of the determined grid node values (GoldenSoftware, 2015). The grids were then used to generate spatial maps of the sites utilizing the semi-variogram model (Webster and Oliver, 2007).

4.2.4 Exploratory analysis of *in-situ* radiometric measurements

The conceptual framework used for the multivariate exploratory analysis of *in-situ* radiometric measurements in the study area, is presented in Fig 4.9. PCA and ternary plots were realized utilizing R software (GNU General Public License); pre-processing of the PCA data was undertaken to obtain a new set of suitably weighted variables through mean-centering and log-scaling, prior to the analysis. This was necessary in order to achieve equal statistical influence of the variables and reduce the amount of data by eliminating irrelevant sources of variation.

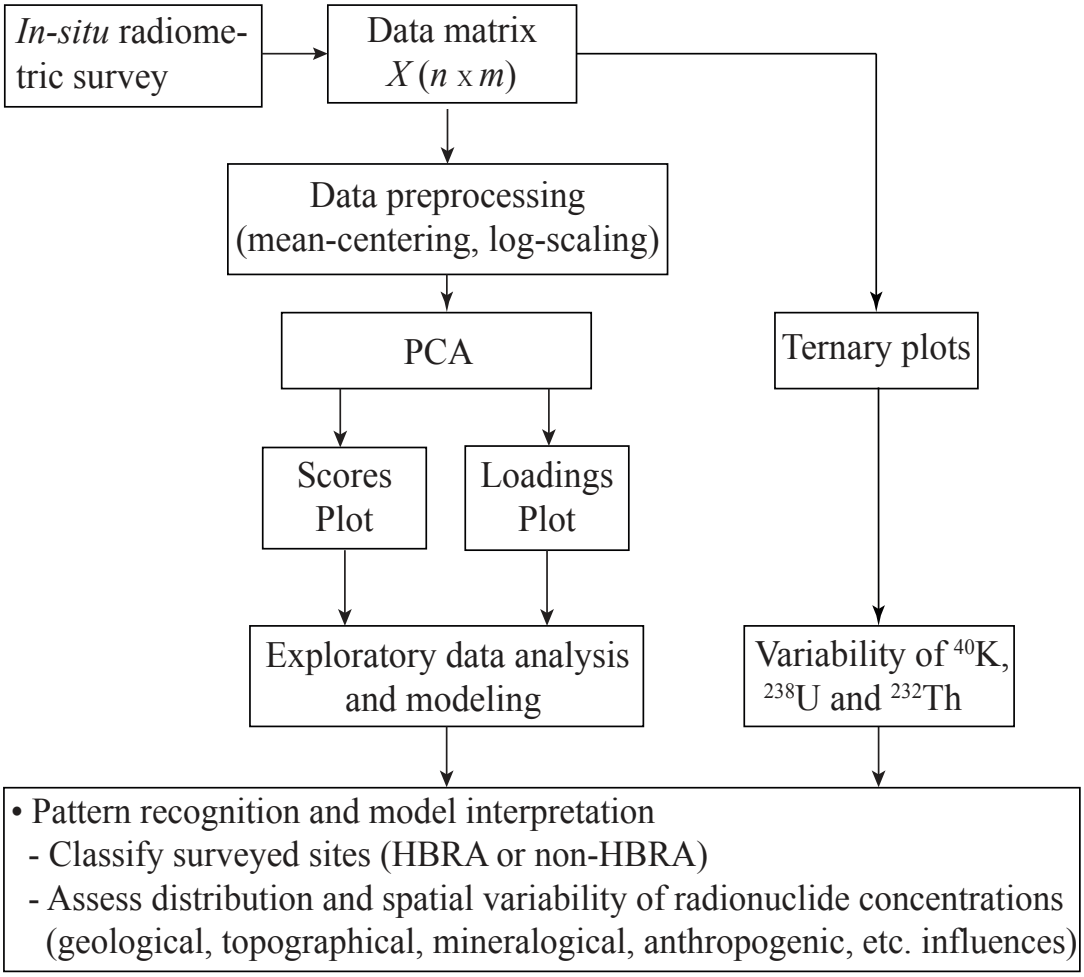

Fig. 4.9: Conceptual framework used for the multivariate exploratory analysis of *in-situ* radiometric measurements in the study area using PCA and ternary plots. The data matrix $X\,(n \times m)$ represents n radiometric measurements each having m (^{40}K, ^{238}U and ^{232}Th) variables.

4.3 Laboratory EDXRF spectrometric measurements

A total of 31 geological samples (19 soil, 7 rocks and 5 sediments) were collected for laboratory EDXRF analysis (see Table B.1 in Appendix B.4), to complement the *in-situ* radiometric measurements and to help ascertain the mineral structure of the study area. Surface soil samples (15 - 20 cm) were scooped at various sites of interest including sand mines, the Indian Ocean beach and farmlands, following the ISO 18589-2 (ISO, 2007) procedures. Rock samples were picked from Kiruku Hill, wastes at quarries and at the Indian Ocean coastline, while sediments were scooped along the bottom of the surface water bodies such as streams and rivers in the upstream direction. Test sample preparation involved: homogenizing, splitting and selecting a specific range of grain size for analysis and storage.

4.3.1 Sample preparations

Physical processing of the samples (see Fig. B.5 in Appendix B.4) required drying, crushing, sieving and homogenizing which were based on ISO 18589-2 (ISO, 2007) procedures. Soil samples were weighed and then spread in a thin layer of 1 - 2 cm on flat containers and left for 3 weeks to air dry at ambient room temperature. A 2 mm sieve was used to separate fine soil (< 2 mm) from coarse rock fragments. Rock fragments weighing $> 5\%$ of total soil mass were also considered for analysis based on recommendations given by Anderson and Ingram (1993). The rock samples were crushed to grain sizes < 2 mm using a rock crusher while the sediment samples were weighed and placed in open containers for air drying for at least 3 days before sieving. Thereafter, all samples (soil, rock and sediments) were ground further to fine size using pestle and mortar, sieved using a 0.5 mm sieve before oven-drying at a temperature of 105 ± 10 °C overnight, and put in a desiccator to expel moisture.

Approximately 50 g of each sample was ground further to < 60 μm grain size required for EDXRF analysis (IAEA, 1997) using a tungsten carbide pulverizer. Duplicate samples of 2.5 g were drawn and mixed with paraffin powder (10% by weight to sample)

for binding by blending thoroughly using pestle and mortar. The mixture was pressed to pellets of 25 mm diameter, weighing about 2.75 g by applying a load between 15 and 20 tons. Several certified reference materials from USGS and IAEA with similar matrix compositions, were also prepared to test the accuracy of the EDXRF method.

4.3.2 EDXRF spectrometer set-up

The Spectro X-Lab 2000 (Spectro Analytical Instruments, GmbH) tube-excited polarized EDXRF spectrometer (set-up shown in Fig. 4.10 and pictorial illustrations shown in Fig. B.6, Appendix B.4) was used for the elemental analysis of geological samples. It is equipped with a 400 W Rh end window X-ray tube which has a 75 μm Be window, and a Si(Li) semiconductor detector with a resolution < 150 eV (1000 cps Mn K_α) coupled to a charge sensitive preamplifier (Spectro, 2000).

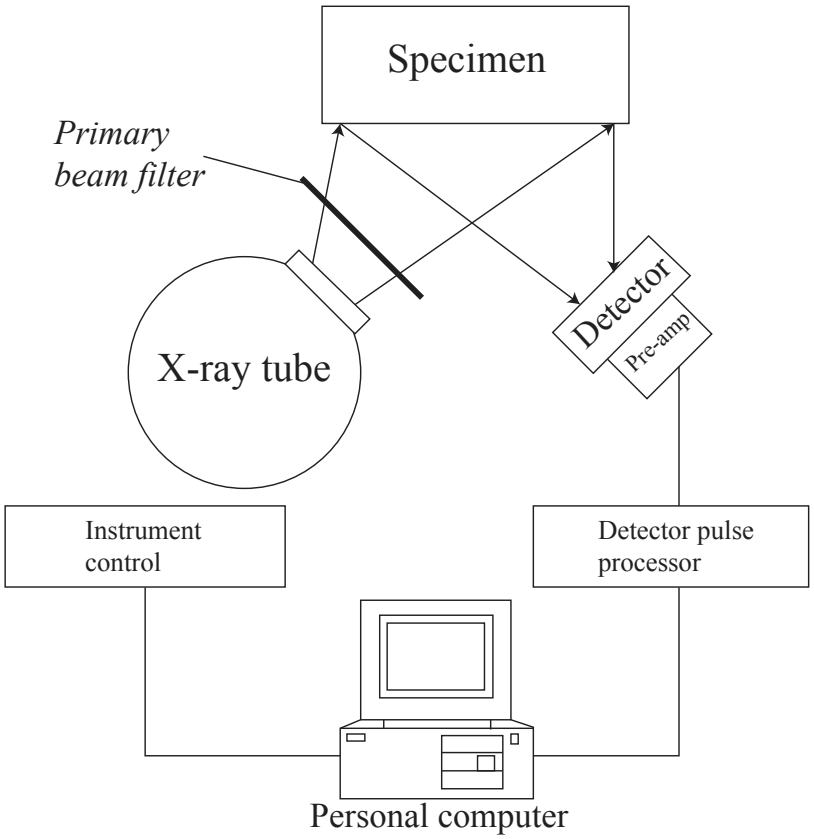

Fig. 4.10: Set-up of the tube-excited polarized EDXRF spectrometer (adapted from: van Grieken and Markowicz (2001)). Operation of the irradiation chamber is usually under vacuum or He gas purge.

Incident photons striking the detector from the specimen are converted to voltage pulses (with amplitudes proportional to photon energies), which are transmitted via the preamplifier to the detector pulse processing unit which consists of the main amplifier, ADC and MCA. The MCA accumulates EDXRF spectra of the sequential events which are stored in the personal computer.

Selective excitation of the secondary fluorescence radiation beam (with reduced scatter) is achieved by polarizing the primary beam under orthogonal conditions and generating monochromatic radiation using secondary targets. Consequently, in addition to enhanced excitation of low-Z elements with relative reduction in measurement times, the detector processes more fluorescent radiation improving the elemental detection limits and sensitivities by a factor of 4 - 7 (Spectro, 2000).

The primary beam is polarized by Barkla scatter with Al_2O_3 target and Bragg diffraction with a highly oriented pyrolytic graphite (HOPG) target. Mo, Co and Pd were used as secondary targets to produce near monochromatic radiation that was used to excite the specimens. The specific measurement conditions are summarized in Table 4.5. Spectra analysis was performed by the SUPEX software based on the fundamental parameters method for intermediate thick samples (van Grieken and Markowicz, 2001).

Table 4.5: Characteristics of polarizer and targets used in Spectro X-Lab 2000 EDXRF spectrometer for pressed discs

Type	Excited elements (Z)	Applied voltage (kV)	Applied current (mA)	Measurement time (s)
HOPG (Bragg polarizer)	11-17	15	13	500
Al_2O_3 (Barkla target)	47-60	50	5.6	300
Mo (secondary target)	26-38 and 72-83	40	3	700
Co (secondary target)	19-25	35	4	300
Pd (secondary target)	39-42 and 90-92	40	1.9	300

Chapter 5

Results and Discussion

This chapter presents the results of the *in-situ* $\gamma-$ray and EDXRF spectrometric measurements. A comparison of the *in-situ* radiometric results with other related studies in the region and elsewhere, is also presented. In the end, results of multivariate analysis of the activity concentration values are presented.

5.1 Results of gamma dose-rates

This section presents the results of a systematic assessment of gamma dose-rates in the study area. Measured dose-rates were overlaid on geo-referenced base topographical and geological maps[1] to capture landscape, geology and spatial variability of the measurements. It was observed that dose-rates in the south coast paved road and environs generally increase with proximity to the main paved road which implies that the roadbed material contains elevated radioactivity levels. The spatial variability in measured dose-rates within the Mrima-Kiruku complex was found to correspond mainly with the underlying geology, with increments observed toward the summits of Mrima and Kiruku Hills which implies that the complex is a geogenic HBR anomaly.

[1]Map legends for surveyed sites are presented in Fig. B.2, Appendix B.1.

5.1.1 Evaluation of performance for the PGIS-2 detectors

The spectral responses for PGIS-21 and PGIS-128 detectors was evaluated by comparing stationary dose-rates measured for 60 s on a background calibration pad and at approximately 1 m above concrete, see Table 5.1. Despite the difference in crystal volumes and hence sensitivity to $\gamma-$rays, the measurements were relatively comparable with precision better than 6.1% RSD. Spectra obtained by the detectors (600 s measurements) on the background calibration pad, are shown in Fig 5.1.

Table 5.1: Comparison of spectral responses for PGIS-21 and PGIS-128 detectors

	Dose rate (nGy h^{-1})		Statistics		
	PGIS-21	PGIS-128	Mean	SD	RSD (%)
Background calibration pad	79	72	76	4	5.7
Warehouse (1 m above concrete)	65	59	62	4	6.1

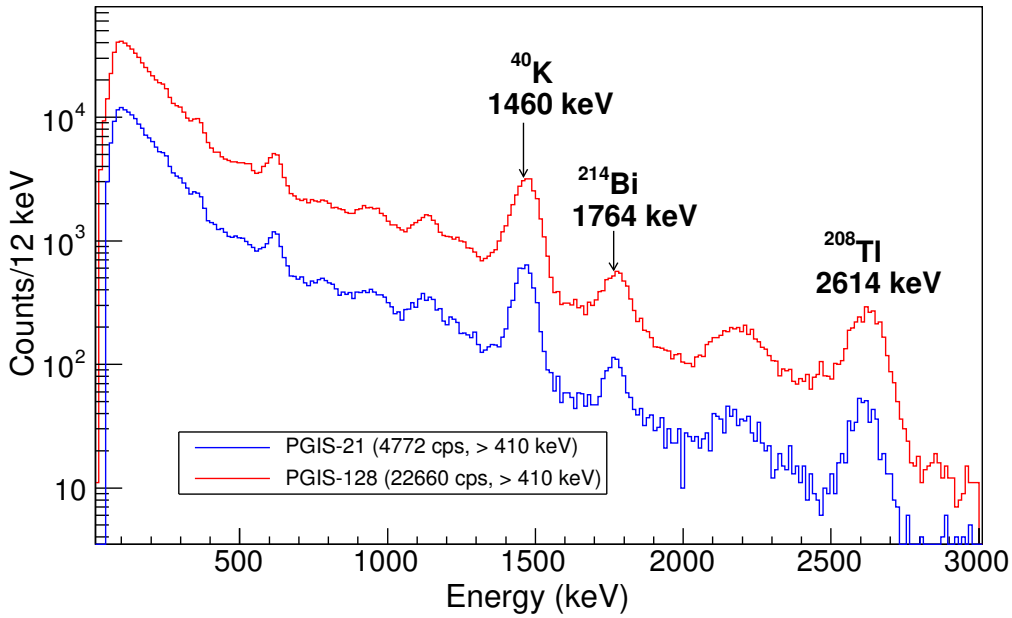

Fig. 5.1: Spectra obtained from background calibration pad measured with the PGIS-21 (0.347 l) and PGIS-128 (2.0 l) detectors for 600 s. The PGIS-128 detector has higher sensitivity compared to PGIS-21.

5.1.1.1 Comparison of stationary and *in-situ* gamma dose-rates

A comparison of stationary and *in-situ* dose-rate measurements was evaluated based on readings taken at Kiruku Hill by the PGIS-128 detector. Readings within 10 m radius of the stationary measurement points were averaged with accumulation times of 176 s and 199 s at point A and B, respectively (Table 5.2). The results show a low standard deviation < 10 between the two measurements with precision better than 1% RSD.

Table 5.2: Comparison of *in-situ* and stationary dose-rate measurements by PGIS-128. Mean values of *in-situ* readings are indicated in brackets

	Dose rate (nGy h^{-1})		Statistics		
	In-situ	Stationary[†]	Mean	SD	RSD (%)
Point A	1021 - 1144 (1056)	1043	1050	9	0.9
Point B	1364 - 1904 (1719)	1713	1716	4	0.2

[†]Readings accumulation time was 120 s

5.1.1.2 Variation of dose-rates with detector to ground distance

Three dose-rate stationary readings by the PGIS-128 were taken at a southern foothills of Mrima Hill site for 10 s and at three different detector geometries, see Table 5.3. A 500 nGy h^{-1} difference between point 1 and point 2 readings was observed and attributed to vehicle shielding effect (IAEA, 2003). Consequently, a shielding factor of 1.714 was used to correct the vehicular dose-rate measurements and corresponding natural radionuclide activity concentrations ($A_U = 0.792$, $A_{Th} = 1.035$ and $A_K = 0.072$).

Table 5.3: Detector to ground stationary dose-rate measurements by PGIS-128

Detector-to-ground distance	Dose rate (μGy h^{-1})
Point 1 (≈ vehicle position)	0.7
Point 2 (≈ 1 m above ground)	1.2
Point 3 (0 m above ground)	1.3

5.1.2 Gamma dose-rates in the south coast paved road and adjoining environs

The gamma dose rate mapping for surveyed areas of the south coast paved road and adjoining environs survey is shown in Fig. 5.2.

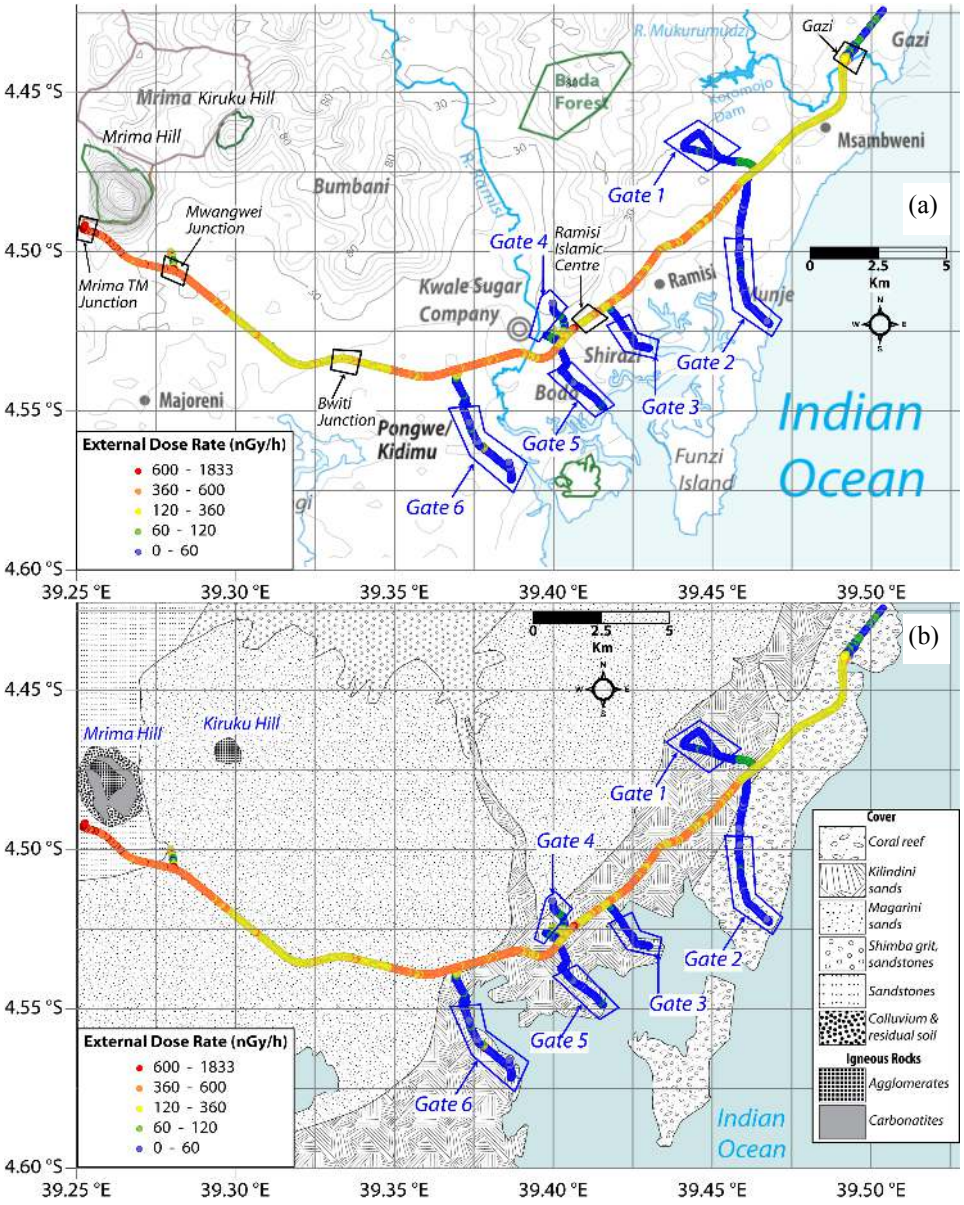

Fig. 5.2: Gamma dose-rate mapping for the south coast road and environs overlaid on (a) topographic and (b) geological (adapted from: Caswell (1953) and JICA (1993)) maps. *In-situ* $\gamma-$ray spectra were aggregated in gates 1 - 6.

Dose-rates measured along the south coast paved road section from Kwale township to Gazi via Diani and Ukunda (not shown in Fig. 5.2), and in the non-paved roads, namely Kidzumbani, Munje, Shirazi, Ramisi, Bodo and Pongwe/Kidimu (i.e. gate 1 - 6) were below the world population weighted average (< 60 nGy h^{-1}). The region is mostly underlain by sediments (grit, sands, shales, siltstones) of the Duruma Sandstone Series (Caswell, 1953; Horkel *et al.*, 1984) and thus the low gamma dose-rates can be attributed to accumulation of quartz in sediments which is considered to be radioactively barren (Wilford *et al.*, 1997). However, a sharp increase in dose-rate by a factor of 2 - 6 times was noted along the south coast paved road at the Mukurumudzi river bridge approach in Gazi (approximately 23 km from Ukunda town), as shown in Fig. 5.3 (a) and (b). From this point onward up to the Menzamwenye junction (past Mrima TM center), measured dose-rates were > 120 nGy h^{-1}, as shown in Fig. 5.2. It may also be noted that much higher dose-rates (i.e. > 360 nGy h^{-1}) were measured along various sections of the paved road which indicates abrasion in the bitumen paving.

Ground-based measurements were conducted approximately 20 m from both sides of the road at Ramisi Islamic center (located approximately 13 km from Gazi) and Bwiti junction (located approximately 9 km from Ramisi) to examine the extent of the HBR anomaly, as shown in Fig. 5.4 (a) and (b). The measurements at the Ramisi Islamic center showed that the high dose-rates (> 230 nGy h^{-1}) were confined to the paved road and road shoulders while adjoining roadside areas, approximately 10 m from the paved road, indicated $\leqslant 60$ nGy h^{-1}, as shown in Fig. 5.4 (b). At the Bwiti junction (Fig. 5.4 (c)), high dose-rates (> 250 nGy h^{-1}) were also measured along the paved road and road shoulders. The adjoining murram road and side-road intersecting the main road indicated even higher dose-rates (> 600 nGy h^{-1}). Similar anomalies were also noted at other side road intersections and bus stops located at the Mwangwei and Mrima TM road junctions, as shown in Fig. 5.4 (c) and (d). These areas can be classified as gamma radiation hot spots.

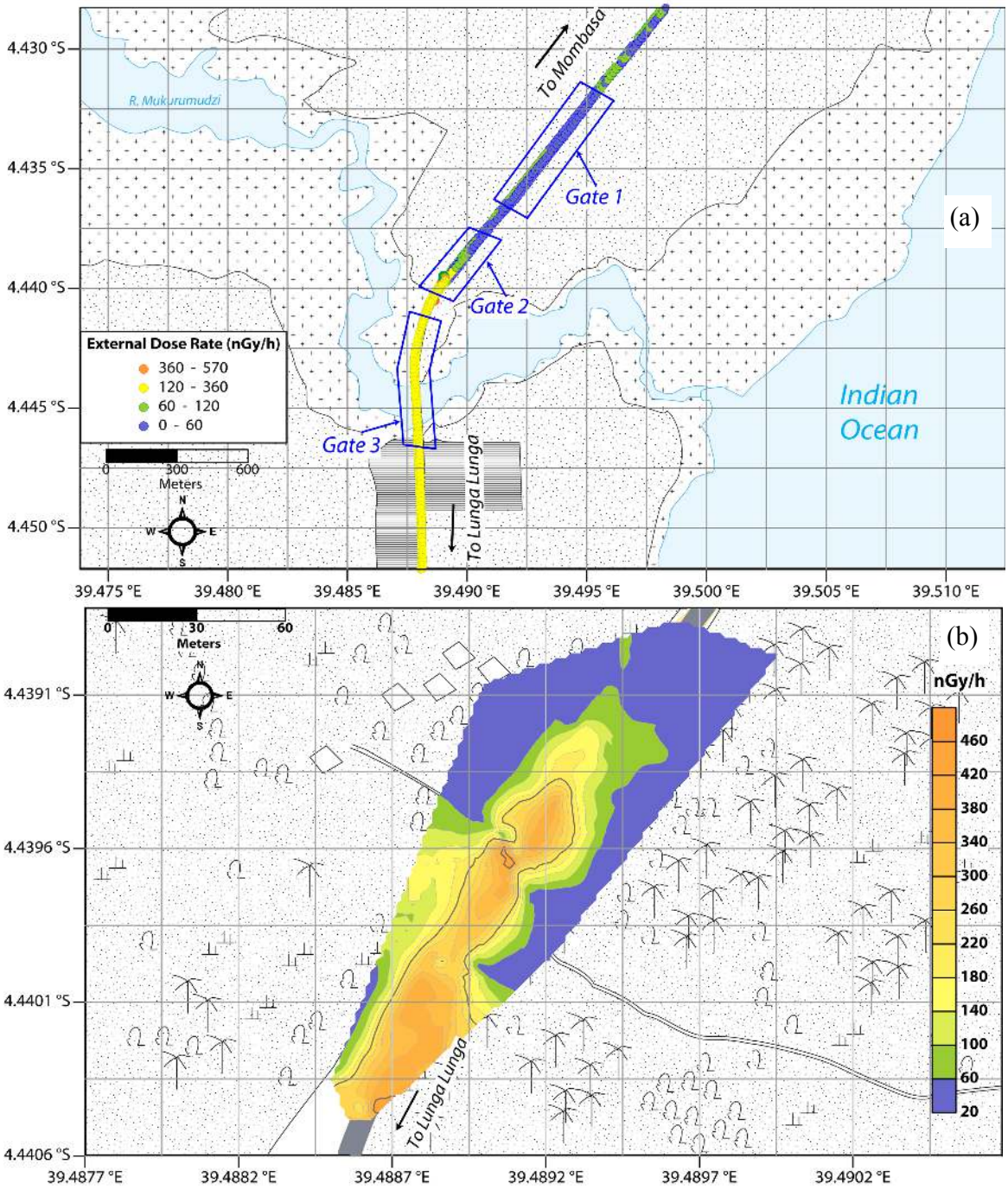

Fig. 5.3: (a) Gamma dose-rate mapping for the south coast paved road section in Gazi ($\gamma-$ray spectra were aggregated in gate 1 - 3), and (b) Dose-rate interpolation by Kriging technique for ground based measurements conducted in Gazi along the road and at the roadside.

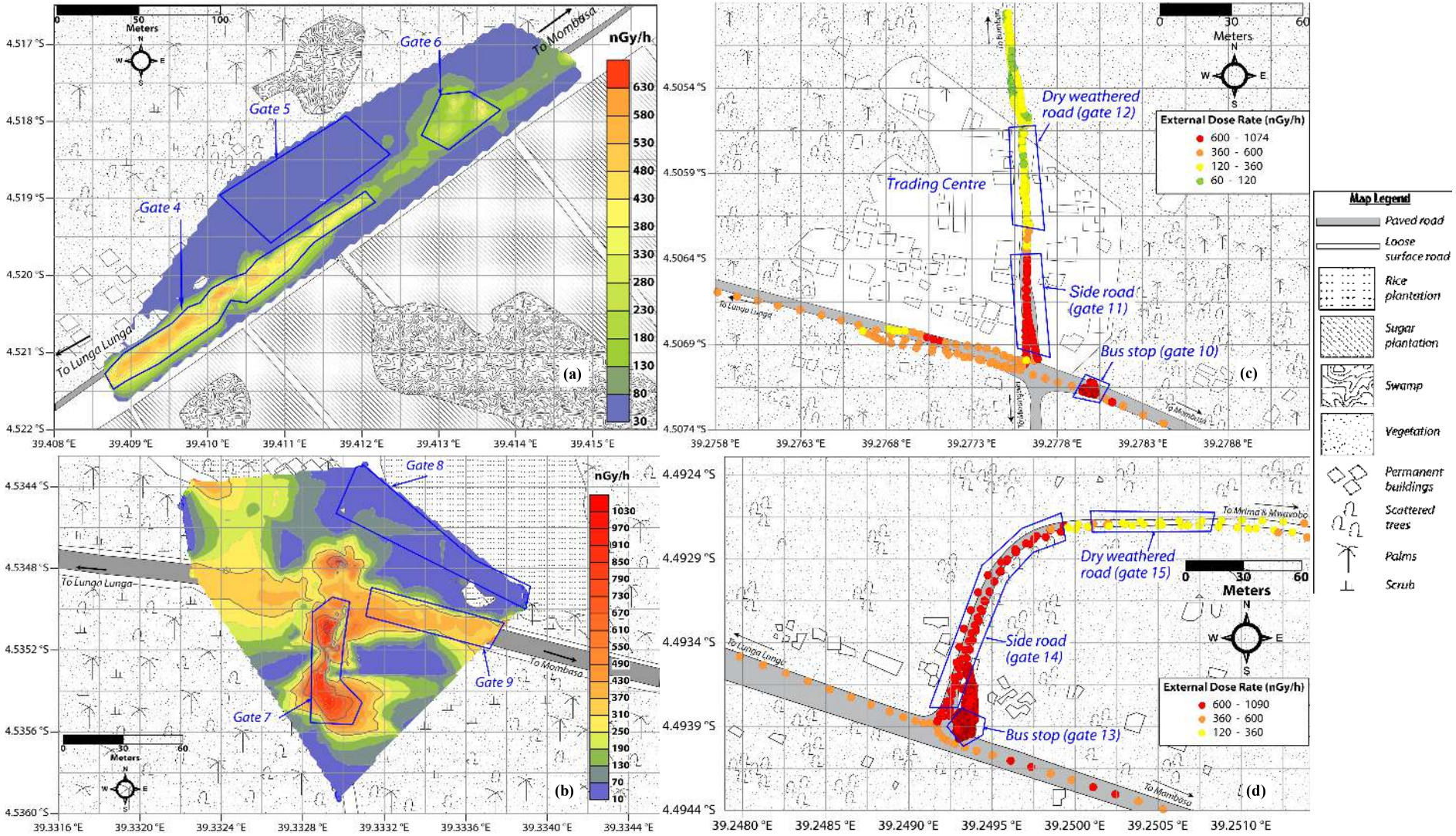

Fig. 5.4: Gamma dose-rate mapping for (a) Ramisi Islamic center roadside, (b) Bwiti junction roadside, (c) Mwangwei junction and (d) Mrima TM junction. *In-situ* $\gamma-$ray spectra were aggregated in gates 4 - 15.

The results obtained show a dependence of gamma dose-rates with proximity to the main paved road, implying that it was the murram roadbeds that contained elevated radioactivity levels. It was further observed at the time of survey that bitumen paving on these side-road intersections were abraded thus exposing the underlying murram roadbed[2]. It was thus concluded that the roadbed murram was non-indigenous and must have been ferried from a HBRA, possibly the Mrima Hill which is situated approximately 1 km from the Mrima TM junction (see Fig. 5.2 (a)). Furthermore, the bitumen surface along the main paved road in addition to acting as a shielding layer attenuating $\gamma-$rays beneath also prevents weathering of roadbed murram, hence the relatively lower dose-rates on the main road compared to the side road intersections (Fig. 5.4 (b) - (d)).

Baker (1953) reported the presence of huge iron, manganese and REE rich laterite (locally known as murram) deposits of sedimentary origin containing radioactive mineral ores, such as monazite and pyrochlore on the lower slopes of Mrima Hill. Later, Mangala (1987) and Patel (1991) also observed several murram pits and trenches dug on the southern and eastern slopes of the hill suggesting that the dug-murram could have been relocated and exploited for other uses such as road construction. During the Post-Colonial Era in Kenya, laterite was commonly used as an aggregate material for road paving due to local availability and lower cost; such paving was extended about 1.5 - 2 m beyond the edge of the carriageway (Grace, 1991). Some senior residents interviewed at the time of the survey recalled that the south coast road section from Gazi to Lunga Lunga town was paved in 1972 and that murram from Mrima Hill was used as an aggregate material for its paving.

[2]See assorted pictures of the surveyed areas presented in Fig. B.3, Appendix B.2.

5.1.3 Gamma dose-rates in the Jombo complex area

The gamma dose rate mapping for surveyed areas of the alkaline igneous complex of Jombo is shown in Fig. 5.5 and 5.6. It may be noted that measured dose-rates were more than 6 times higher than the world population weighted average (i.e. $\geq$ 360 nGy h^{-1}) along the south coast paved road-section between the Mwangwei and Menzamwenye junctions. However, dose-rates measured along the turn-off to Marenji forest were $<$ 60 nGy h^{-1}.

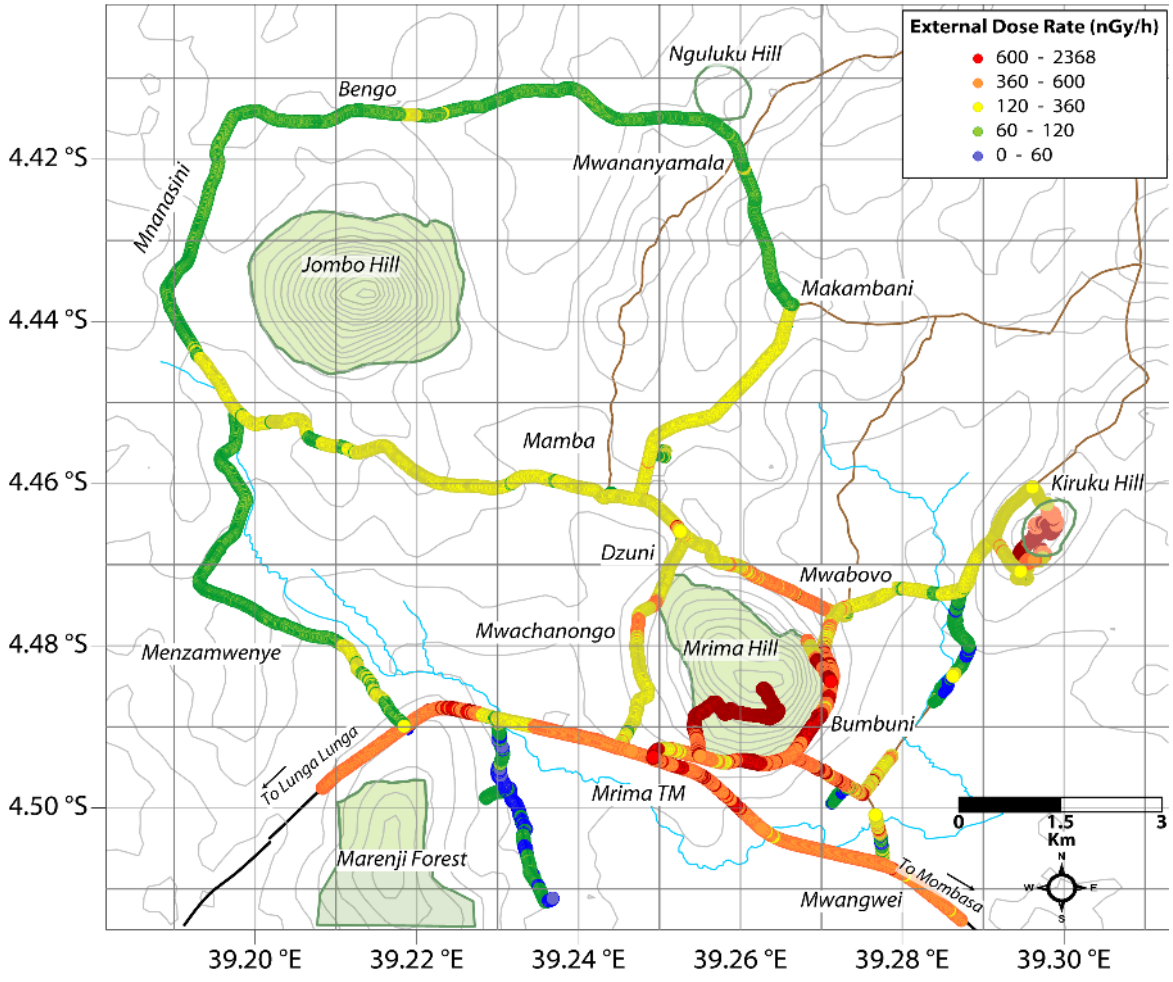

Fig. 5.5: Gamma dose-rate mapping in surveyed areas of the alkaline igneous complex of Jombo.

Along the dry weathered roads surrounding Mrima Hill[3], measured dose-rates ranged $\geq$ 360 - $>$ 600 nGy h^{-1} with several hotspots located between the Mrima TM junction and Mwabovo trading centre. Between the trading centre and Kiruku Hill junction, measured dose-rates ranged $\geq$ 60 - $<$ 360 nGy h^{-1}, and from Dzuni toward the main road via Mwachanongo, dose-rates ranged 63 - 120 nGy h^{-1}. Along the off-roads surrounding Jombo Hill passing through Mamba, Makambani, Mwananyamala, Bengo, Mnanasini and Menzamwenye trading centres, measured dose-rates were however significantly lower compared to those surrounding Mrima Hill (ranged $>$ 60 - $\leq$ 120 nGy h^{-1}). The highest dose-rates ($>$ 1000 nGy h^{-1}) were measured on the summits of Mrima and Kiruku Hills.

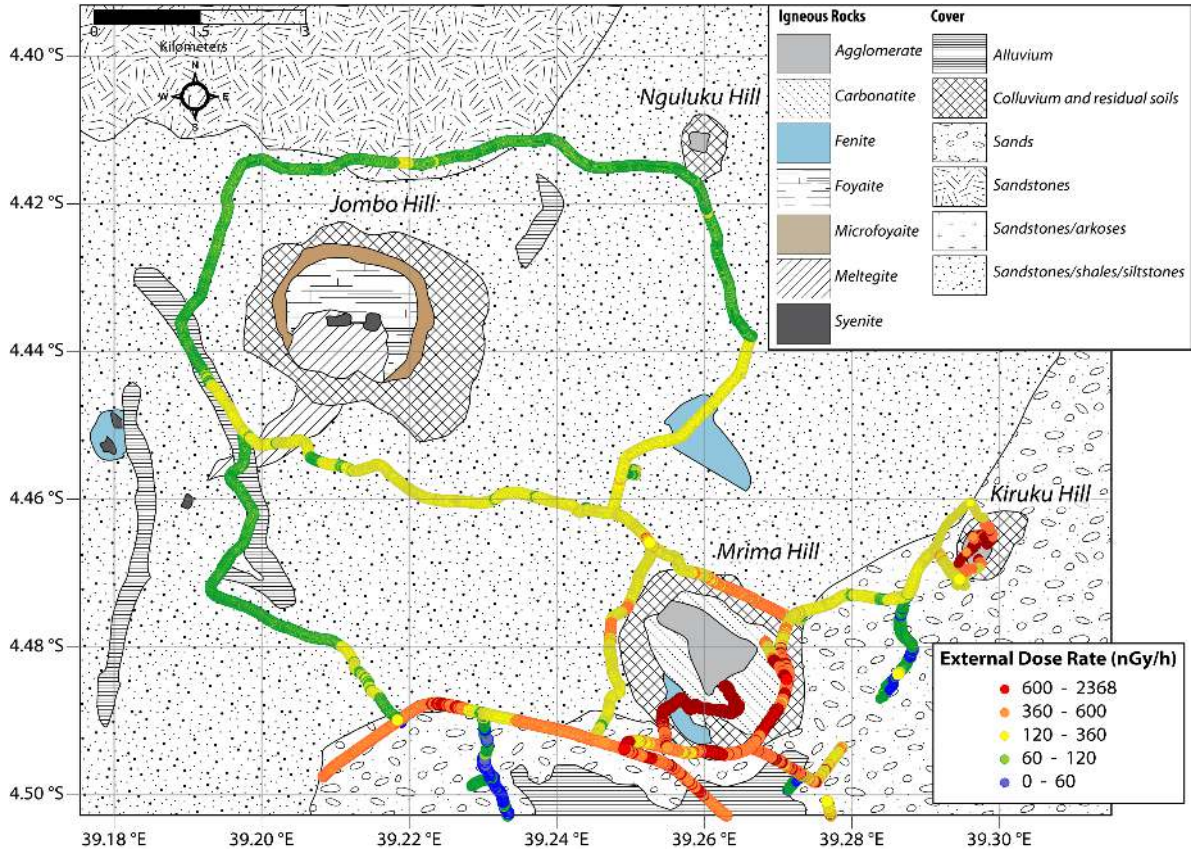

Fig. 5.6: Gamma dose-rates overlaid on the geological (adapted from: JICA (1993)) map of the alkaline igneous complex of Jombo.

The spatial variability in measured dose-rates within the Jombo complex was found to correspond mainly with the underlying geology (bedrock and soil), as shown in

[3]See assorted pictures of the surveyed areas presented in Fig. B.4, Appendix B.2.

Fig. 5.6. It may be observed that the lower dose-rates are associated with sands and sandstones/shales/siltstones, whereas higher dose-rates are associated with colluvium and residual soils, agglomerate and carbonatite rocks. In the sub-sections that follow, Mrima and Kiruku Hills and the Mrima Hill environs are studied in greater detail.

5.1.3.1 Gamma dose-rates on the Mrima and Kiruku Hills

The gamma dose rate maps for the surveyed areas of Mrima and Kiruku Hills are shown in Fig. 5.7 (a, b) and (c, d), respectively. It may be observed that the hot spots of activity in Mrima Hill are located on the hill crest and along the southern hill slopes which are associated with colluvium and residual soils and carbonatite rocks, according to the area's geological report (JICA, 1993). The eastern and northern foothills have relatively lower dose-rates and are associated with sands, sandstones, shales and siltstones. It was also observed that areas located along elevated and sloped terrains (i.e. gate 1 [86 m ASL] and 3 [84 m ASL]) also indicated slightly higher dose-rates compared to depressed terrains (i.e. gate 2 [71 m ASL]).

In Kiruku Hill, hot spots of activity were mostly confined to the hill crest and hill slopes which are associated with agglomerate rocks, colluvium and residual soils. The southern and northern foothills which are associated with sandstones, shales and siltstones have relatively lower dose-rates. In addition to geology, topographical effects (i.e. vegetation, rock outcrops) and anthropogenic activities (i.e. land cultivation, human settlement) were salient features found to influence the radiation exposure levels in the area. The highest dose-rate (1904 nGy h^{-1}) for instance was measured in farm fields located in the northern hill slopes (i.e gate 21). Increments in dose-rate (2 - 4 %) were observed along the southern hill slope (i.e. gate 18) which was characterized by visible signs of erosion and weathering thereby exposing bedrock. Dense vegetation masking the hill crest (i.e. section between gate 18 and 19) was observed to cause attenuation of γ-rays, resulting in slightly lower dose-rates ($<$ 600 nGy h^{-1}) compared to non-masked areas.

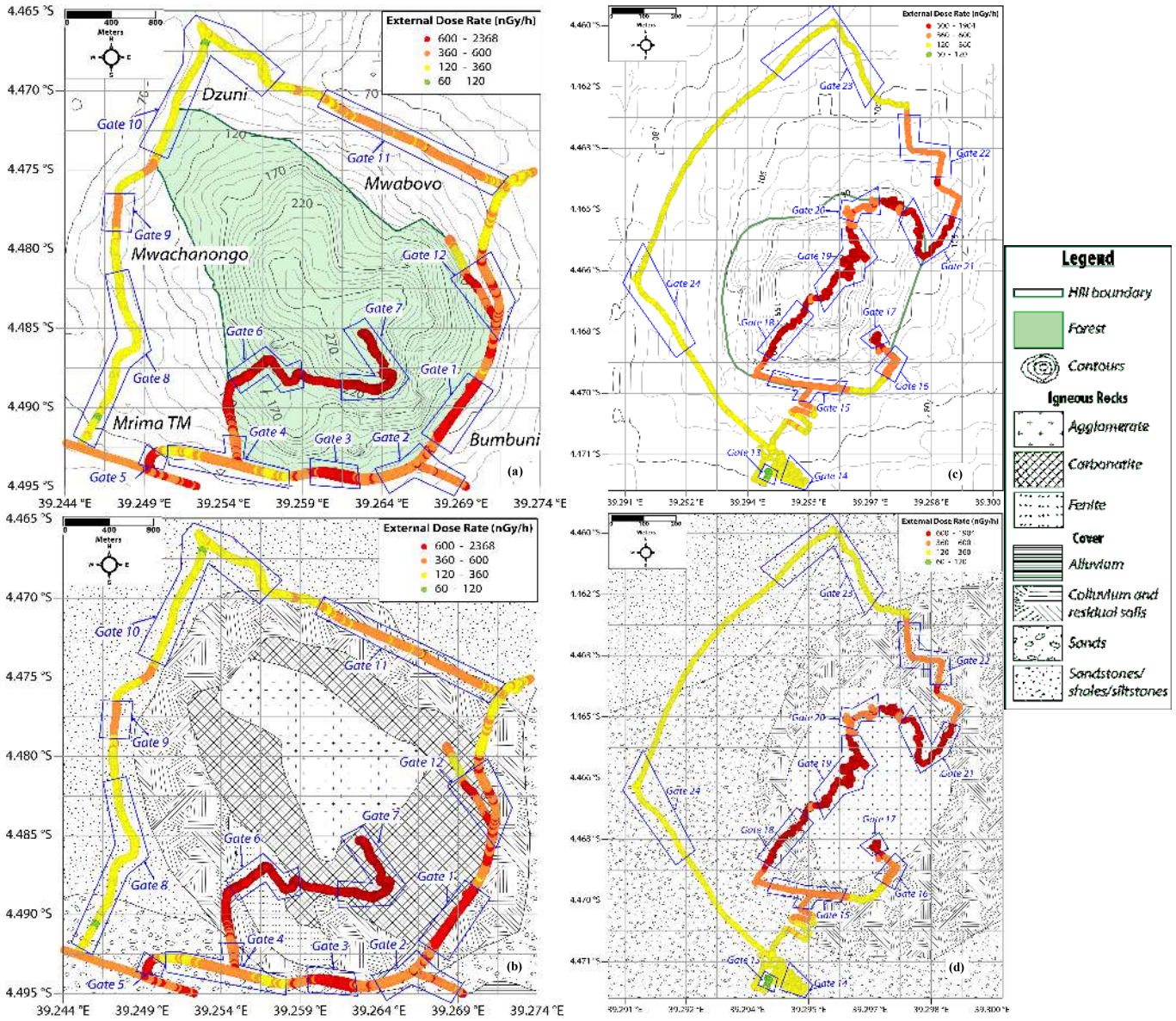

Fig. 5.7: Gamma dose-rate mapping for the Mrima and Kiruku Hills overlaid on (a,c) topographical (contour heights are ASL) and (b,d) geological (adapted from: JICA (1993)) maps. *In-situ* $\gamma-$ray spectra were aggregated in gates 1 - 24.

5.1.3.2 Gamma dose-rates around Mrima Hill

Gamma dose-rates measured on a ploughed field separated from the southern base of Mrima Hill by a murram road ranged 780 - 1261 nGy h^{-1}, as shown in Fig. 5.8 (a). These rates were almost ten times higher than in Bumbuni village, 2 km away to the south east. The site was ploughed and generally sloped, surrounded by maize plantations on the bordering fields, which explains the dose-rate variations. The highest dose-rates were measured along the murram road and further south at the ploughed field boundary. In an open field site in Bumbuni village, 1 km away to the south west of the Mrima foothills site, measured dose-rates ranged 44 - 512 nGy h^{-1}. The higher dose-rates ($>$ 360 nGy h^{-1}) were confined along the foot path, as shown in Fig. 5.8 (b). The variation observed in measured dose-rates (gates 7 - 9) could be attributed to attenuation of γ-rays from the soil by vegetation.

At an open field site located near the Mwabovo junction, located approximately 1.5 km away to the north east of the Mrima foothills site, there were minimal variations in measured dose-rates (ranged 105 - 120 nGy h^{-1}), as shown in Fig. 5.9 (a). Similarly at a farm site in Mamba, north of Mrima Hill approximately 4 km from Mwabovo junction, measured dose-rates (ranged 106 - 186 nGy h^{-1}) were also relatively uniform, as shown in Fig. 5.9 (b). At the Menzamwenye junction, high dose-rates ($>$ 300 nGy h^{-1}) were measured along the paved road, as shown in Fig. 5.9 (c), while dose-rates measured in the roadsides, approximately 50 m away from the paved road were $<$ 60 nGy h^{-1}. However, on a small section of the swamp near the road tunnel, measured dose-rates (ranged: 61 - 412 nGy h^{-1}) were up to 5 times higher than the values measured in the roadsides. At the Marenji field, located approximately 4.5 km away to the south west of the Mrima foothills site, measured dose-rates in the ploughed fields were generally $<$ 60 nGy h^{-1} with a slight increment noted along the footpaths (ranged 62 - 80 nGy h^{-1}), as shown in Fig. 5.9 (d).

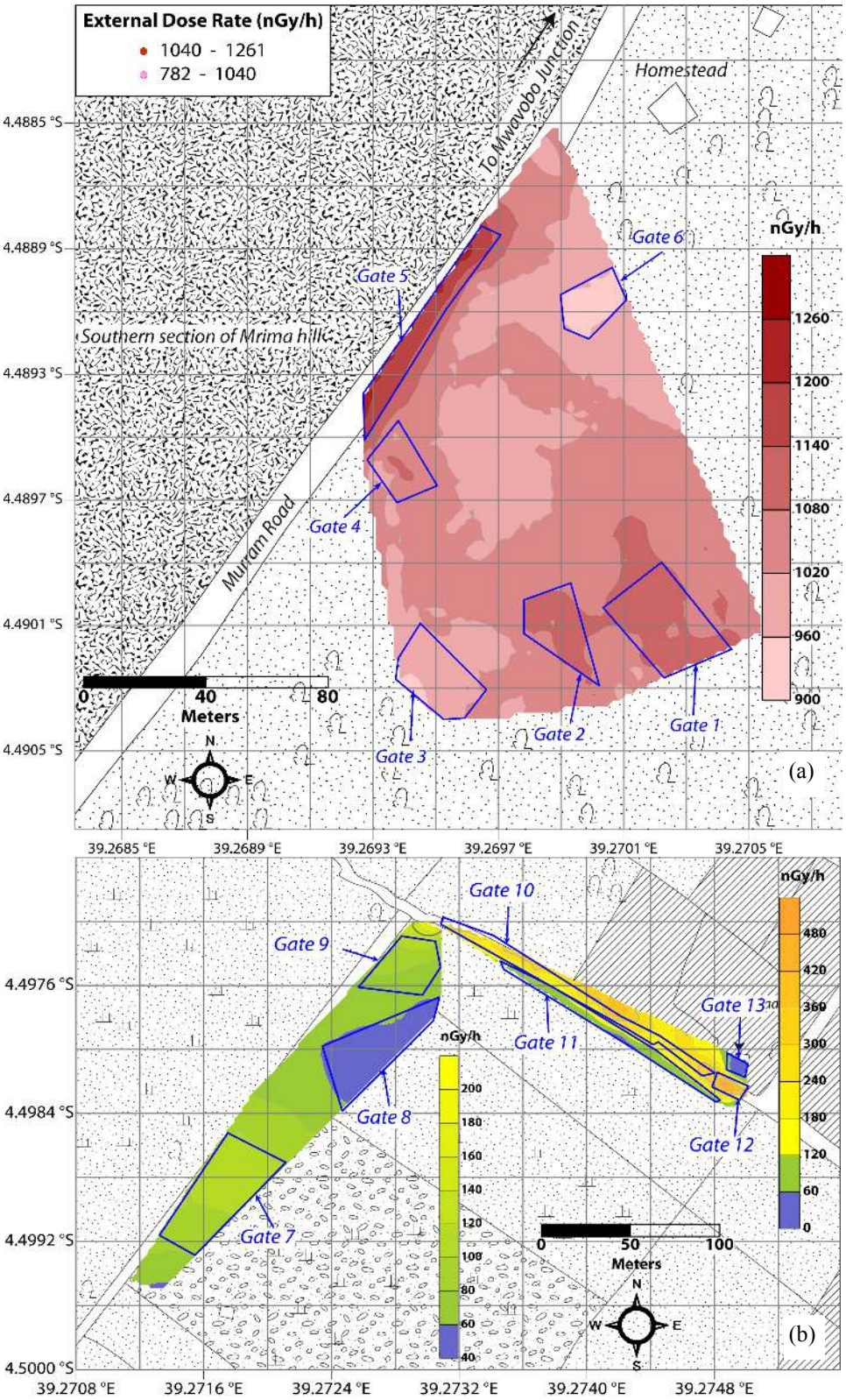

Fig. 5.8: Dose-rate interpolation by Kriging technique for (a) Mrima southern foothills ploughed field and (b) Bumbuni open field. *In-situ* $\gamma-$ray spectra were aggregated in gates 1 - 13.

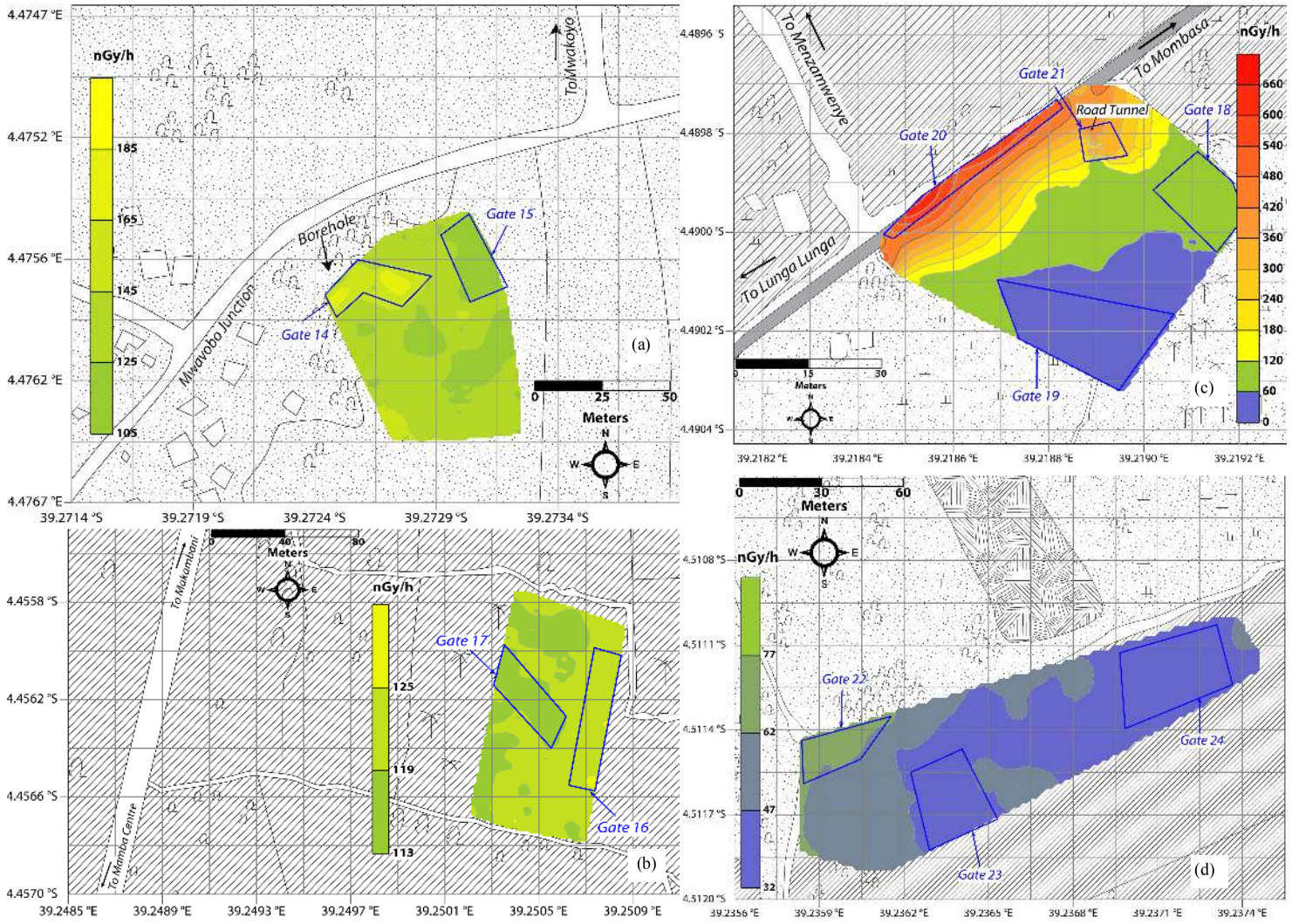

Fig. 5.9: Dose rate interpolation by Kriging technique for (a) Mwabovo open field (b) Mamba farm (c) Menzamwenye roadside and (d) Marenji farm. *In-situ* $\gamma-$ray spectra were aggregated in gates 14 - 24.

5.2 Results of radioactivity measurements and the associated radiological risk factors

This section presents results of the radioactivity measurements (^{40}K, ^{238}U and ^{232}Th) and associated radiological risk factors ($AEDE$, H_{ex} and $ECLR$) in the study area. These were determined by aggregating and processing the *in-situ* $\gamma-$ray spectra measured in the $\gamma-$ray spectral sampling gates indicated on gamma dose-rate maps presented in Sub-section 5.1.2 and 5.1.3. The results were further examined in relation to world average values for soil, and compared with those from related studies in the region as well as other HBRA in Kenya and elsewhere.

5.2.1 Statistical summaries for radioactivity measurements

The measured (*in-situ*) radioactivity concentrations were explored by adding up and processing spectra taken at 1 s intervals in areas defined by γ-ray spectral sampling gates, as illustrated in Fig. 5.10 (a) - (c). The criteria used for selecting these areas was guided by dose-rate variations observed in the gamma dose-rate maps. In principle, longer stationary measurements could have been made but that would not have increased the representativeness of the areas that were being surveyed as radioactivity anomalies were present, hence a geospatial gating approach was chosen to better represent the areas and provide sufficient statistics.

However, the measurements were found to be generally non-symmetric and multi-modal and showed neither normal nor log-normal probability distributions due to their spatial nature and presence of outliers, as illustrated in Fig. 5.10 (d) - (f). Consequently, the median and median absolute deviation (MAD) which are statistically non-parametric and robust for skewed distributions (Reimann and Filzmoser, 2000) were used to perform summary descriptive statistical analyses of the measurements. The resulting median and MAD values were further aggregated using mean and standard deviation (SD) and tabulated as the representative values for the surveyed areas.

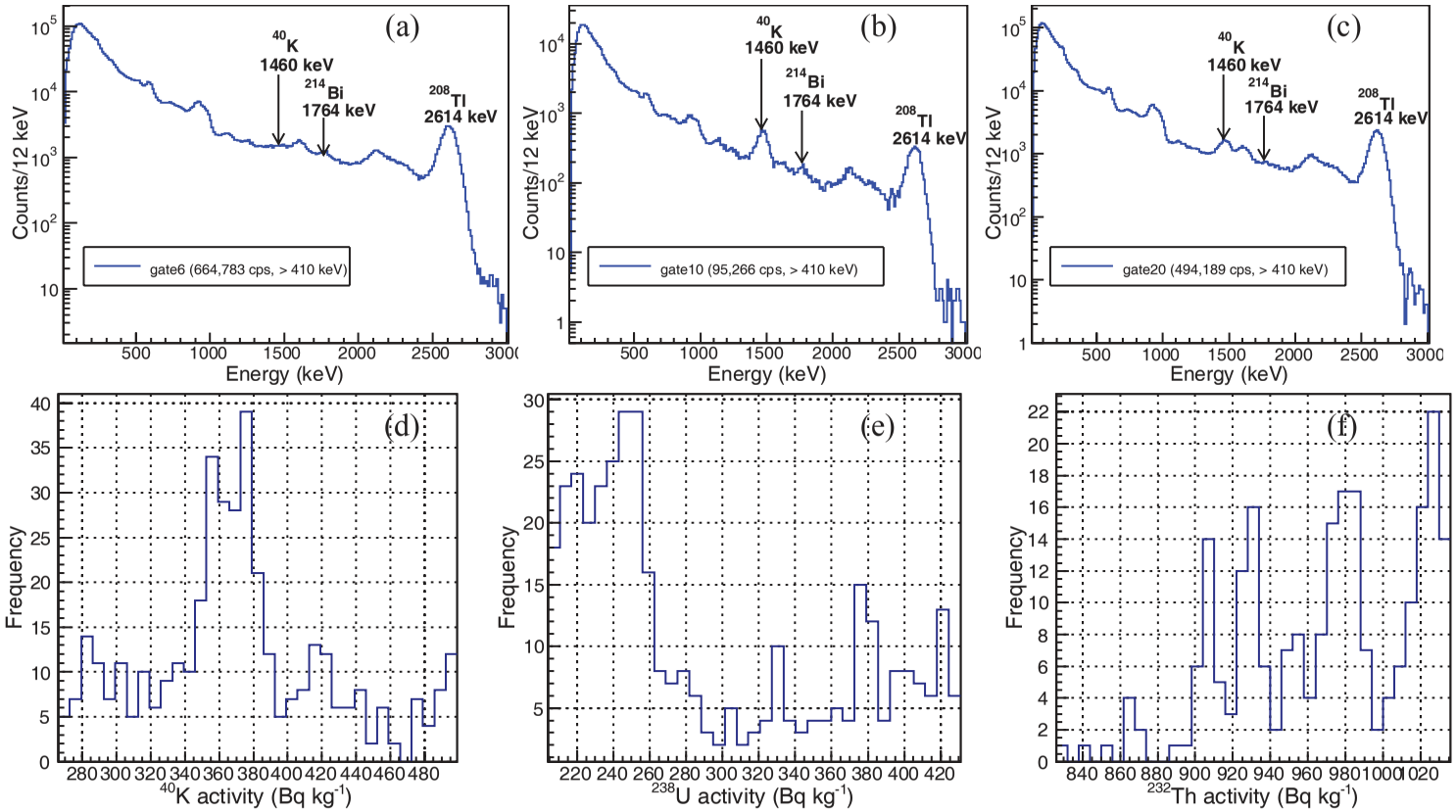

Fig. 5.10: *In-situ* $\gamma-$ray spectra (aggregated for 200 s) showing variation of ^{40}K, ^{232}Th and ^{238}U counts and total cps in (a) gate 6, (b) gate 10 and (c) gate 20 of the Mrima and Kiruku Hills (see Fig. 5.7). Frequency histogram plots illustrating non-symmetric distribution of the activity concentrations of ^{40}K, ^{232}Th and ^{238}U are shown in (d) gate 10, (e) gate 6 and (f) gate 20.

5.2.2 Activity concentrations of ^{40}K, ^{238}U and ^{232}Th in the south coast road environs and Indian Ocean coastline

Measured activity concentrations of ^{40}K, ^{238}U and ^{232}Th in the south coast paved road adjoining environs were generally low, ranging $<$ 202 Bq kg^{-1}, $<$ 45 - 73±4 Bq kg^{-1} and 35±8 - 96±39 Bq kg^{-1}, respectively. Radioactivity levels along the Indian ocean beaches in Bodo and Munje, and at a sand quarry in Ramisi were much lower, as measured activity concentrations of ^{40}K, ^{238}U and ^{232}Th were below the MDA of the PGIS-21 detector. A summary of the results is given in Table 5.4. The high MAD values associated with Ramisi measurements can be attributed to variability of ^{238}U and ^{232}Th in the area. The Th/K and U/K ratios are low and relatively constant compared to Th/U ratios. It may also be observed that Bodo and Ramisi are distinguished by higher Th/U ratios ($>$ 1) which suggests higher leachability of U compared to the other areas.

Table 5.4: Summary statistics for gamma dose-rates, activity concentrations of ^{40}K, ^{238}U and ^{232}Th and activity ratios measured in the south coast paved road environs

	Dose-rate	Activity (Bq kg^{-1})			Activity ratios		
Location (gate)	(nGy h^{-1})	^{40}K	^{238}U	^{232}Th	Th/K	Th/U	U/K
Kidzumbani (1)†	53±2	$<$ 202	65±4	49±4	0.2	0.7	0.3
Munje (2)†	41±2	$<$ 202	47±5	35±2	0.1	0.7	0.2
Shirazi (3)†	57±2	$<$ 202	73±4	45±2	0.2	0.5	0.3
Ramisi (4)†	74±26	$<$ 202	58±22	96±39	0.3	1.4	0.2
Bodo (5)†	53±2	$<$ 202	$<$ 45	63±4	0.2	1.4	0.2
Pongwe/Kidimu (6)†	39±5	$<$ 202	$<$ 45	35±8	0.4	0.8	0.5
Bodo beach‡	28±2	$<$ 470	$<$ 112	$<$ 64	0.4	1.3	0.3
Munje beach‡	16±5	$<$ 470	$<$ 112	$<$ 64	0.1	0.4	0.3
Ramisi sand quarry‡	16±1	$<$ 470	$<$ 112	$<$ 64	0.6	0.9	0.6

†PGIS-128 spectrometry vehicular measurements; γ-ray spectral sampling gates are indicated in Fig. 5.2

‡PGIS-21 spectrometry ground-based measurements hence higher MDA (see Table 4.3)

5.2.3 Activity concentrations of ^{40}K, ^{238}U and ^{232}Th in the south coast paved road, side road intersections and roadsides

The activity concentrations of ^{40}K, ^{238}U and ^{232}Th measured in the south coast paved road, side-road intersections and roadsides, are presented in Table 5.5 (a) - (e). From the results, it was found that the HBR anomaly noted along the paved road in Gazi is due to elevated activity concentrations of ^{238}U and ^{232}Th, see Table 5.5 (a) and spectra shown in Fig. 5.11. Furthermore, higher Th/K and U/K ratios were also observed in gate 2 and 3 compared to gate 1, while the Th/U ratios had minimal variation, implying that the road paving material contained elevated levels of both ^{238}U and ^{232}Th and had been relocated elsewhere.

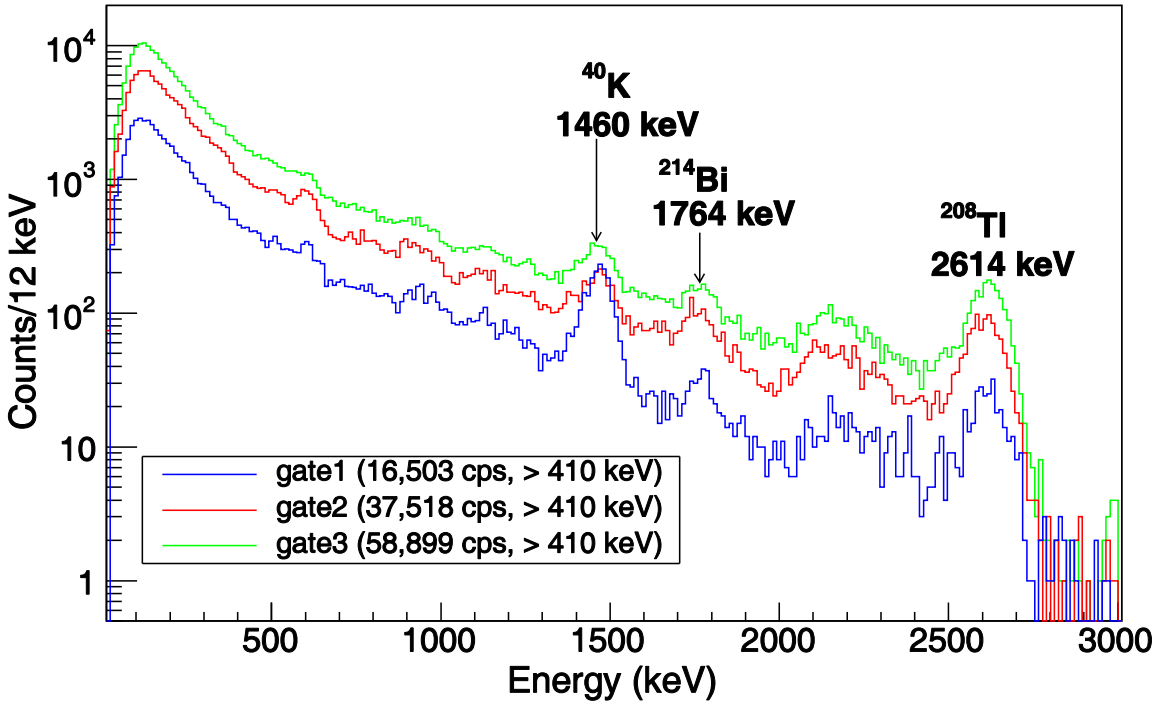

Fig. 5.11: *In-situ* $\gamma-$ray spectra (aggregated for 100 s) showing variation of ^{40}K, ^{232}Th and ^{238}U counts and total cps along the south coast paved road in Gazi.

At the Ramisi Islamic center roadside, activity concentrations of ^{238}U and ^{232}Th were also found to be enhanced along the paved road (gate 4 and 6) compared to the roadside (gate 5), see Table 5.5 (b). Whereas the Th/U ratios are relatively uniform, the Th/K

and U/K ratios were found to be higher in the paved road by more than 6 and 3.5 times, respectively compared to the roadside. Activity concentrations of ^{40}K at the Bwiti junction were found to be generally below the MDA ($<$ 202 Bq kg^{-1}) while ^{238}U and ^{232}Th levels in the side road intersection (gate 7) were found to be 15 - 22 and 8 - 14 times, respectively higher than in the roadside (gate 8), and more than 3 times compared to the main road (gate 9), see Table 5.5 (c). The paved road section is slightly elevated compared to adjacent land; therefore there is possibility of radiogenic contamination in the roadside when radionuclides are dispersed from the murram roadbeds by weathering, precipitation or human activity. The depletion of ^{40}K is possibly due to leaching of K-bearing minerals from the abraded road surfaces. U/K compared to Th/K ratios are higher probably due to the solubility of uranium under oxidizing conditions, making it more mobile (Wilford *et al.*, 1997).

Similarly, the ^{238}U and ^{232}Th levels at other side road intersections in Mwangwei junction (gate 10 - 11) and Mrima TM junction (gate 13 - 14) were found to be particularly high (activity concentrations of ^{238}U and ^{232}Th ranged 532$\pm$14 - 1167$\pm$20 Bq kg^{-1} and 657$\pm$151 - 1579$\pm$16 Bq kg^{-1}, respectively) compared to the main road and roadsides. These enhanced levels are likely to correspond to resistate radioactive minerals present in the murram roadbeds such as monazite and pychlore. The Th/K and U/K ratios are equally high (ranged 2.4 - 8.0 and 1.9 - 9.3, respectively), also implying that the murram on the roadbeds had been ferried from elsewhere. It may also be observed that the Ramisi Islamic center and Mrima TM sites are distinguished by higher Th/U ratios ($>$ 1.5) which suggests higher leachability of U compared to the other areas.

Table 5.5: Summary statistics for gamma dose-rates, activity concentrations of ^{40}K, ^{238}U and ^{232}Th and activity ratios measured in the south coast paved road, side road intersections and roadsides

	Dose-rate	Activity (Bq kg^{-1})			Activity ratios		
Gate	(nGy h^{-1})	^{40}K	^{238}U	^{232}Th	Th/K	Th/U	U/K
		(a) Gazi paved road					
1	65±2	358±13	57±4	49±2	0.1	0.9	0.2
2	125±3	< 202‡	167±11	124±4	1.2	0.7	1.7
3	283±7	343±34	308±13	315±10	0.9	1.0	0.9
		(b) Ramisi Islamic center roadside					
4	274±119	287±85	202±102	340±130	1.2	1.7	0.7
5	52±7	227±56	< 45†	53±6	0.2	1.5	0.2
6	275±91	271±28	218±88	317±100	1.2	1.5	0.8
		(c) Bwiti junction roadside					
7	809±154	< 202‡	992±209	775±131	7.0	0.8	8.9
8	82±43	< 202‡	65±42	92±49	0.7	1.4	0.5
9	369±44	207±50	408±32	374±54	1.8	0.9	2.0
		(d) Mwangwei junction side-road intersection					
10	896±3	< 202‡	1167±20	997±10	8.0	0.9	9.3
11	499±94	273±24	532±14	657±151	2.4	1.2	1.9
12	125±5	266±3	95±5	159±6	0.3	1.5	0.2
		(e) Mrima TM junction side-road intersection					
13	1078±7	393±26	901±22	1567±16	4.0	1.7	2.3
14	1085±3	404±34	904±29	1579±16	3.9	1.7	2.2
15	788±34	361±14	625±18	1123±94	1.6	1.6	1.0

‡MDA of ^{40}K (202 Bq kg^{-1}) by PGIS-128 spectrometer

†MDA of ^{238}U (45 Bq kg^{-1}) by PGIS-128 spectrometer

5.2.4 Activity concentrations of ^{40}K, ^{238}U and ^{232}Th in the Mrima and Kiruku Hills

The activity concentrations of ^{40}K, ^{238}U and ^{232}Th measured in the Mrima and Kiruku Hills are presented in Table 5.6 and profile plot shown in Fig. 5.12. It was found that the levels of ^{40}K are highest in flat terrains located at the western and eastern base of Mrima Hill (gate 8 - 10 and 12), ranging 394±32 - 530±12 Bq kg^{-1}, and lowest (< 385±51 Bq kg^{-1}) along the sloppy terrains (gate 1 - 7 and 11). This indicates washout of K-bearing and other soluble minerals along the sloped terrains possibly due to weathering and leaching, and the deposition of transported sediments in the flat/depressed terrains located at the base of the hill. The levels of ^{238}U are highest along the hill slopes (gate 1, 4 - 6 and 11), ranging 348±41 - 582±54 Bq kg^{-1}, and lowest (< 166±4 Bq kg^{-1}) in the flat terrains (gate 8 - 10). The levels of ^{232}Th are highest at the southern foothills and hill crest associated with carbonatite rocks, colluvium and residual soils (gate 1, 6 and 7), ranging 2069±326 - 2837±85 Bq kg^{-1} and lowest (< 618±22 Bq kg^{-1}) at the hill base areas mainly associated with sands and sandstones/shales/siltstones (gate 8 - 11). The distribution of ^{232}Th and ^{238}U levels was also found to be uniform (Fig. 5.12) with some slight variations in gate 5 and 12, where ^{232}Th levels decrease as ^{238}U levels increase and vice versa. These variations could be attributed to anthropogenic effects such as road paving (gate 5) and land ploughing (gate 12).

Although the levels of ^{232}Th in Kiruku Hill are mostly in the same range as Mrima Hill, it was found that the levels of ^{40}K and ^{238}U are generally higher and lower, respectively compared to Mrima Hill (Fig. 5.12). A general increment in the levels of ^{232}Th (606±16 - 2240±367 Bq kg^{-1}) was observed in areas mainly associated with agglomerate rocks, colluvium and residual soils which are the southern hill slopes, hill crest and northern hill slopes (gate 15 - 22). The levels of ^{40}K are highest in the southern (gate 15 - 18) and northern (gate 20) hill slopes, ranging 686±48 - 1166±82 Bq kg^{-1}, while the levels of ^{238}U are highest in the northern foothills (gate 20 - 22), ranging 96±15 - 151±12 Bq kg^{-1}. The southern and northern foothills which are mainly associated with sands and

sandstones/shales/siltstones (gate 13, 14, 23 and 24) had the lowest levels of ^{40}K, ^{238}U and ^{232}Th (Fig. 5.12).

Table 5.6: Summary statistics for gamma dose-rates, activity concentrations of ^{40}K, ^{238}U and ^{232}Th and activity ratios measured in the Mrima and Kiruku Hills

		Dose-rate	Activity (Bq kg^{-1})			Activity ratios		
Location	Gate	(nGy h^{-1})	^{40}K	^{238}U	^{232}Th	Th/K	Th/U	U/K
Mrima Hill	1	1106±159	313±56	364±27	2069±326	6.6	5.7	1.2
	2	711±89	308±54	296±56	1300±140	4.2	4.4	1.0
	3	648±57	303±32	296±16	1156±130	3.8	3.9	1.0
	4	631±45	355±33	348±41	1028±79	2.9	3.0	1.0
	5	692±99	385±51	582±54	955±118	2.5	1.7	1.5
	6	1357±39	339±24	455±61	2591±61	7.7	5.7	1.4
	7	1421±48	331±45	289±25	2837±85	8.6	9.8	0.9
	8	195±10	428±13	106±16	272±69	0.6	2.6	0.3
	9	375±19	530±12	166±4	618±22	1.2	3.7	0.3
	10	185±22	394±32	81±14	244±37	0.6	3.0	0.2
	11	434±84	287±29	462±65	543±124	1.9	1.2	1.6
	12	674±96	465±70	244±16	1238±214	2.7	5.1	0.5
Kiruku Hill	13	168±35	327±32	60±4	242±61	0.8	4.1	0.2
	14	276±11	366±20	68±8	430±29	1.2	6.3	0.2
	15	403±11	1166±82	79±10	606±16	0.5	7.7	0.1
	16	476±62	897±38	73±7	773±128	0.9	10.6	0.1
	17	700±30	935±24	70±9	1181±45	1.3	16.9	0.1
	18	858±15	686±48	47±10	1520±36	2.2	32.3	0.1
	19	813±36	251±166	< 45	1459±74	5.8	44.2	0.1
	20	589±28	710±27	96±15	976±43	1.4	10.2	0.1
	21	1268±181	399±48	151±12	2240±367	5.6	14.9	0.4
	22	488±45	531±36	118±14	799±79	1.5	6.8	0.2
	23	270±62	490±36	76±5	412±114	0.8	5.4	0.2
	24	207±22	343±66	74±6	304±48	0.9	4.1	0.2

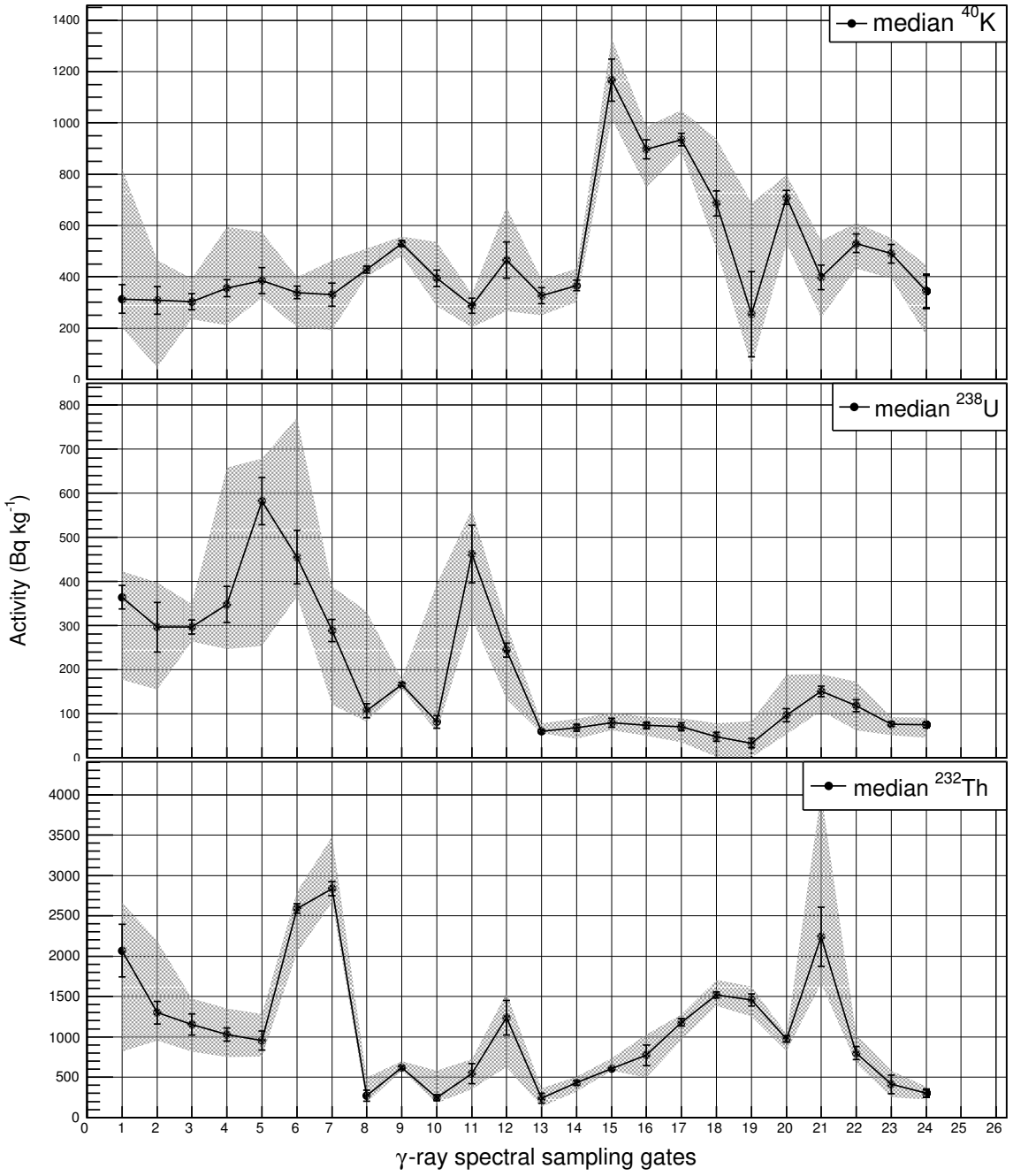

Fig. 5.12: Profile plot showing natural radionuclide concentrations in selected sites of Mrima (gates 1 - 12) and Kiruku (gates 13 - 24) Hills. The median and MAD values in the γ-ray spectral sampling gates are shown together with the range of activity concentration values (shaded). Lines have no significance, they are used for visual guidance.

High Th/U ratios (> 7) were observed mostly in Kiruku Hill (see Table 5.6) which is indication of the oxidation and intense leaching of U during weathering (see also elemental concentration profile of soil samples analyzed in Table 5.16, Section 5.4). Intermediate Th/U ratios (2 - 7) observed along the hill slopes and foothills of both Mrima and Kiruku Hills indicate incomplete weathering and leached U, or mixture of weathered sediments (Adams and Weaver, 1958) from the hill summits and hill slope soils. Low Th/U ratios (< 2) observed in the Mrima Hill foothills indicate deposition of U from the hill summit and the foothills. High Th/K ratios (> 2) along the hill slopes of both Mrima and Kiruku Hills indicate depletion of K-bearing minerals. It may be noted that K and U are geochemically mobile in oxidized environments (Chan *et al.*, 2007).

5.2.5 Activity concentrations of ^{40}K, ^{238}U and ^{232}Th around Mrima Hill

The activity concentrations of ^{40}K, ^{238}U and ^{232}Th measured in the areas surrounding the Mrima Hill are presented in Table 5.7 (a) - (e). It was found that the elevated gamma dose-rates measured in the southern foothills of Mrima Hill (Table 5.7 (a)) correspond to elevated activity concentrations of ^{232}Th which ranged 1805±56 - 2330±24 Bq kg^{-1}. The levels of ^{238}U range 118±18 - 223±43 Bq kg^{-1} while levels of ^{40}K are generally below the MDA. These indicates the intense weathering of soil in the foothills of Mrima Hill as reported by Baker (1953) which results in the loss of soluble mineral constituents bearing ^{40}K and ^{238}U, and enhancement of ^{232}Th in resistate radioactive minerals such as monazite. This is also manifested in the high Th/K and Th/U ratios (> 10) observed (see Table 5.7 (a)). It was further noted that the levels of ^{232}Th and ^{238}U are slightly higher on the murram road (gate 5) compared to the adjacent field, which could be as a result depletion of topsoil from erosion exposing the resisted minerals on the road surface. The levels of ^{232}Th are also slightly enhanced in gate 1, 2 and 4 compared to gate 3 and gate 6 indicating bare soil exposure, as loose particles have a higher surface area per mass ratio and vegetation which attenuates γ-rays (Laedermann *et al.*, 1998).

Table 5.7: Summary statistics for gamma dose-rates, activity concentrations of ^{40}K, ^{238}U and ^{232}Th and activity ratios measured around the Mrima Hill

	Dose-rate	Activity (Bq kg^{-1})			Activity ratios		
Gate	(nGy h^{-1})	^{40}K	^{238}U	^{232}Th	Th/K	Th/U	U/K
	(a) Bumbuni Mrima foothills (homestead site)						
1	1173±10	< 202	118±18	2103±32	15.4	17.8	0.9
2	1175±19	< 202	127±24	2096±46	28.3	16.5	1.7
3	1071±25	< 202	154±18	1877±53	22.8	12.2	1.9
4	1174±22	202±49	163±25	2053±29	10.2	12.6	0.8
5	1331±11	< 202	223±43	2330±24	25.5	10.5	2.4
6	1026±30	< 202	155±14	1805±56	17.4	11.7	1.5
	(b) Bumbuni open field site						
7	109±8	< 202	47±4	154±16	0.8	3.3	0.3
8	53±5	< 202	< 45	69±10	0.6	2.3	0.3
9	90±22	< 202	< 45	135±30	1.5	3.8	0.4
10	328±32	< 202	183±21	450±48	4.3	2.5	1.8
11	72±9	< 202	< 45	101±17	0.8	3.4	0.3
12	575±19	< 202	545±21	682±24	10.4	1.3	8.3
13	55±7	< 202	< 45	62±6	0.4	1.7	0.2
	(c) Mwabovo open field site						
14	182±28	309±12	87±4	249±48	0.8	2.9	0.3
15	130±12	312±9	77±5	166±12	0.5	2.2	0.3
	(d) Mamba ploughed field site						
16	130±1	239±5	64±3	175±2	0.7	2.7	0.3
17	129±1	262±18	61±4	172±2	0.7	2.8	0.2
	(f) Menzamwenye roadside site						
18	166±82	< 202	143±65	185±98	0.9	1.3	0.7
19	47±3	< 202	< 45	46±4	0.3	1.3	0.2
20	661±53	661±53	479±55	830±64	1.9	1.7	1.1
21	372±36	372±36	154±16	533±90	2.7	3.5	0.8
	(e) Marenji ploughed field site						
22	77±3	289±15	64±6	72±3	0.3	1.1	0.2
23	46±1	< 202	< 45	49±1	0.4	1.3	0.4
24	38±2	< 202	< 45	40±3	0.5	1.1	0.4

At the Bumbuni open field site, activity concentrations of ^{232}Th and ^{238}U range 62±6 - 682±24 Bq kg^{-1} and < 45 - 545±21 Bq kg^{-1}, respectively while levels of ^{40}K are below the MDA, see Table 5.7 (b). The area located next to a stream drainage channel (gate 12) is delineated by a higher ^{238}U response, as shown in Fig. 5.13, which could be associated with radium isotopes deposited from the ground water or U precipitation. Along the footpath (gate 10), levels of ^{232}Th are enhanced compared to adjacent field which was covered by vegetation (gate 7 - 9, 11), which indicates the leaching of soluble minerals on the loose surface; see also depletion of K and enhancement of LREEs and Th, exhibited on the footpath soil compared to open field and homestead soil samples in Table 5.16, Section 5.4.

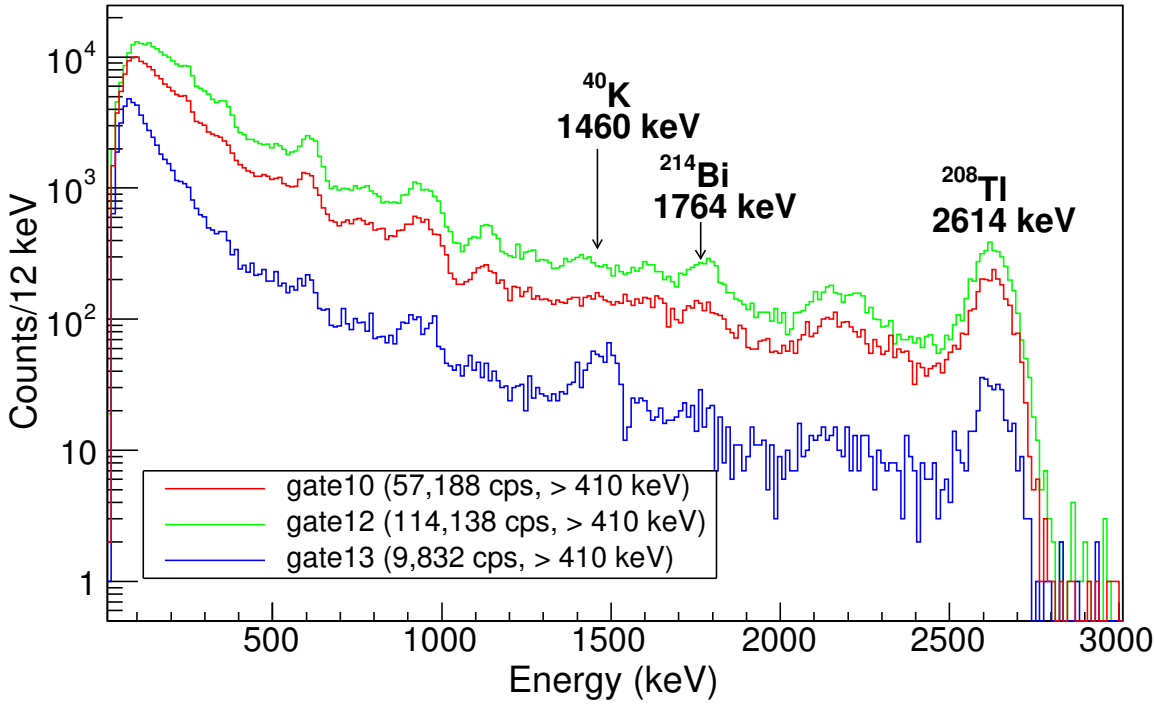

Fig. 5.13: *In-situ* $\gamma-$ray spectra (aggregated for 43 s) showing variation of ^{40}K, ^{232}Th and ^{238}U counts and total cps along the weathered footpath (gate 10), stream drainage channel (gate 12) and ploughed land (gate 13) at the Bumbuni open field site.

At the Mwabovo junction open field and Mamba ploughed sites, lower levels of ^{238}U and ^{232}Th (61±4 - 87±4 Bq kg^{-1}and 166±12 - 249±48 Bq kg^{-1}, respectively) and higher levels of ^{40}K (239±12 - 312±9 Bq kg^{-1}) were measured, compared to those of the Mrima

foothills and Bumbuni open field sites. At the Menzamwenye junction, the levels of ^{40}K, ^{238}U and ^{232}Th along the paved road (gate 20) were more than 14, 2 and 18 times respectively, higher than on the roadside, approximately 50 m away (gate 19); this is consistent with observations made earlier in Sub-section 5.2.3. At the road tunnel (gate 21), the levels of ^{232}Th and ^{238}U were found to be relatively enhanced compared to the neighbouring areas (gate 18 and 19), which indicates deposition of contaminated soils from the paved road shoulders. It was observed that the levels of ^{40}K, ^{238}U and ^{232}Th at the Marenji ploughed site are much lower compared to all the other surveyed sites; the lower Th/U ratios are indicative of the comparatively lower ^{232}Th levels. See summary of the results in Table 5.7 (c) - (f).

5.2.6 Discussion on radioactivity measurements and associated radiological risk factors

5.2.6.1 The south coast paved road and adjoining environs

Descriptive statistics for the activity concentration values and radiological risk factors in the south coast paved road and adjoining environs are presented in Table 5.8. It may be observed that the means of ^{40}K are below the world average value for soil (< 420 Bq kg^{-1}), while those of ^{238}U and ^{232}Th along the main road and side road intersections are more than 9 - 27 and 7 - 24 times the world average values for soil (33 and 45 Bq kg^{-1}, respectively). The levels of ^{238}U and ^{232}Th in the roadsides and areas located further away from the roadsides are more than 2 times and within the range of world average values for soil, respectively. These results show that there is significant contamination of ^{238}U in the roadsides which could be due to precipitation or abrasion of the murram roadbed by weathering or human activity.

The AEDE values in the paved road and side-road intersection range 0.75±0.05 - 2.19±0.05 mSv; these are higher compared to the world population weighted average value and the maximum permissible dose of 1 mSv/y recommended for members of the public (ICRP, 2007) by a factor of 10 - 29 and 0.75 - 2.19, respectively. It should however be noted that AEDE values reported are based on an outdoor occupancy factor of 0.4 (Mustapha, 1999), while the world average and ICRP dose limit were based on an outdoor occupancy factor of 0.2. The external radiation hazard index values due to NORM in both the south coast paved road and side road intersections are > 1, making them significant; while the mean ELCR estimated values are higher than the world average value (0.28×10^{-3}) by more than 10 - 30 times. Correlation analysis of the radioactivity concentrations and absorbed gamma dose-rates in air (Fig. 5.14) showed that the HBR anomaly along the south coast paved road and side-road intersections is due to elevated ^{238}U and ^{232}Th levels associated with the murram roadbeds.

Table 5.8: Descriptive statistics of measured activity concentrations of ^{40}K, ^{238}U and ^{232}Th, gamma dose-rates and radiological risk factors for the south coast paved road and adjoining environments

	^{40}K (Bq kg^{-1})				^{238}U (Bq kg^{-1})				^{232}Th (Bq kg^{-1})				Dose-rate (nGy h^{-1})				AEDE (mSv)				H_{ex}				ECLR $\times 10^{-3}$			
Parameter	A	B	C	D	A	B	C	D	A	B	C	D	A	B	C	D	A	B	C	D	A	B	C	D	A	B	C	D
Mean	269	281	< 202	< 202	308	900	93	54	345	1116	98	54	307	892	97	53	0.752	2.189	0.238	0.130	2.22	6.80	0.66	0.38	2.9	8.4	0.9	0.50
SD	21	17	14	9	21	20	16	7	23	26	15	8	21	21	15	6	0.052	0.052	0.037	0.015	0.15	0.16	0.10	0.05	0.2	0.2	0.1	0.06
Min	123	111	50	50	132	532	18	39	94	657	23	35	109	499	25	39	0.267	1.223	0.061	0.097	0.74	4.00	0.15	0.25	1.0	4.7	0.2	0.37
Max	567	404	286	160	650	1452	318	73	802	1579	333	96	620	1278	315	74	1.522	3.135	0.773	0.181	4.97	10.11	2.20	0.60	5.9	12.1	3.0	0.70
Range	444	293	237	109	519	920	300	34	708	922	310	61	511	779	290	34	1.255	1.911	0.711	0.084	4.23	6.11	2.06	0.35	4.8	7.4	2.7	0.32
World average for soil[†]																												
	420				33				45				60				0.074				0.35				0.28			

[A]South coast paved road including 2 m extension from both sides of bitumen pavement

[B]Side road intersections (murram and paved) and bus stops

[C]Roadside ($\gtrapprox$ 15 m $\lessapprox$ 100 m away from main paved road)

[D]South coast paved road environs ($\gtrapprox$ 200 m away from main paved road)

[†]Adapted from UNSCEAR (2000)

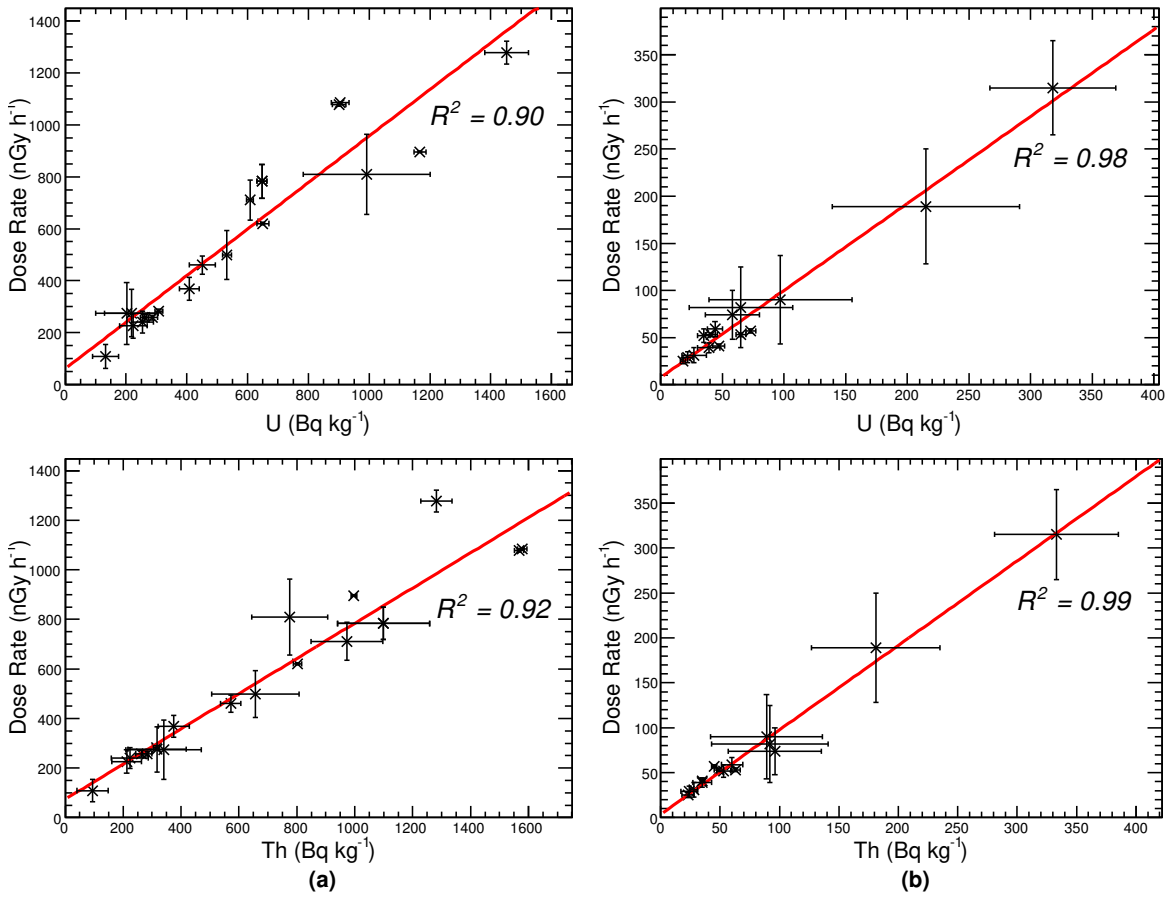

Fig. 5.14: Correlation of activity concentrations of ^{238}U and ^{232}Th with absorbed gamma dose-rates measured in air (a) along the south coast paved and side road intersections and (b) roadsides and adjoining environs.

It may be concluded that contaminated murram roadbeds on the side-road intersections pose a significant radiological hazard to inhabitants and merchants operating businesses (a major occupational activity in the area) in close proximity. A major concern is the possibility of inhalation of radioactive dust particles abraded from the murram roadbeds, and contamination of boreholes located near the paved roads such as is the case at Bwiti junction. There is however a less hazard to road users due the restricted time spent on the road and partial radiation shielding provided by vehicles.

5.2.6.2 The Mrima-Kiruku complex

Descriptive statistics for the activity concentration values and radiological risk factors in the Mrima-Kiruku complex are summarized in Table 5.9. It may be observed that activity concentrations of ^{232}Th in the Mrima-Kiruku complex are generally higher than those of ^{40}K and ^{238}U. The mean activity concentration of ^{40}K is higher in Kiruku compared to Mrima by a factor of 1.5, while means of ^{232}Th and ^{238}U are higher in Mrima compared to Kiruku by a factor of 3.1 and 1.4, respectively. Furthermore, the means of ^{238}U and ^{232}Th and absorbed gamma dose-rates in the complex were found to be more than 2 - 9, 8 - 40, and 4 - 16 times the world average values for soil, respectively. It was further noted that the absorbed gamma dose-rates in air reduce significantly, i.e. by a factor of approximately 1.3 - 2.8 away from both Mrima and Kiruku Hill summits implying that the Mrima-Kiruku complex is a geogenic HBR anomaly.

Correlation analysis between the activity concentrations of ^{40}K, ^{238}U and ^{232}Th and air absorbed gamma dose-rates indicated that the HBR anomaly in both the Mrima and Kiruku Hills is mainly due to elevated activity concentrations of ^{232}Th, as shown in Fig. 5.15. Activity concentrations of ^{238}U were also found to have significant correlation ($R^2 = 0.80$) with air absorbed gamma dose-rates in the Mrima Hill environs. The AEDE values in the Mrima-Kiruku complex range 0.86±0.05 - 2.37±0.09 mSv; these are higher compared to the world average value and maximum permissible dose of 1 mSv/y recommended for members of the public by a factor of 11 - 32 and 0.86 - 2.37, respectively. In addition, the measured external radiation hazard index values due to NORM are > 1, making them significant. The mean ELCR estimated values range 3.3±0.2 - 9.1±0.3 $\times$ 10^{-3} and are up to 32 times higher by than the world average value. It may thus be concluded from an external dose perspective that there is significant (> 1 mSv/y) radiological hazard to inhabitants of the area particularly those who reside at the foothills of both Mrima and Kiruku Hills.

Table 5.9: Descriptive statistics for activity concentrations of ^{40}K, ^{238}U and ^{232}Th, absorbed gamma dose-rates in air and radiological risk factors in the Mrima-Kiruku complex

	^{40}K (Bq kg^{-1})					^{238}U (Bq kg^{-1})					^{232}Th (Bq kg^{-1})					Dose-rate (nGy h^{-1})					AEDE (mSv)					H_{ex}					ECLR $\times 10^{-3}$				
	A	B	C	D	E	A	B	C	D	E	A	B	C	D	E	A	B	C	D	E	A	B	C	D	E	A	B	C	D	E	A	B	C	D	E
Mean	381	235	334	603	460	326	205	288	73	104	1817	1168	446	1215	833	967	689	349	705	506	2.37	1.69	0.86	1.73	1.24	8.0	5.1	2.6	5.0	3.6	9.1	6.5	3.3	6.7	4.8
SD	28	19	18	28	22	24	15	24	14	11	51	26	28	38	33	36	19	21	27	24	0.09	0.05	0.05	0.07	0.06	0.3	0.2	0.2	0.2	0.2	0.3	0.2	0.2	0.3	0.2
Min	288	< 202	< 202	225	217	154	77	75	< 45	60	633	166	98	463	242	375	130	87	323	168	0.92	0.32	0.21	0.79	0.41	2.9	0.9	0.6	1.9	1.2	3.5	1.2	0.8	3.1	1.6
Max	533	584	671	1166	663	539	909	665	141	151	4247	2057	1037	1649	2240	2027	1161	628	918	1268	4.97	2.85	1.54	2.25	3.11	18.0	10.5	5.9	7.0	9.2	19.1	11.0	5.9	8.7	12.0
Range	244	557	552	942	446	385	832	590	116	91	3614	1891	939	1187	1998	1651	1031	541	596	1100	4.05	2.53	1.33	1.46	2.70	15.1	9.6	5.3	5.1	8.0	15.6	9.7	5.1	5.6	10.4
World average for soil[†]																																			
	420					33					45					60					0.074					0.35					0.28				

[A]Mrima Hill

[B]Mrima foothills (within 1.7 km from Mrima Hill)

[C]Mrima Hill environs ($\gtrapprox$ 1.7 km $\lessapprox$ 3.5 km away from Mrima Hill)

[D]Kiruku Hill

[E]Kiruku foothills

[†]Adapted from UNSCEAR (2000)

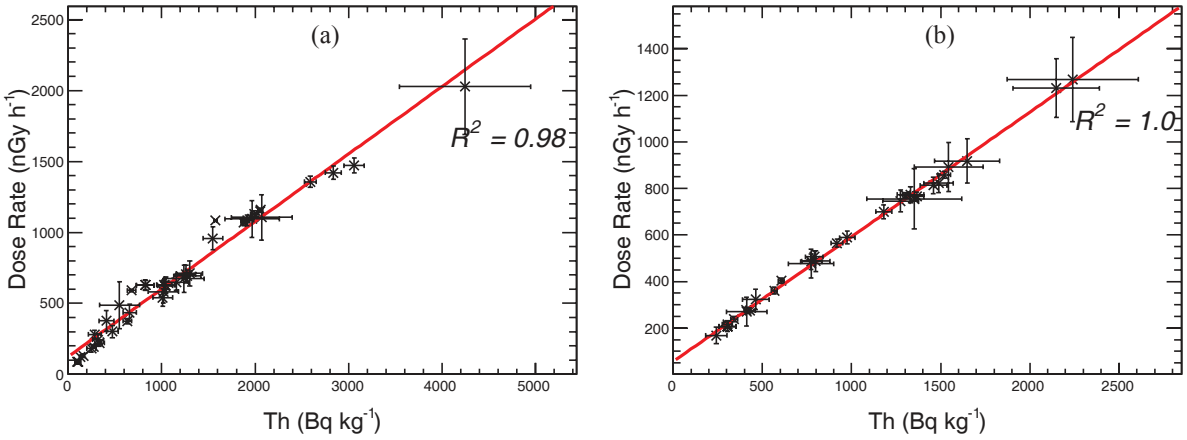

Fig. 5.15: Correlation of absorbed dose-rates in air with activity concentrations of ^{232}Th in (a) Mrima Hill (b) Kiruku Hills.

5.3 Comparison of gamma dose-rates and activity concentration values with other related studies

5.3.1 Comparison of results obtained from the south coast road environs with related studies

The results obtained from the south coast paved road environs (approximately, 1 - 20 km offshore) and along the Kenyan coast were compared with published values from related studies, see Table 5.10. Results from the present study were found to be comparable with those from previously published values. In both the present and previous studies, gamma dose-rates are below the world population weighted average ($<$ 60 nGy h^{-1}). This shows that the sediments underlying the south coastal region (see Fig. 5.2 (b)) have low radioactive mineral content. Furthermore, the low $\gamma-$ray response of ^{40}K, ^{238}U and ^{232}Th can be attributed to accumulation of quartz in sand (implied by high Si content in analysed soil samples, see Table 5.16 in Section 5.4).

The mean AEDE for the south coast road environs and Indian Ocean coastline were 0.114±0.035 mSv and 0.069±0.029 mSv, respectively; hence they are insignificant as

they are below the set annual public dose-limit of 1 mSv (ICRP, 2007). It may also be concluded from the dose-rate values that there is minimal influx of NORM to the Indian Ocean from the hinterland.

Table 5.10: Comparison of activity concentrations of ^{40}K, ^{232}Th and ^{238}U and absorbed gamma dose-rates in the south coast paved road environs with published values

	Activity (Bq kg^{-1})			Dose-rate	
Location	^{40}K	^{238}U	^{232}Th	(nGy h^{-1})	Reference
South coast road environs^{‡,1}	< 202	54±7	54±8	53±6	Present study
Kanana soils	137±13	31±2	35±3	41±3	Chege (2015)
Maumba soils	< 45	39±18	62±29	56±26	Maina (2008)†
	77±15	21±5	28±6	30±6	Osoro *et al.* (2011)
Nguluku soils	< 45	29±1	34±19	34±12	Maina (2008)†
	61±13	21±10	27±12	29±12	Osoro *et al.* (2011)
South coast beaches^{‡,2}	< 470	< 112	< 64	22±3	Present study
Gazi sediments (south coast)	206±26	12±1	11±1	21±2	Hashim *et al.* (2004)
World average for soils	420	33	45	60	UNSCEAR (2000)

^{‡,1}Average values for Kidzumbani, Munje, Shirazi, Ramisi, Bodo and Pongwe/Kidimu results from Table 5.4

^{‡,2}Average values for Munje and Bodo beaches results from Table 5.4

†Values reported are the median±MAD re-calculated from measured soil samples results in Maina (2008).

The results from the Indian Ocean coastline were further compared with similar studies carried out in different coastlines of the world, see Table 5.11. It was found that lower than the world population weighted average dose-rates were measured along the Indian Ocean coast in Kenya, Red Sea coast in North Africa and South west coast in Australia. This shows that the mineralogy of sands (and parent rocks) in these regions has low radioactive content. The higher than world population weighted average dose-rates reported in the other studies has been attributed to among other causes, geological setting and presence of heavy mineral deposits in beach sands for example monazite in the HBRA Brazilian beaches (Veiga *et al.*, 2006).

Table 5.11: Comparison of activity concentrations of ^{40}K, ^{232}Th and ^{238}U and absorbed gamma dose-rates along the Indian Ocean coastline with similar studies carried out in different parts of the world

	Activity (Bq kg^{-1})			Dose-rate	
Location	^{40}K	^{238}U	^{232}Th	(nGy h^{-1})	Reference
South coast beaches, Kenya	< 470	< 112	< 64	22±3	Present study
Red Sea coast, Egypt	758±2	23±2	14±2	51±2	Harb (2008)
Red Sea coast, Sudan	77±48	35±15	56±16	53±19	Sam *et al.* (1998)
East coast of Orissa, India	180±25	350±20	2825±50	1925±718	Mohanty *et al.* (2004)
Cox's Bazaar, Bangladesh	525±124	28±10	49±17	65±20	Ahmed *et al.* (2014)
Brazil beaches (HBRA)	63±32	313±197	1387±424	985±348	Veiga *et al.* (2006)
South west coast, Australia	109±70	16±13	18±16	23±19	De Meijer *et al.* (2001)
Samila Beach, Thailand	869±118	31±4	23±2	65±8	Kessaratikoon *et al.* (2015)
North Sea coast, Europe	145±67	46±41	54±49	60±51	De Meijer and Donoghue (1995)
World average for soils	420	33	45	60	UNSCEAR (2000)

5.3.2 Comparison of results obtained from the Mrima area with related studies

The results obtained in and around Mrima Hill and were compared with previous studies (Patel, 1991; Kebwaro, 2009) to investigate the variation in radiation exposure between the surveys, as well as evaluate the performance of the *in-situ* $\gamma-$ray spectrometry method in relation to radiation survey meter measurements and *ex-situ* analysis of soil samples. Towards this goal, measured dose-rates in the southern part of Mrima Hill were interpolated by the Kriging technique (Webster and Oliver, 2007) and compared with published values reported by Patel (1991). Furthermore, the measured dose-rates and natural radionuclides concentrations in villages bordering Mrima Hill, namely Mwabovo, Bumbuni, Mwachanongo and Mrima TM were compared with the findings of Kebwaro (2009) for soil sampled from the villages and γ-ray spectrometry measurements performed using a shielded laboratory based 3" × 3" NaI(Tl) detector.

5.3.2.1 Comparison of Mrima Hill dose-rates with Patel (1991) values

It was found necessary to investigate the accuracy of the survey meter used for recording dose-rate readings by Patel (1991) after a large discrepancy was noted. This was done by comparing the published dose-rates of a 5 μCi ^{133}Ba source at various source-detector distances (Patel, 1991) with reverse-calculated values estimated using Eq. A.1 in Appendix A.2, given by Chabot (2011). The comparison (Fig. 5.16) indicates that dose-rates reported by Patel (1991) were higher by a factor of 1.8 on average suggesting that the calibration factor used to adjust the survey meter was incorrect. Consequently, the dose-rates reported by Patel (1991) were decreased by a factor of 1.8, as shown in Fig. 5.17 (a), while interpolated dose-rates on the southern part of Mrima Hill (present study) are shown in Fig. 5.17 (b).

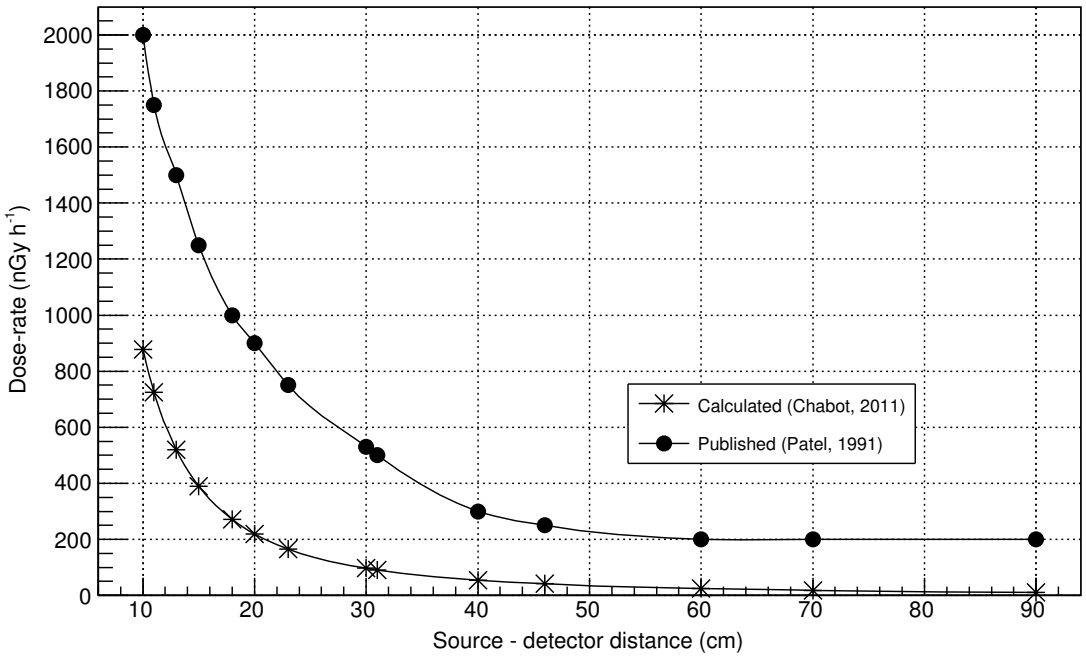

Fig. 5.16: Comparison of calculated and published calibration curves for a 5 μCi un-shielded ^{133}Ba source.

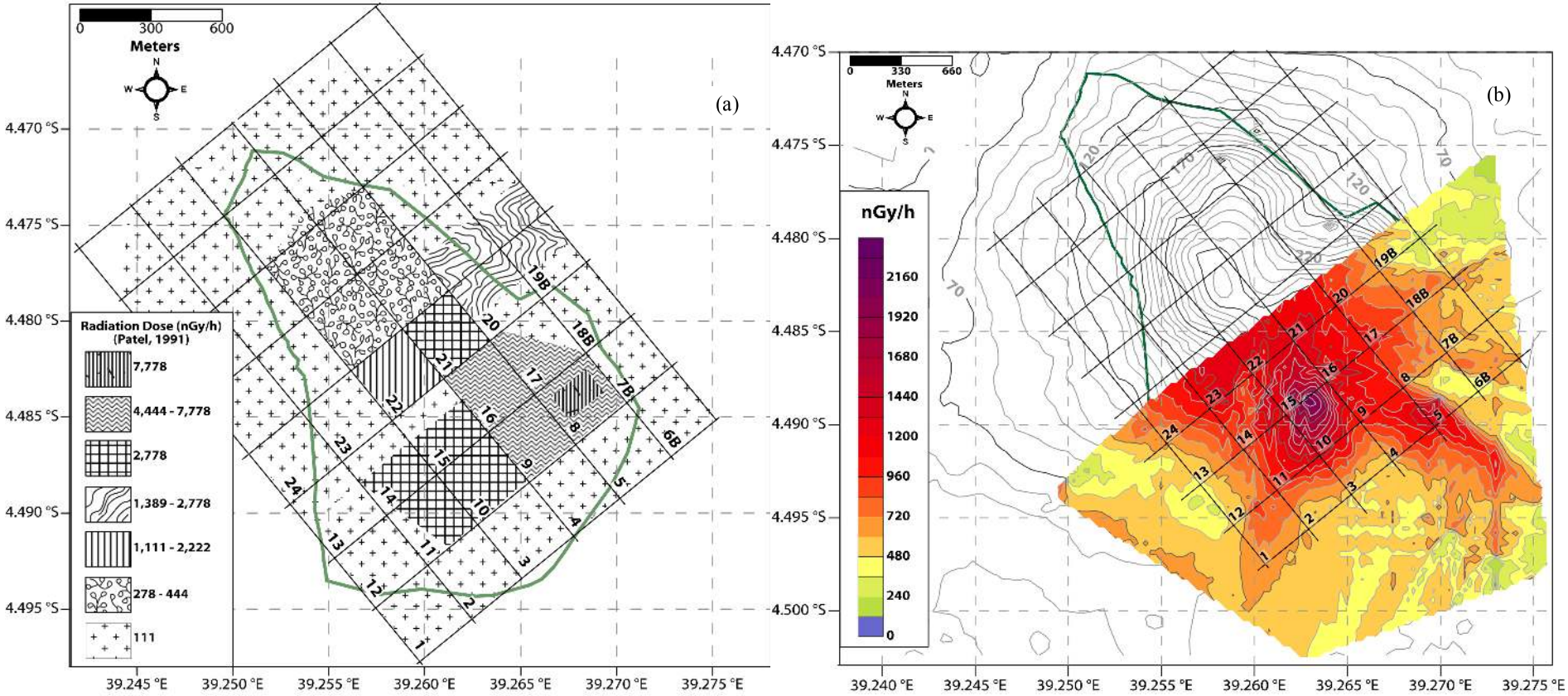

Fig. 5.17: (a) Gamma dose-rate iso-curves of Mrima Hill (adapted from: Patel (1991)); the values are lower by a factor of 1.8, and are reported in nGy/h after conversion from the originally published units of mR/h. (b) Interpolated gamma dose-rates in the southern part of Mrima Hill and overlaid by the Patel (1991) sampling grid.

A comparison of the interpolated dose-rate values with the revised Patel (1991) values is presented in Table 5.12 and Fig. 5.18.

Table 5.12: Comparison of absorbed gamma dose-rates on Mrima Hill compared with published values

	Dose-rate (nGy h^{-1})		
Grid	Patel (1991)‡	Present study†	RSD (± %)
1	≤ 111	745±44	105
2	≤ 111	720±122	104
3	≤ 111	778±182	106
4	≤ 111	1010±78	113
5	≤ 111	585±138	96
6B	≤ 111	601±31	97
7B	≤ 111	614±38	98
8	6667 (4444 - 7778)	804±66	111
9	6111 (4444 - 7778)	1074±29	99
10	≤ 2778	1473±215	43
11	1036 (111 - 1960)	1137±149	7
12	≤ 111	670±78	101
13	≤ 111	757±114	105
14	1036 (111 - 1960)	1051±102	1
15	1036 (111 - 1960)	1391±92	21
16	6111 (4444 - 7778)	1129±88	97
17	4111 (111 - 7778)	850±65	93
18B	≤ 111	614±129	98
19B	1426 (111 - 2778)	530±65	65
20	1426 (111 - 2778)	801±105	40
21	≤ 2778	1147±43	59
22	1667 (111 - 2222)	1220±21	22
23	≤ 111	1220±27	118
24	≤ 111	914±115	111

‡ Midrange values. Ranges in brackets.

†Median ± MAD

Although an almost similar pattern of absorbed gamma dose-rates can be observed in the sampling grids 1 - 24 (see Fig. 5.18), there is still a large variation between the two measurements. This could be attributed to significant differences inherent in the detector responses to gamma radiation and associated gamma photon energies. Compared to gas-filled detectors, scintillation detectors have a greater efficiency and

better linear response to high energy γ-rays. The variation could also be indication of the redistribution of radioactive minerals in Mrima Hill due to geochemical processes such as weathering and mineral leaching, given the temporal difference between the two measurements i.e. 2014 and 1987.

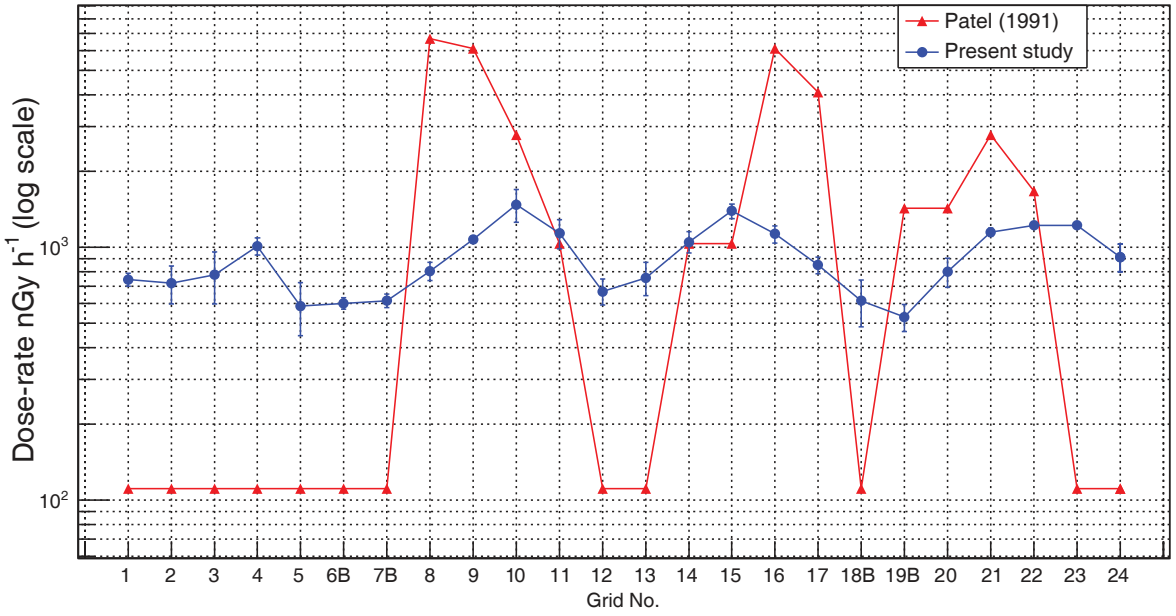

Fig. 5.18: Comparison of measured gamma dose-rates in the southern part of Mrima Hill with Patel (1991) values. Lines have no significance, they are used for visual guidance. Raw data is presented on Table 5.12.

5.3.2.2 Comparison of Mrima villages results with Kebwaro (2009) values

A comparison of the results obtained in the present study with Kebwaro (2009) values is given in Table 5.13. It was observed that mean activity concentrations of ^{40}K, ^{238}U and ^{232}Th in both studies were varied but the absorbed gamma dose-rate values were comparable. It may be noted that ^{238}U and ^{232}Th values reported by the *in-situ* method (present study) were higher by up to 26% and 31%, respectively compared to values reported by the *ex-situ* analysis method (Kebwaro, 2009). This variation could be attributed to the differences in locations or origin of samples and detector geometries employed. The PGIS-2 portable detector quantifies a relatively large volume radioactivity source (30 cm thickness of earth surface within 10 m radius in the

field) compared to the small volume source (500 ml processed sample) measured by a laboratory shielded detector. However, accuracy of the *in-situ* method is greatly affected by topographic effects, the distribution of radionuclides and soil moisture (IAEA, 2003). The method also assumes radioactive equilibrium of ^{214}Bi with ^{238}U in the U decay series, which is not necessarily the case due to environmental effects.

Table 5.13: Comparison of mean activity concentrations of ^{40}K, ^{238}U and ^{232}Th and absorbed gamma dose-rates around the Mrima Hill with published values

Location	Mean activity (Bq kg^{-1})			Dose-rate (nGy h^{-1})	Reference
	^{40}K	^{238}U	^{232}Th		
Around Mrima Hill	401±21	240±17	626±27	408±20	Present study
	769±21	187±15	465±23	402±19	Kebwaro (2009)

It may be concluded that both the *in-situ* method and conventional measurements of field samples in the laboratory (*ex-situ*) can complement each other in environmental radioactivity monitoring. The *in-situ* method may be adapted for preliminary radiometric studies for identification of radiation hot spots while the soil sampling followed by laboratory analysis method may be adapted for determination of specific activity concentrations in specified locations.

5.3.3 Comparison of results obtained from the Mrima-Kiruku complex with other HBRA in Kenya and elsewhere

A comparison of results obtained in the Mrima-Kiruku complex with published values from other HBRA of Kenya and elsewhere is presented in Table 5.14. It was observed that the means of ^{238}U and ^{232}Th in Kiruku foothills are comparable with values reported for carbonatite rocks by Mustapha (1999). The values of ^{238}U reported in Mt. Homa (Otwoma *et al.*, 2013) and Lambwe east (Achola *et al.*, 2012) were comparable to the means of the foothills of both Mrima and Kiruku Hills. The means of ^{232}Th in the complex are however much higher than values reported in Mt. Homa and Lambwe

east. It was however noted that the values of ^{40}K and absorbed dose-rates reported in Lambwe east (approximately 1000 m ASL) are much higher compared to values reported in the present study, perhaps due to the cosmic radiation factor. Compared to other HBRA in the world such as Ramsar in Iran (Sohrabi, 1993) and Guarpari in Brazil (Cullen and Franca, 1977), the Mrima-Kiruku complex may be classified as a low HBRA (< 5 mSv/y) without considering other sources of exposure such as cosmic radiation and internal exposures, according to Sohrabi (2013).

Table 5.14: Comparison of mean activity concentrations of ^{40}K, ^{238}U and ^{232}Th, gamma dose-rates and AEDE in the Mrima-Kiruku complex with published values in Kenya and elsewhere

	Activity (Bq kg^{-1})			Dose-rate	AEDE	
Location	^{40}K	^{238}U	^{232}Th	(nGy h^{-1})	(mSv)	Reference
Mrima Hill	381±28	326±24	1817±51	967±36	2.371±0.089	Present study
Mrima foothills	235±19	205±15	1168±26	689±19	1.691±0.048	Present study
Kiruku Hill	603±28	73±14	927±31	705±27	1.730±0.067	Present study
Kiruku foothills	460±22	104±11	833±33	506±24	1.241±0.059	Present study
Kenya (Carbonatites)	186±27	179±70	950±21	-	-	Mustapha (1999)
Mt. Homa, Kenya	916	195	410	383	0.470	Otwoma *et al.* (2013)
Lambwe east, Kenya	1397	179	509	2300	5.7	Achola *et al.* (2012)
Ramsar, Iran	-	-	-	-	10.2	Sohrabi (1993)
Kerala, India	-	-	-	-	3.8	Sunta (1993)
Guarpari, Brazil	-	-	-	-	5.5	Cullen and Franca (1977)
Yangjiang, China	-	-	-	-	3.5	Luxin *et al.* (1990)
World average for soil	420	33	45	60	0.074	UNSCEAR (2000)

- data not reported

5.4 EDXRF analysis results for soil samples

The results obtained from analysis of the SARM 69 (clay potsherd) certified reference material (CRM) by the Spectro X-Lab 2000 EDXRF spectrometer are tabulated in Table 5.15, and compared with the CRM's certified values in order to determine accuracy of the EDXRF technique. The detection limit (DL) and relative standard deviation (RSD) values for individual elements are also presented. It may be observed that RSD of the measurements for elemental analyses with the exception of Th was better than 19%. The poor RSD (53.6%) for Th could be due to its low concentration in the SARM 69 CRM and hence poor signal-to-noise ratio, or peak interference.

Table 5.15: Comparison of selected measured and certified elemental concentrations of the SARM 69 CRM

	DL (%)	Certified (%)	Measured (%)	RSD (± %)		DL (μg g^{-1})	Certified (μg g^{-1})	Measured (μg g^{-1})	RSD (± %)
Si	0.3	31.13	26.75±0.04	10.7	Y	0.8	29	36±1	16.2
Fe	0.011	5.02	4.94±0.005	1.1	Zr	0.8	271	270±1	0.3
K	0.12	1.63	1.60±0.004	1.2	Nb	0.9	9	12±0.3	18.4
P	0.05	0.12	0.13±0.002	2.1	La	2.5	-	23±2	
					Ce	3	67	69±3	1.6
					Nd	2	30	23±4	18.7
					Th	2	9	20±1	53.6
					U	2	-	19±1	

- data not reported

The elemental concentrations in soil samples from sites representing both low and high natural radioactivity levels were determined by EDXRF analysis. A summary of sample descriptions and selected results are provided in Table B.1 in Appendix B.4 and Table 5.16, respectively. In the context of this thesis, only selected light, heavy and light REEs (LREEs including Y) results were considered in order to help understand the mineralogy and geochemical behaviour of U and Th in the study area.

Table 5.16: Mean concentrations of selected light-, heavy-, LREEs- and radio-elements in soil samples characterized by EDXRF

	Location	Si (%)	P (%)	K (%)	Fe (%)	Y (μg g^{-1})	Zr (μg g^{-1})	Nb (μg g^{-1})	La (μg g^{-1})	Ce (μg g^{-1})	Nd (μg g^{-1})	Th (μg g^{-1})	U (μg g^{-1})
1	Bwiti Junction												
	foot path	43.6±0.7	< 0.015	0.311±0.003	0.149±0.006	8.8±0.7	178±18	7.3±0.5	23.4±3.9	35±6	24±5	11.0±1.3	11.5±1.2
	farm	43.9±0.4	0.049±0.003	0.232±0.002	0.515±0.007	20.0±04	425±3	27.1±0.9	49.5±2.4	83±7	37±18	14.4±0.8	11.3±1.5
	roadside	38.1±0.6	0.084±0.008	0.245±0.015	0.557±0.012	21.5±0.9	283±14	41.3±1.6	63.3±5.3	108±5	45±11	6.4±0.8	1.9±0.5
2	Ramisi quarry	44.2±0.5	< 0.015	< 0.12	0.060±0.001	10.7±0.7	283±12	8.6±0.6	30.0±2.4	48±7	19±13	13.3±1.3	11.2±1.9
3	Bodo coastline	37.4±0.4	0.042±0.016	0.619±0.003	0.401±0.008	12.1±1.8	376±7	9.4±0.8	28.6±3.6	48±3	22±9	14.1±0.6	11.6±1.1
4	Munje coastline												
	soil	29.7±0.4	0.309±0.003	0.874±0.006	2.511±0.011	35.7±1.0	637±4	17.9±0.7	57.8±2.3	104±3	43±18	20.0±1.2	12.0±1.6
	sand	40.9±0.9	0.010±0.006	< 0.12	0.031±0.001	7.3±1.5	36±5	5.3±0.8	18.8±3.8	24±3	13±4	12.6±2.1	17.0±2.7
5	Ramisi roadside	43.1±0.8	0.026±0.002	0.720±0.009	0.137±0.005	16.2±1.3	623±11	11.8±0.9	42.1±1.9	64±3	30±6	20.5±2.7	18.3±3.5
6	Bumbuni village												
	open field	30.1±0.2	0.124±0.002	0.787±0.003	4.001±0.007	54.8±1.2	595±6	116±1	134±3	218±6	80±5	31.7±1.6	20.2±1.3
	foot path	32.7±0.3	0.149±0.004	0.267±0.006	2.496±0.013	75.7±2.1	318±7	206±2	413±8	497±10	180±14	39.2±2.9	10.8±4.3
	homestead	34.1±0.5	0.214±0.005	0.485±0.006	1.364±0.015	52.1±0.9	331±9	131±2	189±3	302±7	94±14	19.6±1	6.6±1.3
7	Mrima												
	southern foothills	9.7±0.3	1.212±0.012	0.410±0.009	19.095±0.112	926±12	627±26	2692±37	8120±97	10110±91	3580±27	444±10	27.9±5.7
8	Menzamwenye												
	roadside	22.3±0.1	0.941±0.025	0.668±0.010	9.415±0.036	496±13	575±4	1190±25	1979±41	3078±102	1109±22	143±12	45.4±21.1
	roadside†	3.7±0.1	1.771±0.035	0.218±0.016	26.25±0.133	933±8	198±6	2050±17	3435±41	7544±89	2622±21	293±16	123±7
9	Marenji farm	37.7±0.5	0.064±0.007	0.379±0.032	0.934±0.055	20.7±3.2	641±15	24±2	36.0±6.3	63.2±2.5	22±4	17.4±4.3	12.6±6.6
10	Kiruku Hill												
	southern hill base	24.9±0.4	0.245±0.007	3.390±0.054	5.553±0.051	254±5	414±9	487±5	551±11	1021±17	376±45	227±3	23.3±5.1
	southern hill slopes	14.7±0.1	0.357±0.003	0.653±0.010	17.24±0.091	457±5	311±7	986±5	1952±24	2984±13	1312±36	349±6	29.2±5.3
	southern hill slopes†	5.0±0.1	0.244±0.006	0.156±0.008	32.69±0.313	264±3	126±8	693±4	23±5	4679±66	< 10	318±15	23.5±9.4
	hill crest	17.6±0.3	0.323±0.005	0.644±0.008	12.61±0.031	509±7	389±21	1083±14	1614±22	2258±8	742±91	334±5	16.4±6.1
	hill crest†	10.0±0.8	0.265±0.017	0.234±0.024	22.40±1.675	450±39	191±13	687±52	< 5	6085±430	1930±288	447±36	45.5±6.3
	northern hill slope	20.4±0.1	0.340±0.003	1.497±0.015	8.90±0.053	432±4	429±9	970±5	1241±15	1760±18	537±7	287±7	26.3±2.6
	northern foothills	27.5±0.5	0.179±0.005	0.702±0.003	3.58±0.060	117±2	907±16	284±4	383±9	370±3	148±9	89.1±2.1	14.7±2.4

†Rock fragments weighing > 5 % of total soil sample mass

5.4.1 Composition of REEs, Th and U in soil samples

Assessment of the isotopic and elemental compositions of U and Th is beneficial in for example, determining provenance of geological samples and the implications of processes such as erosion and deposition (Hawkesworth *et al.*, 1997). In addition, the assessment of REEs provides better insight to the geochemical behaviour of Th and U and is also important in mineralogy (Verplanck and van Gosen, 2011; Sahoo *et al.*, 2011).

The concentration of LREEs, Th and U ranged < 5 μg g^{-1} - > 10 % with a general increment observed in the Mrima-Kiruku complex samples (see Table 5.16). High concentrations of especially Th and LREEs can be attributed to carbonatites and lateritic soil of the Mrima-Kiruku complex (Baker, 1953; JICA, 1993). It may be noted that Si concentration (ranged 3.7% - < 45 %), which implies quartz in sand, was particularly high in samples collected along the south coast paved road and adjoining environs compared with samples from the Mrima-Kiruku complex.

Five samples spatially distributed within the study area were selected to assess the pattern of LREEs, Th and U, as shown in Fig. 5.19. It can be observed that there is no significant variation in the concentration of LREEs relative to location, which suggests that the minerals forming these elements are similar. Nonetheless, there is variation of Th and U concentrations with location which confirms alteration of these elements, possibly due to geochemical processes such as leaching and weathering.

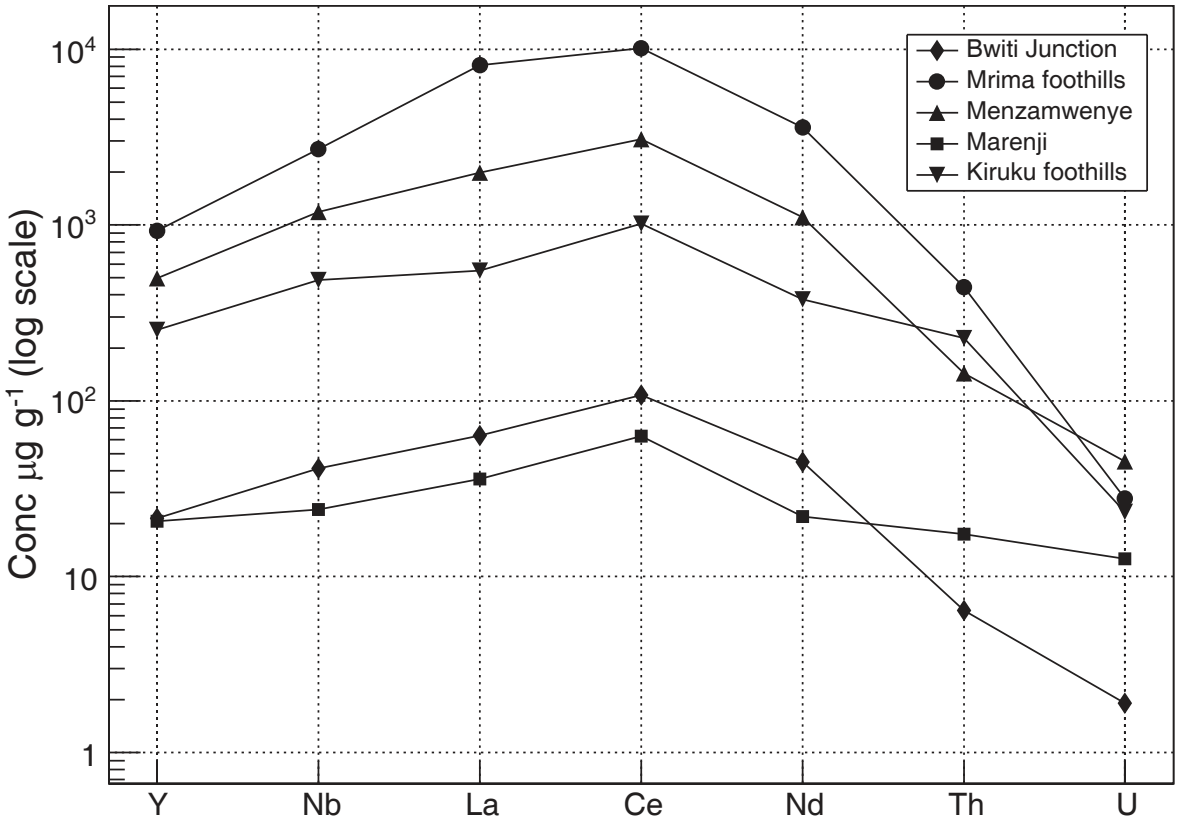

Fig. 5.19: Patterns of normalized LREEs, Th and U concentrations in the soil samples. Lines have no significance, they are used for visual guidance.

An attempt to establish the presence of monazite [(Ce, La, Nd, Th)(PO_4, SiO_4)] in the soil samples showed that Th correlates positively with Ce, Nd, La and P, see Table 5.17. Furthermore, comparison of P, Ce, La, Nd, and Th in samples collected from three different locations, namely southern foothills of Mrima Hill, Menzamwenye (near the south coast paved roadbed) and Bwiti Junction (roadside) showed elevated concentrations of the elements in the Mrima and Menzamwenye samples, see Table 5.18. There is also significant correlation of Th/La, Th/Ce and Th/Nd ratios in these samples which suggests that murram roadbed on the south coast paved road section found with elevated ^{238}U and ^{232}Th levels is likely to have originated from the Mrima Hill area.

Table 5.17: Pearson's correlation matrix for selected elements measured in the soil samples by EDXRF analysis

	Si	P	K	Fe	Y	Zr	Nb	La	Ce	Nd	Th	U
Si	1											
P	-0.69	1										
K	-0.09	-0.03	1									
Fe	-0.94	0.62	-0.1	1								
Y	-0.85	**0.89**	0.05	**0.77**	1							
Zr	0.09	0.04	0.26	-0.28	-0.03	1						
Nb	-0.8	**0.89**	0.02	0.72	**0.98**	0.03	1					
La	-0.56	**0.78**	-0.02	0.47	**0.84**	0.18	**0.92**	1				
Ce	-0.84	**0.81**	-0.13	**0.85**	**0.91**	-0.12	**0.92**	**0.81**	1			
Nd	-0.72	**0.84**	-0.07	0.66	**0.92**	0.00	**0.92**	**0.88**	**0.93**	1		
Th	-0.9	0.55	0.15	**0.86**	**0.85**	-0.14	**0.80**	0.61	**0.85**	**0.77**	1	
U	-0.64	**0.84**	-0.04	0.64	0.74	-0.19	0.65	0.42	0.66	0.67	0.49	1

- 'Strong' correlation coefficient: > 0.75 (in bold)

- 'Moderate' correlation coefficient: 0.50 - 0.75

- 'Weak' correlation coefficient: 0.35 - 0.50

Table 5.18: Elemental concentrations and ratios for monazite constituents in selected soil samples characterized by EDXRF analysis

Location	P (%)	La (μg g^{-1})	Ce (μg g^{-1})	Nd (μg g^{-1})	Th (μg g^{-1})	Th/P	Th/La	Th/Ce	Th/Nd
A	0.084±0.008	63.3±5.3	108±5	45±11	6.4±0.8	0.536	0.101	0.059	0.142
B	1.212±0.012	8120±97	10110±91	3580±27	444±10	0.366	0.055	0.044	0.124
C	0.941±0.025	1979±41	3078±102	1109±22	143±12	0.152	0.072	0.046	0.129

[A]Bwiti junction roadside $\approx$ 30 m from paved road

[B]Southern foothills of Mrima Hill

[C]Menzamwenye junction $\approx$ 8 m near the south coast paved roadbed

5.4.2 Analysis of K, U and Th by *in-situ* gamma-ray and EDXRF spectrometry

In-situ $\gamma-$ray spectrometry measurements made within the vicinity ($\approx$ 10 m radius) of the soil sampling points were estimated for determination of K, U and Th elemental concentrations and compared with EDXRF analysis results, as shown in Fig. 5.20.

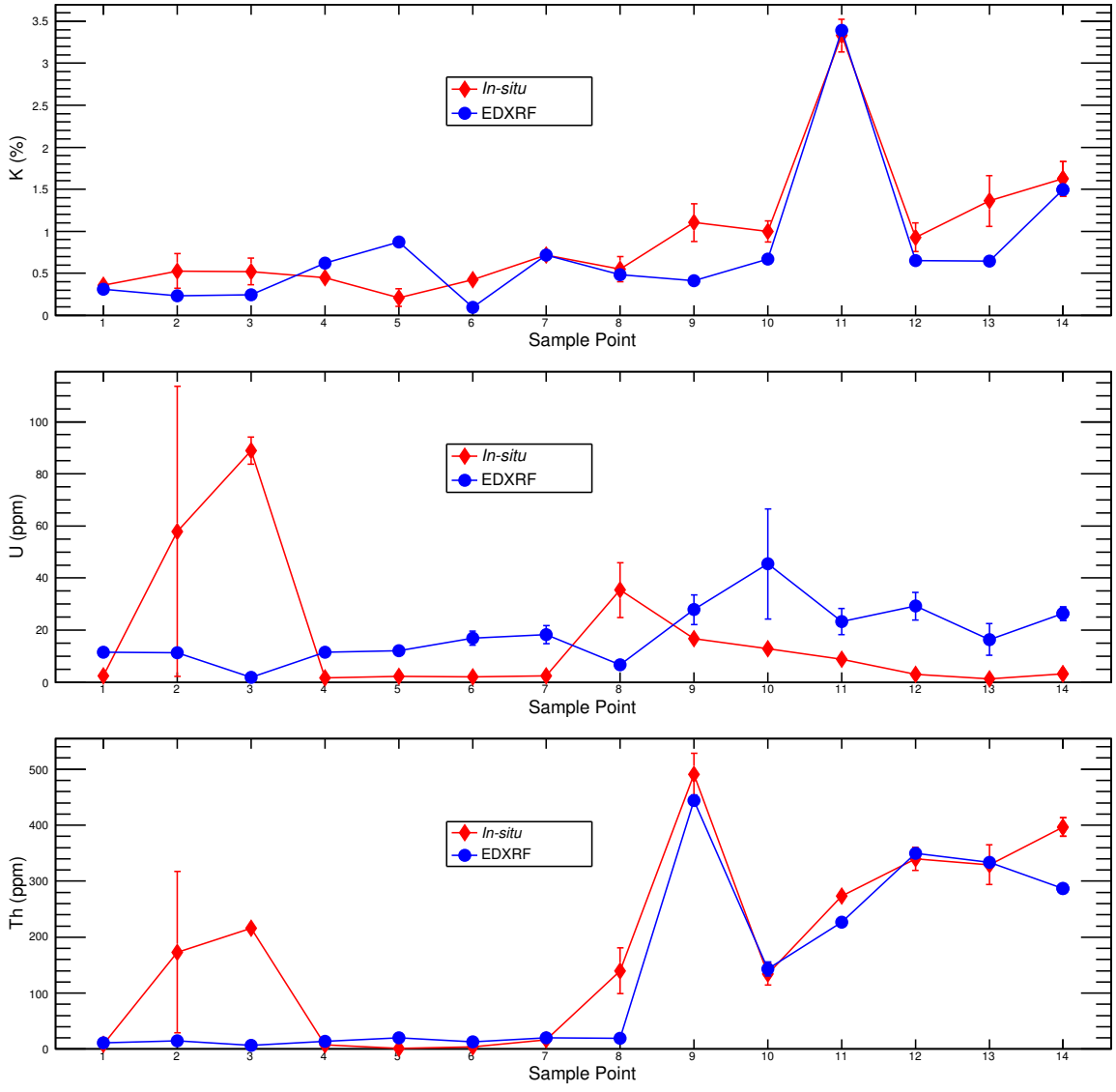

Fig. 5.20: Comparison of K, U and Th concentrations measured by *in-situ* $\gamma-$ray spectrometry survey and EDXRF spectrometric analysis of surface soil samples. Greyed out points indicate BDL and are shown for completeness of information. See Table 5.19 for raw data and sample point locations.

Generally, it may be observed that results obtained by *in-situ* $\gamma-$ray spectrometry and EDXRF analysis are comparable especially for K and Th (see Fig 5.21 and Table 5.19), and appear to correlate better at the Mrima-Kiruku complex (sampling points 8 - 14), than at the south coast paved road environs (sampling points 1 - 7).

Table 5.19: Comparison of K, U and Th elemental concentrations by *in-situ* $\gamma-$ray and EDXRF spectrometric measurements

		EDXRF			*In-situ* $\gamma-$ray spectrometry		
	Location	K (%)	U (ppm)	Th (ppm)	K (%)	eU (ppm)	eTh (ppm)
1	Bwiti Junction foot path	0.311±0.003	11.5±1.2	11.0±1.3	< 0.645	< 3.6	8.8±1.4
2	Bwiti Junction farm	0.232±0.002	11.3±1.5	14.4±0.8	< 0.645	57.9±55.6	173.2±144
3	Bwiti Junction roadside	0.245±0.015	1.9±0.5	6.4±0.8	< 1.5‡	88.8±5.2	216±8.4
4	Bodo coastline	0.619±0.003	11.6±1.1	14.1±0.6	< 1.5‡	< 9.1‡	< 15.8‡
5	Munje coastline soil	0.874±0.006	12.0±1.6	20.0±1.2	< 1.5‡	< 9.1‡	< 15.8‡
6	Munje coastline sand	< 0.12	17.0±2.7	12.6±2.1	< 1.5‡	< 9.1‡	< 15.8‡
7	Ramisi roadside	0.720±0.009	18.3±3.5	20.5±2.7	< 1.5‡	< 9.1‡	16.7±1.5
8	Bumbuni village homestead	0.485±0.006	6.6±1.3	19.6±1	< 0.645	35.4±10.5	140±41.2
9	Mrima southern foothills	0.410±0.009	27.9±5.7	444±10	1.104±0.225	16.7±2.8	491.1±37
10	Menzamwenye roadside	0.668±0.010	45.4±21.1	143±12	0.996±0.126	12.8±2.6	134.2±19.4
11	Kiruku southern hill base	3.390±0.054	23.3±5.1	227±3	3.330±0.193	8.88±1.1	273.4±6.4
12	Kiruku southern hill slopes	0.653±0.010	29.2±5.3	349±6	0.928±0.172	< 3.6	339.8±20.6
13	Kiruku hill crest	0.644±0.008	16.4±6.1	334±5	1.361±0.304	< 3.6	329.5±35.5
14	Kiruku northern hill slope	1.497±0.015	26.3±2.6	287±7	1.625±0.205	< 3.6	396.8±16.9

‡ PGIS-21 spectrometry measurements, hence different MDA reported

It may also be noted that results obtained for U and Th by *in-situ* $\gamma-$ray spectrometry were higher than those obtained by EDXRF in sampling points 2 and 3, located at the Bwiti junction. This variation was attributed to the differences in the methods of calibration between the two analytical techniques. As discussed earlier in Sub-section 5.2.3, U and Th anomalies were confined to the paved and side road intersections. Whereas the *in-situ* $\gamma-$ray spectrometry method averages the gamma radiation field within a radius of 10 m (in this case, the paved and side roads were in the vicinity of the sampling points), analysis by the EDXRF method was made directly on a split ($\approx$ 2.5 g) from a much smaller sample volume ($\approx$ 50 g). Also, ground attenuation effects such as soil cover and moisture levels were not taken into consideration in the EDXRF analysis results.

Furthermore, the *in-situ* $\gamma-$ray spectrometry method determines an equivalent uranium value from the ^{214}Bi peak and an equivalent thorium value from the ^{208}Tl gamma peak and assumes equilibrium in the natural radioactive decay series (IAEA, 2003). However, disequilibrium in the decay series, particularly for U due to radon gas escape and changes to the geochemical environment, could be a possible cause for differing results between EDXRF and *in-situ* $\gamma-$ray spectrometry.

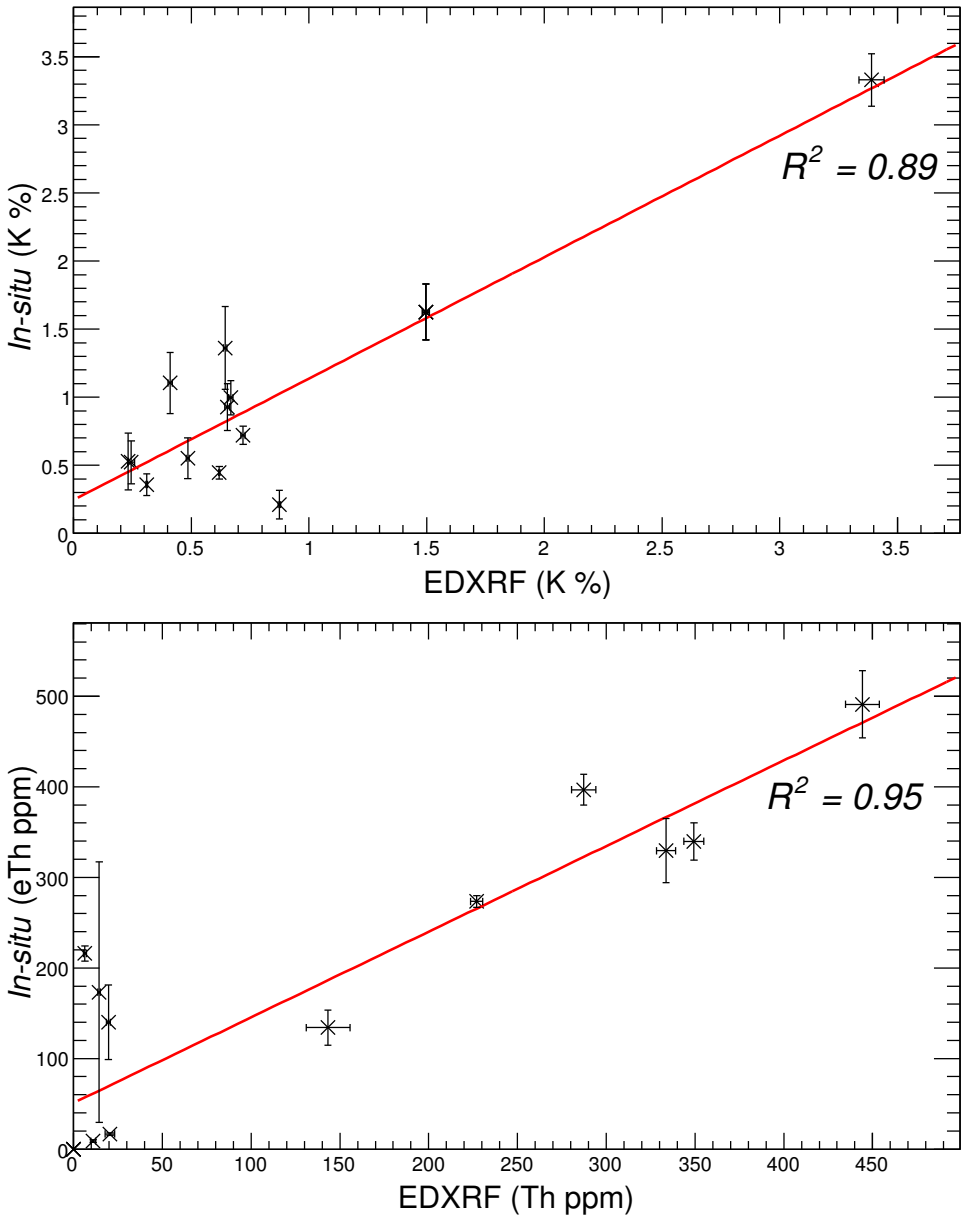

Fig. 5.21: Correlation plot for K and Th elemental concentration values by *in-situ* $\gamma-$ray and EDXRF spectrometric measurements.

5.5 Exploratory analysis of activity concentration values

This section presents the multivariate exploratory analysis results of activity concentration values presented in Section 5.2 utilizing the PCA technique. Ternary diagrams were used to complement the PCA results by assessing the variability of measured natural radionuclide concentrations. It was found that the spatial variability of the HBR anomaly in the study area is mainly constrained by anthropogenic activities, underlying geology and geochemical processes in the terrestrial environment.

5.5.1 PCA of activity concentration values in the south coast paved road and adjoining environs

The data-set used in this study consists of a matrix $X_{38\times3}$ in which the rows (38) correspond to surveyed sites of the south coast paved road and adjoining environs i.e. areas defined by $\gamma-$ray spectral sampling gates on the dose-rate maps[4] presented in Sub-section 5.2.2 and 5.2.3, and columns (3) correspond to activity concentrations of ^{40}K, ^{238}U and ^{232}Th. PCA results show that 99.1 % of total variance in the data can be explained by the first and second principal components (PC1 and PC2), see Table 5.20.

From the Table 5.20, it may be observed that all variables have a positive projection on PC1 which accounts for 82.1% of the total variance; PC1 thus explains the main process (in this case, NORM) controlling radioactivity in the survey area. PC2 which accounts for 17.0% of the variance contrasts between ^{40}K (positive projection) and ^{238}U and ^{232}Th (negative projections). The loadings can be understood as weights of each original variable used in the calculation of the principle components. So, the positive and negative projections highlight an antithetic behavior of K and U-Th elements due to their enrichment/strong influence (corresponding to high PC2 loadings) or low influence (corresponding to low PC2 loadings) in ^{40}K, related to a predominance in

[4]The data-set includes additional gates not shown in the gamma dose-rate maps

leaching of K-bearing minerals. This is so because K is geochemically mobile under most weathering conditions whereas Th and U, being less mobile, are readily adsorbed and retained by clay minerals (Chan *et al.*, 2007).

Table 5.20: PCA loadings of activity concentration values in the south coast paved road and environs

	PC1	PC2	PC3
^{40}K	0.503	0.858	0.107
^{238}U	0.602	-0.436	0.669
^{232}Th	0.620	-0.272	-0.735
Standard deviation	1.570	0.715	0.158
Proportion of variance	0.821	0.170	0.008
Cumulative proportion	0.821	0.991	1

From the PCA bi-plot shown in Fig. 5.22, it may be observed that the sites (e.g. roadsides and the road environs) which are characterized by the lowest gamma dose-rates (i.e. < 60 nGy h^{-1}), are projected with the lowest PC1 values, while sites (e.g. side road intersections) with the highest gamma dose-rates (i.e. > 450 nGy h^{-1}), are projected at the other end of the axis. This means that the HBR anomaly is related to the road paving materials in this case, murram (laterite). Similarly, paved roads had the highest PC2 values which could be an indication of minimal weathering of the underlying murram roadbeds. Some of the roadside and side road sites however had lower PC2 values, indicating intense leaching of K-bearing mineral constituents.

The ternary plot shown in Fig. 5.23 illustrates the relative proportions of natural radionuclide concentrations in the south coast paved road and adjoining environs. It may be observed that areas adjoining the paved road (i.e. roadsides and paved road environs) show a trend towards high ^{40}K (> 50 - < 80% contribution) and low ^{232}Th and ^{238}U (< 30% contribution), whereas the side road intersections show enhanced ^{232}Th and ^{238}U (70 - 90% and 30 - 60% contribution, respectively) and low ^{40}K (10 -

30% contribution). A number of surveyed roadsides (i.e. sites adjacent to the side-road intersections) however show a trend towards high ^{232}Th and ^{238}U (70 - 90% and 35 - 50% contribution, respectively) and low ^{40}K (> 30% contribution). Along the paved road, contribution of ^{232}Th varies between 40 - 80%, while that of ^{238}U and ^{40}K varies between 20 - 40% and 20 - < 60%, respectively.

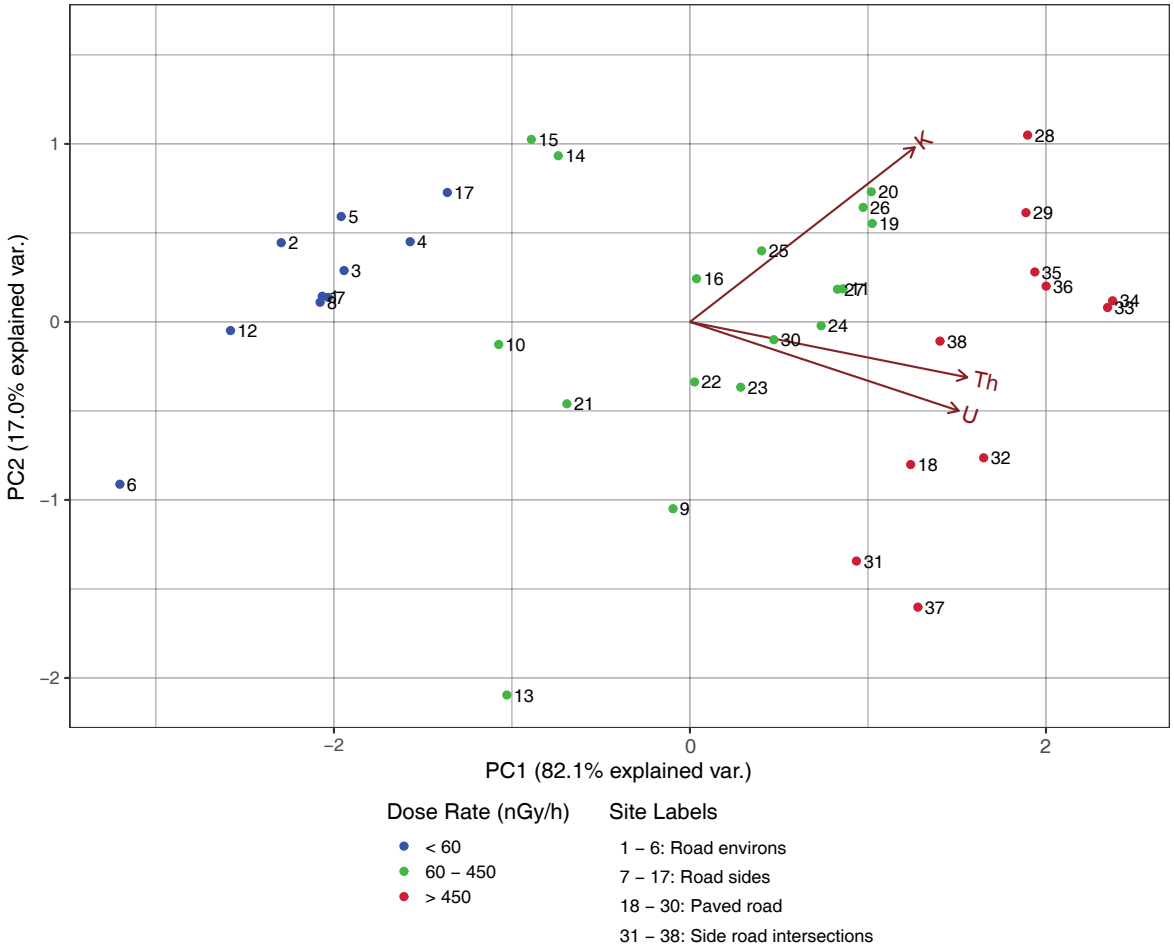

Fig. 5.22: PCA bi-plot of activity concentration values in the south coast paved road and environs. The horizontal axis shows data projections on PC1, and the vertical axis, PC2. Data points are spatially plotted at their projections on the PCs and coloured according to dose-rate values. Red arrows show the projections of ^{40}K, ^{238}U and ^{232}Th on the PCs.

It may also be observed that the Th/K ratios in the paved road and side road intersections were higher (> 1.0) compared to the roadsides and paved road environs. This shows that the the road paving materials had been ferried from elsewhere. Furthermore, a

majority of paved road sites are characterized by slightly lower (< 1.5) Th/K ratios compared to the side road intersection sites (> 1.5), indicating minimal abrasion of bitumen paving and thus minimal leaching of K. It may thus be concluded that the spatial variability of the HBR anomaly in the south coast paved road and environs, is influenced mostly by anthropogenic activities i.e. relocation of murram (containing enhanced NORM) from a HBRA to previously uncontaminated sites for the purpose of road construction, and geochemical processes in the terrestrial environment.

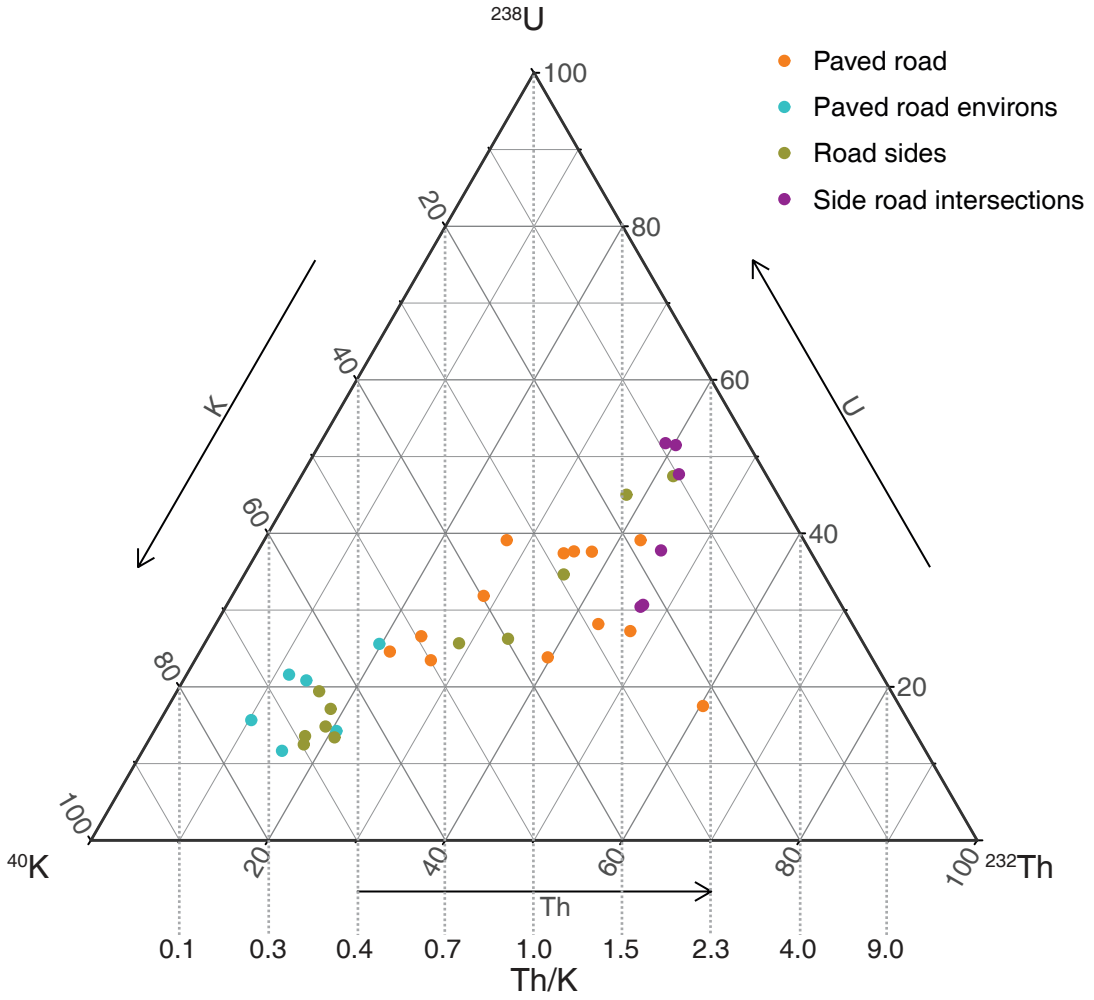

Fig. 5.23: Ternary diagram of percent relative activity concentrations of ^{40}K, ^{232}Th and ^{238}U in the south coast paved roads and environs. Activity ratios of Th/K are shown in dotted lines; sites with minimal leaching of K are characterized by < 1.0 ratios, whereas sites that are characterized by > 1.0 ratios indicate intense leaching of K or relocation of NORM.

5.5.2 PCA of activity concentration values in the Mrima-Kiruku complex

The data-set used in this study consists of a matrix $X_{79\times3}$ in which the rows (79) correspond to all surveyed sites within the Mrima-Kiruku complex i.e. areas defined by $\gamma-$ray spectral sampling gates on the gamma dose-rate maps[5] presented in Sub-section 5.2.4 and 5.2.5, and columns (3) correspond to activity concentrations of ^{40}K, ^{238}U and ^{232}Th. PCA results show that PC1, PC2 and PC3 account for 54.6 %, 31.0 % and 14.4 % of total variance, respectively (see Table 5.21).

Table 5.21: PCA loadings of activity concentration values in Mrima-Kiruku complex

	PC1	PC2	PC3
^{40}K	-0.373	-0.897	0.240
^{238}U	-0.627	0.434	0.647
^{232}Th	-0.684	0.091	-0.724
Standard deviation	1.279	0.965	0.658
Proportion of variance	0.546	0.310	0.144
Cumulative proportion	0.546	0.856	1

It may be observed that ^{238}U and ^{232}Th have the lowest contribution to the variance of PC1 compared to ^{40}K, whereas on PC2 ^{40}K correlates negatively with ^{238}U and ^{232}Th, and on PC3 ^{232}Th correlates negatively with ^{40}K and ^{238}U. PC1 shows an inverse relationship between the component and the variables, and thus discriminates sites according to their activity concentrations of ^{40}K, ^{238}U and ^{232}Th, while PC2 discriminates sites according to their deficiency in ^{40}K. PC3 discriminates sites according to their deficiency in ^{238}U and enhancement of ^{232}Th. The depletion of ^{238}U is caused by U leaching from primary minerals, in this case, monazite and pyrochlore (Baker, 1953), leaving the relative insoluble Th in high concentrations (Adams and Weaver, 1958; Dickson, 1990).

[5]The data-set includes additional gates not shown in the gamma dose-rate maps

From the PCA 3D-plot shown in Fig. 5.24, it may be observed that the surveyed areas may be classified according to site locations (and thus underlying geology), namely Kiruku Hill, Mrima Hill and Mrima environs based on the PC variations. The sites (e.g. Mrima and Kiruku Hills) which are characterized by the lowest PC1 values have the highest activity concentrations of ^{40}K, ^{238}U and ^{232}Th. The Mrima environs sites are characterized by the highest PC2 values and thus depleted ^{40}K levels. Kiruku Hill sites are characterized by both the lowest PC2 and PC3 values (Fig. 5.24), and thus the highest and lowest levels of ^{40}K and ^{238}U, respectively.

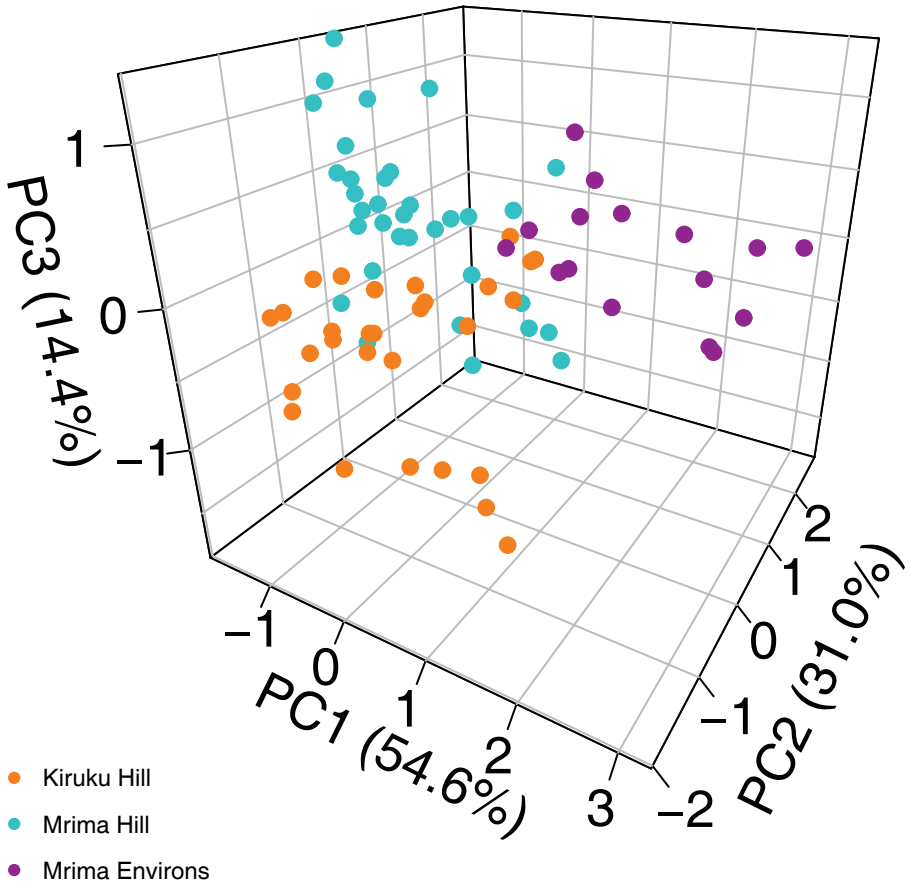

Fig. 5.24: PCA 3D-plot of activity concentration values in the Mrima-Kiruku complex. Data points are spatially plotted at their projections on the PCs and coloured according to site location.

The cluster overlap observed in some of the Kiruku Hill, Mrima Hill and Mrima environs measurements is due to similarity of soil and rock forming minerals in these areas, as shown in the ternary plot (Fig. 5.25). This plot illustrates the relative proportions of natural radioactivity concentrations in the Mrima-Kiruku complex with respect to spatial distance and geology. Furthermore, It may be observed that the Kiruku Hill sites show a relatively uniform trend characterized by high ^{40}K (> 80% contribution), low to high ^{232}Th (> 30 - < 90% contribution) and low ^{238}U (< 20% contribution). A majority of the Mrima environs sites also show a trend towards high ^{40}K (> 60% contribution), while contribution from ^{232}Th and ^{238}U varies between 30% - 70% and < 30%, respectively. In Mrima Hill, a majority of the sites show a trend towards enhanced ^{232}Th (> 60% contribution) and low ^{40}K and ^{238}U (< 40% contribution).

It may further be observed that the Th/K ratios in most of both Mrima and Kiruku Hills sites were higher compared to the Mrima Hill environs sites. The highest ratios (> 1.0) indicate intense leaching of K during weathering on the hill summits and along hill slopes of both Mrima and Kiruku Hills. Low Th/K ratios indicate the deposition of K from the hill summit and hill slopes to the foothills and environs of Mrima Hill. It may thus be concluded that spatial variability of the HBR anomaly in the Mrima-Kiruku complex, is influenced mostly by the underlying geology, and geochemical processes in the complex such as mineral leaching, weathering and sedimentation of soil and bedrock, and transportation of regolith from the hill summits toward the foothills.

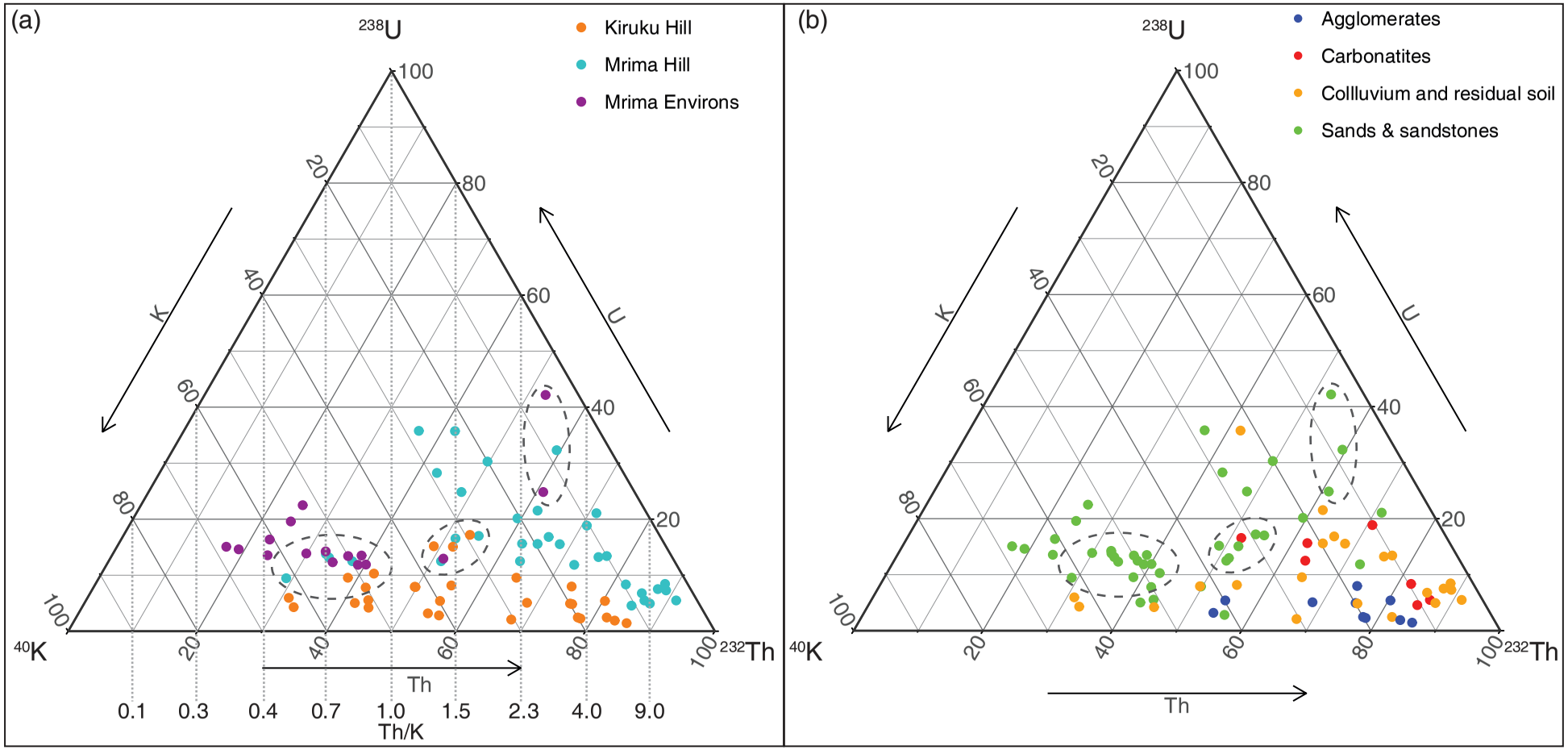

Fig. 5.25: Ternary diagram of percent relative activity concentrations of ^{40}K, ^{232}Th and ^{238}U in the Mrima-Kiruku complex. Data points are colored according to (a) site location and (b) geology. Activity concentration ratios of Th/K are shown in dotted lines (a); sites with minimal leaching of K are characterized by < 1.0 ratios, whereas sites characterized by > 1.0 ratios indicate intense leaching of K.

5.5.3 PCA of activity concentration values in the Mrima-Kiruku complex and south coast paved road

In Sub-section 5.4.1, it was shown that soil samples collected at Menzamwenye paved road shoulder and southern foothills of Mrima Hill contained enhanced concentrations of elements associated with monazite [(Ce, La, Nd, Th)(PO_4, SiO_4)]. The Th/La, Th/Ce and Th/Nd ratios in both samples were found to be comparable suggesting that murram roadbeds on the contaminated section of the south coast paved road and side road intersections may have been sourced from the Mrima Hill area.

The Mrima-Kiruku complex PCA model was used to evaluate the provenance of murram roadbeds in areas identified with HBR anomaly (> 450 nGy h^{-1}), see Fig. 5.22. This data-set used consists of a matrix $X_{92\times3}$ in which the rows (92) correspond to surveyed sites of the Mrima-Kiruku complex (79) together with sites identified with HBR anomaly along the south coast paved road (13), and columns (3) correspond to activity concentrations of ^{40}K, ^{238}U and ^{232}Th.

From the PCA bi-plot shown in Fig. 5.26, ^{238}U and ^{232}Th have the highest contribution to PC1 (52.4%) variance, which is used in the sites classification. It may be observed that all the south coast paved road sites are clustered together with those from Mrima Hill, along PC1. The Gazi, Bwiti and Mwangwei junction sites are closely associated with the southern foothills of Mrima Hill. The Ramisi and Mrima TM junction sites are closely associated with the Mrima Hill slopes, while the Menzamwenye site is associated with the Mrima paved road sites. Based on the results, there is reasonable indication to conclude that the murram used as an aggregate material in paving the south coast paved road section from Gazi toward Lunga Lunga town could have originated from the various murram pits earlier reported by Baker (1953) and Patel (1991), that are located along the hill slopes and southern base of Mrima Hill.

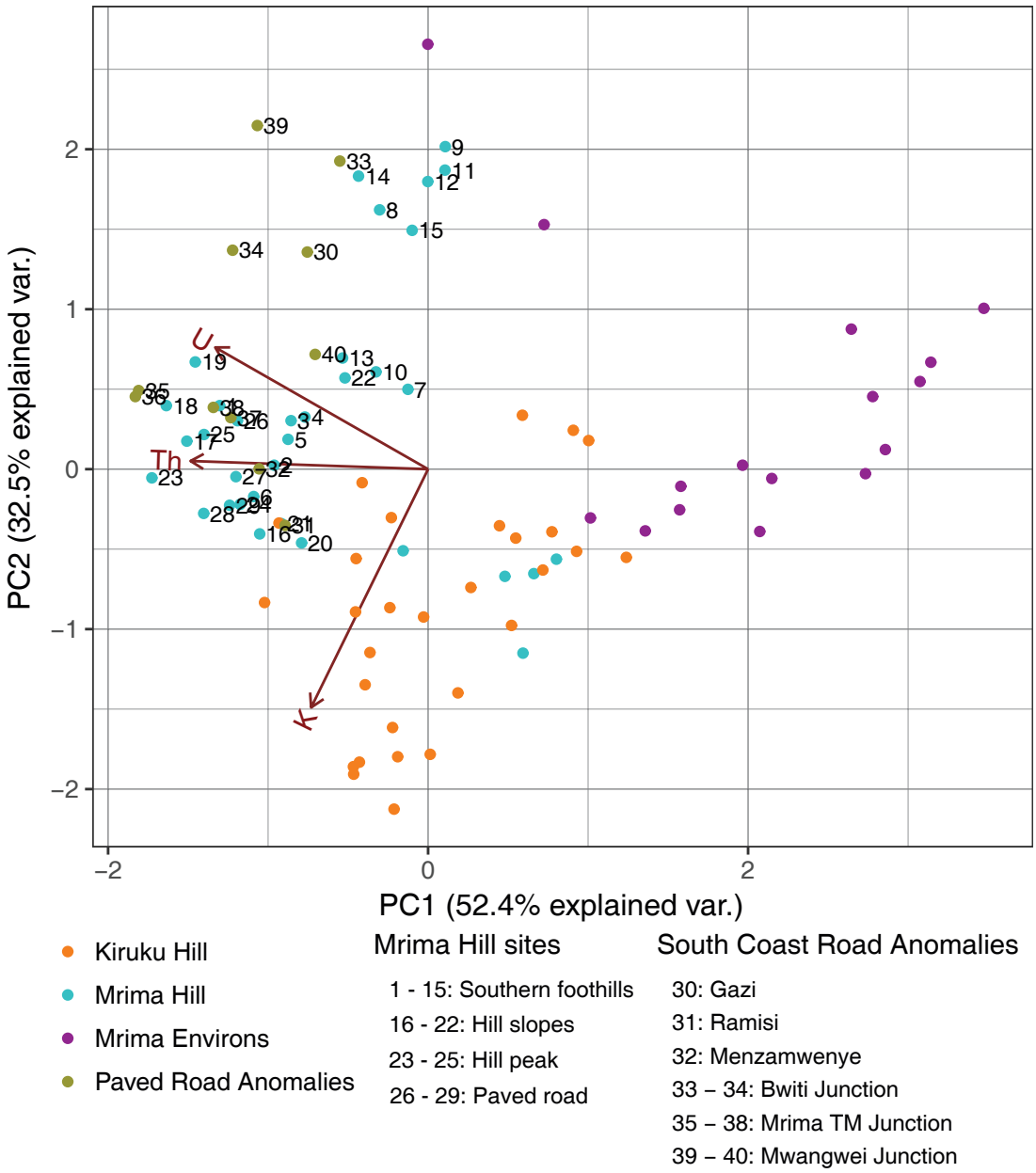

Fig. 5.26: PCA bi-plot of activity concentration values in the Mrima-Kiruku complex and sites identified with the highest natural radioactivity anomalies along the south coast paved road.

Chapter 6

Conclusions and Recommendations

This chapter presents the summary of the *in-situ* $\gamma-$ray survey and associated radiometric measurements (EDXRF spectrometry) carried out in the Mrima-Kiruku complex and the adjoining environs, and the important findings drawn from the objectives of the study. Finally, recommendations and suggestions for future work are given.

6.1 Summary and conclusions

A wide-ranging *in-situ* (carborne and mobile backpack) radiometric survey and mapping, to investigate and accurately delineate the HBR anomaly in the Mrima-Kiruku complex and adjoining environs, has been realized utilizing GPS equipped portable *in-situ* γ-ray spectrometers and GIS software. The survey covered over 70 km of the south coast paved road and its adjoining environs and over 28 km^2 of the Mrima-Kiruku complex area. A novel geospatial gating approach and multivariate exploratory analysis techniques were employed to effectively represent and analyze the *in-situ* radiometric measurements. Furthermore, a total of 31 geological samples (19 soil, 5 sediment, and 7 rock) were collected for laboratory EDXRF analysis in order to complement the *in-situ* radiometric measurements and to enable ascertain the mineralogy of the study area.

The principle findings in the present study are as follows:

The ranges for absorbed gamma dose-rates measured in air along the south coast paved road section and the adjoining environs from Gazi (Mukurumudzi river bridge approach) to the Menzamwenye road junction (past Mrima TM center) and the Mrima-Kiruku complex were < 20 - 1231 and 36 - 2368 nGy h^{-1}, respectively. Dose-rates in the south coast paved road and its adjoining environs were found to generally increase with proximity to the main road implying that the underlying murram roadbed contains elevated NORM levels and that the murram had been ferried from elsewhere. The spatial variability in measured dose-rates within the Mrima-Kiruku complex was found to correspond mainly with the underlying geology, with increments observed toward the Mrima and Kiruku Hill summits, implying that the complex is a geogenic HBR anomaly.

The mean activity concentrations of ^{40}K, ^{238}U and ^{232}Th measured in the south coast paved road and adjoining environs ranged < 202 - 281±17 Bq kg^{-1}, 54±7 - 900±20 Bq kg^{-1} and 54±8 - 892±21 Bq kg^{-1} respectively. It was found that the activity concentrations of ^{232}Th in the Mrima-Kiruku complex are generally higher than those of ^{40}K and ^{238}U: The means of ^{40}K, ^{238}U and ^{232}Th ranged 235±19 - 603±28 Bq kg^{-1}, 68±6 - 326±24 Bq kg^{-1} and 386±12 - 1817±51 Bq kg^{-1} respectively. Correlation analysis of the measured activity concentration values and absorbed gamma dose-rates in air indicated that the anomalous dose-rate values are due to elevated levels of ^{238}U and ^{232}Th in the murram roadbeds underlying the main road and the side-road intersections, and elevated levels of ^{232}Th in the soil and rocks of the Mrima-Kiruku complex. From an external dose perspective, there is significant radiological hazard (> 1 mSv/y) to merchants operating businesses in contaminated areas along the south coast paved road, as well as inhabitants of the Mrima-Kiruku complex area, particularly those who reside at the foothills of both Mrima and Kiruku Hills.

Assessment of EDXRF analysis results showed that soil samples collected along the south coast paved road and adjoining environs contained higher sand content (mean concentrations of Si ranged 29.7±0.4 - 44.2±0.5 %) compared to the Mrima-Kiruku

complex samples (mean concentrations of Si ranged 3.7±0.1 - 34.1±0.5 %). Furthermore, the Mrima-Kiruku complex samples were found to contain enhanced concentrations of Nb, Fe, Th and LREEs which can be attributed to carbonatites and lateritic soil associated with the Mrima and Kiruku Hills. The mean concentration of LREEs, Th and U in these soils ranged < 5 μg g^{-1} - > 10 % with a general increment observed toward the summits. A high correlation of monazite constituent elements i.e. Ce, La, Nd and Th was found between the south coast paved road shoulder and the Mrima foothills soil samples which indicates that the murram used in paving the south coast road could have originated from the Mrima Hill area. Ground based *in-situ* γ-ray spectrometry results and EDXRF analysis of soil samples were found to correlate significantly especially for K ($R^2 = 0.89$) and Th ($R^2 = 0.95$). The poor correlation observed for U ($R^2 = 0.22$) was attributed mainly to disequilibrium in the U decay series.

Exploratory analysis of the activity concentration values by PCA and ternary plots enabled the multivariate assessment of the variability of natural radionuclide concentrations in greater detail across the study area. It was found that the spatial variability of the HBR anomaly along the south coast paved road and the Mrima-Kiruku complex is mainly constrained by anthropogenic activities, underlying geology and geochemical processes in the terrestrial environment. It was also found that there is reasonable indication to conclude that the murram could have originated from the various pits that are located along the hill slopes and southern base of Mrima Hill.

6.2 Recommendations and suggestions for future work

A more comprehensive survey is recommended to complete the radiological characterization of the Mrima-Kiruku complex. This would provide a current geo-referenced radiological map of the area and an updated base-line for NORM. At the time of the study, most of the areas in the complex were inaccessible due to dense vegetation and forest. Additional studies such as investigation of the dispersion of ^{238}U and its progenies in the trading centres located along the south coast paved road are highly desirable in order to evaluate environmental effects associated with use of NORM contaminated murram for road construction. Nonetheless, the preliminary results obtained in this study can be considered as base-line values for radiation exposure and natural radionuclide concentrations in the Mrima-Kiruku complex. The information may be used to assess changes in the natural background levels as a result of geological, climatic and anthropogenic activities such as mining in the area. Furthermore, the findings of this work are useful to inform radio-protection policy and regulatory framework for both public and occupational exposures associated with HBRA in Kenya.

Gamma dose-rate maps are likely to be of most use to regulatory authorities especially in areas where gamma radiation hotspots (> 600 nGy h^{-1}) were reported. The maps can also be used as basis for modelling of radiation exposure pathways and impact assessment of NORM in the Mrima-Kiruku complex and trading centres located along the south coast paved road. It is recommended that use of soil and rocks from the Mrima-Kiruku complex, for construction of dwellings and rehabilitation of roads should not be considered safe for local inhabitants. Human settlements in areas located next to south coast paved road and side road intersections as well as the foothills of Mrima and Kiruku Hills should be discouraged. Furthermore, the cost of remediation for the NORM enhanced murram roadbeds on the south coast paved road and side road intersections should be analysed, to include social economic aspects by the National

government and County government of Kwale. The government of Kenya through the Radiation Protection Board should consider reviewing regulation governing exposure to NORM. The regulation should propose controls on the radioactivity associated with building materials as well as mining, so as to limit the radiation exposure associated with HBRA in Kenya.

Analysis of ground water samples from the Mrima-Kiruku complex and Bwiti junction borehole to assess the possibility of elevated ^{226}Ra and ^{222}Rn content is recommended. The degree of weathering in igneous rock samples from Mrima and Kiruku Hills can be ascertained using determined major element concentrations to calculate the chemical indices used to describe weathering, such as the Parker weathering index (Parker, 1970). These indices may be used to study the abundance of natural radio-elements (K, U and Th) in the weathered rocks. Finally, advanced studies related to simulation of homogeneous sources and modelling of lower gamma photon energies especially for ^{238}U progenies utilizing Monte Carlo techniques are highly desirable. The models may be used to improve efficiency calibration of the portable *in-situ* gamma-ray spectrometers.

References

Aage, H. K. and Korsbech, U. (2003). Search for lost or orphan radioactive sources based on NaI gamma spectrometry. *Appl. Radiat. Isot.*, **58(1)**:103–113.

Aage, H. K., Korsbech, U., Bargholz, K. and Hovgaard, J. (2006). Carborne gamma-ray spectrometry. calibration and applications. *Appl. Radiat. Isot.*, **64(8)**:948–956.

Abbaspour, M., Moattar, F., Okhovatian, A. and Sadeghi, M. K. (2010). Relationship of soil terrestrial radionuclide concentrations and the excess of lifetime cancer risk in western Mazandaran province, Iran. *Radiat. Prot. Dosim.*, **ncq**:187.

Achola, S. O. (2009). Radioactivity and elemental analysis of carbonatite rocks from parts of Gwasi area, south-western Kenya. MSc thesis, University of Nairobi (unpublished).

Achola, S. O., Patel, J. P., Mustapha, A. O. and Angeyo, H. K. (2012). Natural radioactivity and external dose in the high background radiation area of Lambwe East, Southwestern Kenya. *Radiat. Prot. Dosim.*, **152(4)**:423–428.

Adams, J. A. and Weaver, C. E. (1958). Thorium-to-uranium ratios as indicators of sedimentary processes: example of concept of geochemical facies. *AAPG Bull.*, **42(2)**:387–430.

Ahmed, M., Das, S., Haydar, M., Bhuiyan, M., Ali, M. and Paul, D. (2014). Study of natural radioactivity and radiological hazard of sand, sediment, and soil samples from Inani Beach, Cox's Bazar, Bangladesh. *Journal of Nuclear and Particle Physics*, **4(2)**:69–78.

Aitchison, J. (1986). *The Statistical Analysis of Compositional Data*. Chapman and Hall, London.

Anderson, J. and Ingram, J. (1993). *Tropical Soil Biology and Fertility. A Handbook of Methods*. CAB international, Wallingford.

Anspaugh, L. R. (1976). In situ methods for quantifying specific radionuclides. *IEEE Trans. Nucl. Sci.*, **23(3)**:1190–1196.

Astel, A. (2007). Chemometrics based on fuzzy logic principles in environmental studies. *Talanta*, **72(1)**:1–12.

Baker, B. (1953). The alkaline igneous complex of Jombo. Technical Report 24, Mines and Geological Department, Nairobi.

Beamish, D. (2016). *Mapping the terrestrial gamma radiation dose*, chapter 18, pages 235–244. Royal Irish Academy, Dublin.

Beck, H. L., Decampo, J. and Gogolak, C. (1972). In situ Ge(Li) and NaI(Tl) gamma-ray spectrometry. Technical report, Health and Safety Lab, New York.

Beretka, J. and Mathew, P. (1985). Natural radioactivity of Australian building materials, industrial wastes and by-products. *Health Phys.*, **48(1)**:87–95.

Bezuidenhout, J. (2015). *In situ* gamma ray measurements of radionuclides at a disused phosphate mine on the West Coast of South Africa. *J. Environ. Radioact.*, **150**:1–8.

Binge, F. W., Joubert, P. and Mason, J. E. (1966). The Mrima Hill niobium deposit, Coast Province, Kenya. Technical report, Mines and Geology Department, Ministry of Natural Resources, Kenya.

BNL (2015). Decay radiation database. `http://www.nndc.bnl.gov/nudat2/indx_dec.jsp)`. Last accessed: 2015-12-30.

Brereton, R. G. (2003). *Chemometrics: Data Analysis for the Laboratory and Chemical Plant*. John Wiley & Sons, West Sussex.

Bucianti, A., Mateu-Figueras, G. and Pawlowsky-Glahn, V., editors (2006). *Compositional Data Analysis in the Geosciences: From Theory To Practice*. Special Publication No. 264. The Geological Society, London.

Caswell, P. V. (1953). Geology of the Mombasa-Kwale Area. Technical report, Mines and Geology Department, Ministry of Natural Resources, Kenya.

Cesar, M. and Moreira, F. (1991). Radiological survey of Goiânia by a mobile monitoring unit. *Health Phys.*, **60(1)**:81–85.

Chabot, G. (2011). Relationship between radionuclide gamma emission and exposure rate. `https://hps.org/publicinformation/ate/faqs/gammaandexposure.html`. Last accessed: 2017-01-21.

Chan, L., Wong, P. and Chen, Q. (2007). Abundances of radioelements (K, U, Th) in weathered igneous rocks in Hong Kong. *J. Geophys. Eng.*, **4(3)**:285.

Charro, E., Pardo, R. and Peña, V. (2013). Statistical analysis of the spatial distribution of radionuclides in soils around a coal-fired power plant in Spain. *Journal of environmental radioactivity*, **124**:84–92.

Chege, M. W. (2015). *Modelling radon and thoron exhalation and measurement of total natural radiation exposure in Mrima Hill, Kenya*. PhD thesis, Kenyatta University (unpublished).

Cresswell, A. and Sanderson, D. (2009). The use of difference spectra with a filtered rolling average background in mobile gamma spectrometry measurements. *Nucl. Instrum. Methods Phys. Res., Sect. A*, **607(3)**:685–694.

Ćujić, M., Dragović, S., Đorđević, M., Dragović, R., Gajić, B. and Miljanić, Š. (2015). Radionuclides in the soil around the largest coal-fired power plant in Serbia: radiological hazard, relationship with soil characteristics and spatial distribution. *Environ. Sci. and Pollut. Res.*, **22(13)**:10317–10330.

Cullen, T. and Franca, E. P. (1977). International symposium on areas of high natural radioactivity. In *Procos da Calgdes, Brazil, June 16-20, 1975, Proceedings of the symposium published by Academica Brasileira de Cieneias RJ.*

Currie, L. A. (1968). Limits for qualitative detection and quantitative determination: Application to radiochemistry. *Anal. Chem.*, **40(3)**:586–593.

De Meijer, R. and Donoghue, J. (1995). Radiometric fingerprinting of sediments on the Dutch, German and Danish coasts. *Quat. Int.*, **26**:43–47.

De Meijer, R., James, I., Jennings, P. and Koeyers, J. (2001). Cluster analysis of radionuclide concentrations in beach sand. *Appl. Radiat. Isot.*, **54(3)**:535–542.

Debertin, K. and Helmer, R. G. (1988). *Gamma-and X-ray Spectrometry with Semiconductor Detectors*. Elsevier, North-Holland.

Dickson, B. (1990). *Radioelement Distributions in Weathered Granitoids and Aeolian Soils in NSW: AMIRA P263: Improving the Interpretation of Airborne Gamma-ray Surveys*. CSIRO, Division of Exploration Geoscience, North Ryde.

Dickson, B. and Scott, K. (1997). Interpretation of aerial gamma-ray surveys-adding the geochemical factors. *AGSO J. Aust. Geol. Geophys.*, **17**:187–200.

Dragović, S. and Onjia, A. (2006). Classification of soil samples according to their geographic origin using gamma-ray spectrometry and principal component analysis. *Journal of environmental radioactivity*, **89(2)**:150–158.

Dragovic, S. and Onjia, A. (2007). Classification of soil samples according to geographic origin using gamma-ray spectrometry and pattern recognition methods. *Appl. Radiat. Isot.*, **65(2)**:218–224.

Einax, J. W., Zwanziger, H. W. and Geiss, S. (1997). *Chemometrics in Environmental Analysis*. John Wiley & Sons, Weinheim.

Eisenbud, M. and Gesell, T. F. (1997). *Environmental Radioactivity from Natural, Industrial and Military Sources: From Natural, Industrial and Military Sources.* Academic press, San Diego, 4^{th} edition.

Forkapic, S., Maletić, D., Vasin, J., Bikit, K., Mrdja, D., Bikit, I., Udovičić, V. and Banjanac, R. (2017). Correlation analysis of the natural radionuclides in soil and indoor radon in Vojvodina, Province of Serbia. *Journal of Environmental Radioactivity*, **166**:403–411.

Gilmore, G. (2008). *Practical Gamma-Ray Spectroscopy.* John Wiley & Sons, West Sussex, 2^{nd} edition.

GoldenSoftware (2015). A basic understanding of surfer gridding methods - part 1. Technical Report Issue 71.

Grace, H. (1991). Investigations in Kenya and Malawi using as-dug laterite as bases for bituminous surfaced roads. *Geotechnical & Geological Engineering*, **9(3-4)**:183–195.

Grasty, R. and Cox, J. (1997). A carborne gamma-ray spectrometer system for natural radioactivity mapping and environmental monitoring. Technical report.

Harb, S. (2008). Natural radioactivity and external gamma radiation exposure at the coastal Red Sea in Egypt. *Radiat. Prot. Dosim.*, **130(3)**:376–384.

Hashim, N. O., Rathore, I. V. S., Kinyua, A. M. and Mustapha, A. O. (2004). Natural and artificial radioactivity levels in sediments along the Kenyan coast. *Radiat. Phys. Chem.*, **71(3)**:805–806.

Hawkesworth, C., Turner, S., McDermott, F., Peate, D. and Van Calsteren, P. (1997). U-Th isotopes in arc magmas: Implications for element transfer from the subducted crust. *Science*, **276(5312)**:551–555.

Helsel, D. R. *et al.* (2005). *Nondetects and Data Analysis. Statistics for Censored Environmental Data.* John Wiley & Sons, New Jersey.

Hendriks, P., Limburg, J. and De Meijer, R. (2001). Full-spectrum analysis of natural γ-ray spectra. *J. Environ. Radioact.*, **53(3)**:365–380.

Hjerpe, T., Finck, R. R. and Samuelsson, C. (2001). Statistical data evaluation in mobile gamma spectrometry: an optimization of on-line search strategies in the scenario of lost point sources. *Health Phys.*, **80(6)**:563–570.

Horkel, A. D., Neubauer, W., Niedermayr, G., Okelo, R. E., Wachira, J. K. and Werneck, W. (1984). Notes on the geology and mineral resources of the southern kenyan coast. *Mitt. Österreichische Geologische Gesellschaft*, **77(2)**:151–159.

IAEA (1989). Construction and use of calibration facilities for radiometric field equipment. Technical report, International Atomic Energy Agency. Series No. 309.

IAEA (1990). The use of gamma-ray data to define the natural radiation environment. Technical report, International Atomic Energy Agency. IAEA-TECDOC-566.

IAEA (1997). Sampling, storage and sample preparation procedures for X-ray fluorescence analysis of the environmental materials. Technical report, International Atomic Energy Agency. IAEA-TECDOC-950.

IAEA (2003). Guidelines for radioelement mapping using gamma ray spectrometry data. Technical report, International Atomic Energy Agency. IAEA-TECDOC-1363.

ICRP (2007). The 2007 Recommendations of the International Commission on Radiological Protection. ICRP Publication 103. *Ann. ICRP*, **37(2.4)**:2.

ICRU (1994). *Gamma ray spectrometry in the environment.* ICRU Report 53. International Commission on Radiation Units and Measurements.

ISO (2007). *Measurement of radioactivity in the environment - Soil, Part 2: Guidance for the selection of the sampling strategy, sampling and pre-treatment of samples.* ISO 18589-2:2007. International Standards Organization, Geneva.

Jenkins, R. (1995). *Quantitative X-ray Spectrometry.* CRC Press, New York.

JICA (1993). Report on the mineral exploration in the Mombasa Area Republic of Kenya: Phase III. Technical report, Metal Mining Agency of Japan.

Jobson, J. (2012). *Applied multivariate data analysis: volume II: Categorical and Multivariate Methods*. Springer Science & Business Media, New York.

Kanevski, M., Parkin, R., Pozdnukhov, A., Timonin, V., Maignan, M., Demyanov, V. and Canu, S. (2004). Environmental data mining and modeling based on machine learning algorithms and geostatistics. *Environmental Modelling & Software*, **19(9)**:845–855.

Karlsson, S., Mellander, H., Lindgren, J., Finck, R. and Lauritzen, B. (2000). *RESUME 99. Rapid Environmental Surveying Using Mobile Equipment. Report from the NKS/BOK-1.2 project group Mobile Measurements and Measurement Strategies*.

Kebwaro, J. M. (2009). Gamma-ray spectrometric analysis of surface soils around Mrima Hill, using NaI(Tl) detector and decomposition technique. MSc thesis, Kenyatta University (unpublished).

Kebwaro, J. M., Rathore, I. V. S., Hashim, N. O. and Mustapha, A. O. (2011). Radiometric assessment of natural radioactivity levels around Mrima Hill, Kenya. *Int. J. Phys. Sci.*, **6(13)**:3105 – 3110.

Kessaratikoon, P., Boonkrongcheep, R., Choosiri, N., Taehdeng, N. and Udomsomporn, S. (2015). Specific activities of natural radionuclides in beach sand samples from Samila beach in Songkhla Province (Thailand) after nuclear power plant accident in Japan. *International Journal of Environmental Science and Development*, **6(9)**:706.

Klusoň, J. and Thinova, L. (2011). Contribution of atmospherical radon to in-situ scintillation gamma spectrometry data. *Appl. Radiat. Isot.*, **69(8)**:1143–1145.

Knoll, G. (2010). *Radiation Detection and Measurement*. John Wiley & Sons, New York, 4^{th} edition.

Kobayashi, S., Shinomiya, T., Kitamura, H., Ishikawa, T., Imaseki, H., Oikawa, M., Kodaira, S., Miyaushiro, N., Takashima, Y. and Uchihori, Y. (2015). Radioactive contamination mapping of northeastern and eastern Japan by a car-borne survey system, Radi-Probe. *J. Environ. Radioact.*, **139**:281–293.

Kock, P. and Samuelsson, C. (2011). Comparison of airborne and terrestrial gamma spectrometry measurements-evaluation of three areas in southern Sweden. *J. Environ. Radioact.*, **102(6)**:605–613.

Laedermann, J.-P., Byrde, F. and Murith, C. (1998). In-situ gamma-ray spectrometry: the influence of topography on the accuracy of activity determination. *J. Environ. Radioact.*, **38(1)**:1–16.

Landa, E. R. (2007). Naturally occurring radionuclides from industrial sources: characteristics and fate in the environment. *Radioactivity in the environment*, **10**:211–237.

L'Annunziata, M. F. (2003). *Handbook of Radioactivity Analysis*. Elsevier, Amsterdam, 3^{rd} edition.

Loupekine, I. (1968). Status of development of certain non-metals and minerals in Kenya: Submitted to the United Nations Economic and Social Council. Technical Report, Deparment of Geology, University of Nairobi.

Luxin, W., Yongru, Z., Zufan, T., Weihui, H., Deqing, C. and Yongling, Y. (1990). Epidemiological investigation of radiological effects in high background radiation areas of Yangjiang, China. *J. Radiat. Res.*, **31(1)**:119–136.

Macdonald, J., Smith, P. and Assinder, D. (1996). The development and use of an *in situ* gamma-ray spectrometry system in North Wales. *J. Radiol. Prot.*, **16(2)**:115.

Maina, D. N. (2008). Measurements of heavy metals and natural radioactivity levels in soils around the titanium mining site in Kwale district. MSc thesis, University of Nairobi (unpublished).

Mangala, M. J. (1987). Multi-elemental EDXRF analysis of Kerio Valley fluorite ores and Mrima Hill soil sediments. MSc thesis, University of Nairobi (unpublished).

McCall, G. J. (1958). Geology of the Gwasi Area. Technical report.

Melville, C., Wai, C., Collopy, M. and Willmes, H. (1981). Uranium dispersion along roads paved with phosphate slag. *Bull. Environ. Contam. Toxicol.*, **27(1)**:470–473.

Miller, K. M. and Shebell, P. (1993). In situ gamma-ray spectrometry: A tutorial for environmental radiation scientists. Technical Report, USDOE Environmental Measurements Lab., New York, NY (United States).

Mohanty, A., Sengupta, D., Das, S., Saha, S. and Van, K. (2004). Natural radioactivity and radiation exposure in the high background area at Chhatrapur beach placer deposit of Orissa, India. *J. Environ. Radioact.*, **75(1)**:15–33.

Mustapha, A. O. (1999). *Natural radioactivity levels in Kenya.* PhD thesis, University of Nairobi (unpublished).

Navas, A., Gaspar, L., López-Vicente, M. and Machín, J. (2011). Spatial distribution of natural and artificial radionuclides at the catchment scale (South Central Pyrenees). *Radiat. Meas.*, **46(2)**:261–269.

NCRP (1976). *Environmental radiatiion measurements. NCRP report no. 50.* National Council on Radiation Protection.

Nilsson, J. M., Östlund, K., Söderberg, J., Mattsson, S. and Rääf, C. (2014). Tests of HPGe-and scintillation-based backpack γ-radiation survey systems. *J. Environ. Radioact.*, **135**:54–62.

NIST (2004). X-ray mass attenuation coeefficients. `http://physics.nist.gov/PhysRefData/XrayMassCoef/ComTab/air.html)`. Last accessed: 2015-11-30.

O'Brien, R. and Cooper, M. (1998). Technologically enhanced naturally occurring radioactive material (NORM): pathway analysis and radiological impact. *Appl. Radiat. Isot.*, **49(3)**:227–239.

Okeji, M. C., Agwu, K. K. and Idigo, F. U. (2012). Assessment of natural radioactivity in phosphate ore, phosphogypsum and soil samples around a phosphate fertilizer plant in Nigeria. *Bull. Environ. Contam. Toxicol.*, **89(5)**:1078–1081.

Osoro, M. K., Rathore, I. V. S., Mangala, M. J. and Mustapha, A. O. (2011). Radioactivity in surface soils around the proposed sites for titanium mining project in Kenya. *Journal of Environmental Protection*, **2**:460–464.

Otwoma, D. (2012). *An investigation of the radioecology of the carbonatite deposits in the Homa Mountain region in South Nyanza, Kenya*. PhD thesis, University of Nairobi (unpublished).

Otwoma, D., Patel, J. P., Bartilol, S. K. and Mustapha, A. O. (2013). Estimation of annual effective dose and radiation hazards due to natural radionuclides in mount homa, southwestern kenya. *Radiat. Prot. Dosim.*, **155(4)**:497–504.

Ouseph, P. J. (1975). *Introduction to Nuclear Radiation Detectors*. Plenum Press, New York, 1^{st} edition.

Parker, A. (1970). An index of weathering for silicate rocks. *Geol. Mag.*, **107(06)**:501–504.

Paschoa, A. S. (1998). Potential environmental and regulatory implications of naturally occurring radioactive materials (NORM). *Appl. Radiat. Isot.*, **49(3)**:189–196.

Patel, J. P. (1991). Environmental radiation survey of the area of high natural radioactivity of Mrima hill of Kenya. *Discovery and Innovation*, **3(3)**:31–35.

PEI (2010). AGRS1 Portable Spectrometer Calibration Program User Manual. Technical Report, Pico Envirotec Inc.

PEI (2013a). PEICore and PGIS-2 operation manual. Technical report, Pico Envirotec Inc.

PEI (2013b). Praga 4 tutorial and user guide. Technical report, Pico Envirotec Inc.

PEI (2015). Detection limits in PEI's gamma-ray spectrometric airborne/ground systems. Technical report, Pico Envirotec Inc.

Podgorsak, E. B. (2010). *Radiation Physics for Medical Physicists*. Springer-Verlag, Berlin Heidelberg, 2^{nd} edition.

Reimann, C. and Filzmoser, P. (2000). Normal and lognormal data distribution in geochemistry: death of a myth. consequences for the statistical treatment of geochemical and environmental data. *Environ. Geol.*, **39(9)**:1001–1014.

Rostron, P. D., Heathcote, J. A. and Ramsey, M. H. (2014). Optimising in situ gamma measurements to identify the presence of radioactive particles in land areas. *J. Environ. Radioact.*, **138**:162–169.

Sahoo, S. K., Hosoda, M., Kamagata, S., Sorimachi, A., Ishikawa, T., Tokonami, S. and Uchida, S. (2011). Thorium, uranium and rare earth elements concentration in weathered Japanese soil samples. *Progress in Nuclear Science and Technology*, **1**:416–419.

Sam, A. K., Ahamed, M. M., El Khangi, F., El Nigumi, Y. and Holm, E. (1998). Radioactivity levels in the Red Sea coastal environment of Sudan. *Mar. Pollut. Bull.*, **36(1)**:19–26.

Sanderson, D., Cresswell, A. and Lang, J. (2002). An international comparison of airborne and ground based gamma ray spectrometry. *Results of the ECCOMAGS*.

Sohrabi, M. (1993). Recent radiological studies of high level natural radiation areas of Ramsar. In *Proceeding of International Conference on High Levels of Natural Radiations*, volume 3, pages 39–47.

Sohrabi, M. (1998). The state-of-the-art on worldwide studies in some environments with elevated naturally occurring radioactive materials (NORM). *Appl. Radiat. Isot.*, **49(3)**:169–188.

Sohrabi, M. (2013). World high background natural radiation areas: Need to protect public from radiation exposure. *Radiat. Meas.*, **50**:166–171.

Spectro (2000). Documentation of SPECTRO X-LAB: Basic Principles of EDXRF. Technical Report, Spectro Analytical Instruments, GmbH.

Sunta, C. (1993). A review of the studies of high background areas of the SW coast of India. In *Proceedings of the International Conference on High Levels of Natural Radiation, Ramsar, IAEA*, pages 71–86.

Tsikritzis, L. (2005). Chemometrics of the distribution and origin of ^{226}Ra, ^{228}Ra, ^{40}K and ^{137}Cs in plants near the West Macedonia Lignite Center (Greece). *Journal of radioanalytical and nuclear chemistry*, **264(3)**:651–656.

Tsujimoto, T. (1988). A comparison between in-situ and sampling methods for the determination of radionuclides in soil. *J. Radiat. Res.*, **29(4)**:229–237.

Tyler, A. N. and Copplestone, D. (2007). Preliminary results from the first national *in situ* gamma spectrometry survey of the United Kingdom. *J. Environ. Radioact.*, **96(1)**:94–102.

UNSCEAR (2000). *Sources and Effects of Ionizing Radiation. Report to the General Assembly, with scientific annexes*, volume 1 of *Report to the General Assembly with scientific annexes*. United Nations Publications.

UNSCEAR (2008). *Effects of Ionizing Radiation: Report to the General Assembly, with scientific annexes*, volume Vol I. United Nations Publications.

van Grieken, R. and Markowicz, A. (2001). *Handbook of X-ray Spectrometry*, volume 2. Marcel Dekker, New York.

van Velzen, L., editor (2015). *Environmental Remediation and Restoration of Contaminated Nuclear and NORM sites*. Number 71 in Woodhead Publishing Series in Energy. Elsevier, Cambridge.

Varmuza, K. and Filzmoser, P. (2016). *Introduction to Multivariate Statistical Analysis in Chemometrics*. CRC press, Florida.

Veiga, R., Sanches, N., Anjos, R., Macario, K., Bastos, J., Iguatemy, M., Aguiar, J., Santos, A., Mosquera, B., Carvalho, C. *et al.* (2006). Measurement of natural radioactivity in Brazilian beach sands. *Radiat. Meas.*, **41(2)**:189–196.

Verplanck, P. L. and van Gosen, B. S. (2011). Carbonatite and alkaline intrusion-related rare earth element deposits–a deposit model. Technical report, US Geological Survey.

Webster, R. and Oliver, M. A. (2007). *Geostatistics for Environmental Scientists*. John Wiley & Sons, West Sussex.

Wenning, R. and Erickson, G. (1994). Interpretation and analysis of complex environmental data using chemometric methods. *TrAC, Trends Anal. Chem.*, **13(10)**:446–457.

Wilford, J., Bierwirth, P. and Craig, M. (1997). Application of airborne gamma-ray spectrometry in soil/regolith mapping and applied geomorphology. *AGSO Journal of Australian Geology and Geophysics*, **17(2)**:201–216.

Appendix A

Calibration Data

A.1 Calibration of PGIS-2 spectrometers on transportable pads

PGIS-128 detector on a 1 × 1 × 0.3 m background calibration pad.

PGIS-21 detector on a 1 × 1 × 0.3 m thorium calibration pad.

Fig. A.1: Calibration of PGIS-2 spectrometers on transportable pads. The PGIS-2 spectrometers were calibrated by taking 600 s measurements on transportable concrete calibration pads containing known K, Th and U concentrations and a fourth pad which served as background.

Table A.1: Concentrations of K, U and Th in transportable calibration pads

Pad	K (%)	eU (ppm)	eTh (ppm)	Density (g cm^{-3})
Blank	1.23±0.01	0.810±0.04	1.95±0.05	2.28
K	6.42±0.04	1.05±0.09	1.17±0.09	2.23
U	1.23±0.01	42.47±0.27	1.95±0.05	2.28
Th	1.23±0.01	1.46±0.15	103.6±1.41	2.28

Table A.2: Energy window sensitivities calculated for PGIS-2 spectrometers

Sensitivities	K window		U window		Th window	
	PGIS-128	PGIS-21	PGIS-128	PGIS-21	PGIS-128	PGIS-21
cps per 1% K	20.283	3.427	1.226	0.262	0.400	0.084
cps per 1 ppm eU	0	0	1.686	0.303	0.315	0.067
cps per 1 ppm eTh	0	0	0.083	0.011	0.945	0.144

Table A.3: Stripping ratios calculated for PGIS-2 spectrometers

	PGIS-128		PGIS-21	
	Ratio of sensitivities	Stripping ratios	Ratio of sensitivities	Stripping ratios
α	0.315/0.945	0.3329±0.0049	0.067/0.144	0.4629±0.0106
β	0.400/0.945	0.4236±0.0126	0.084/0.144	0.5815±0.0239
γ	1.226/1.686	0.7275±0.0101	0.262/0.303	0.8667±0.0321
a	0.083/1.686	0.0491±0.0026	0.011/0.303	0.0377±0.0053
$b = g$		0		0

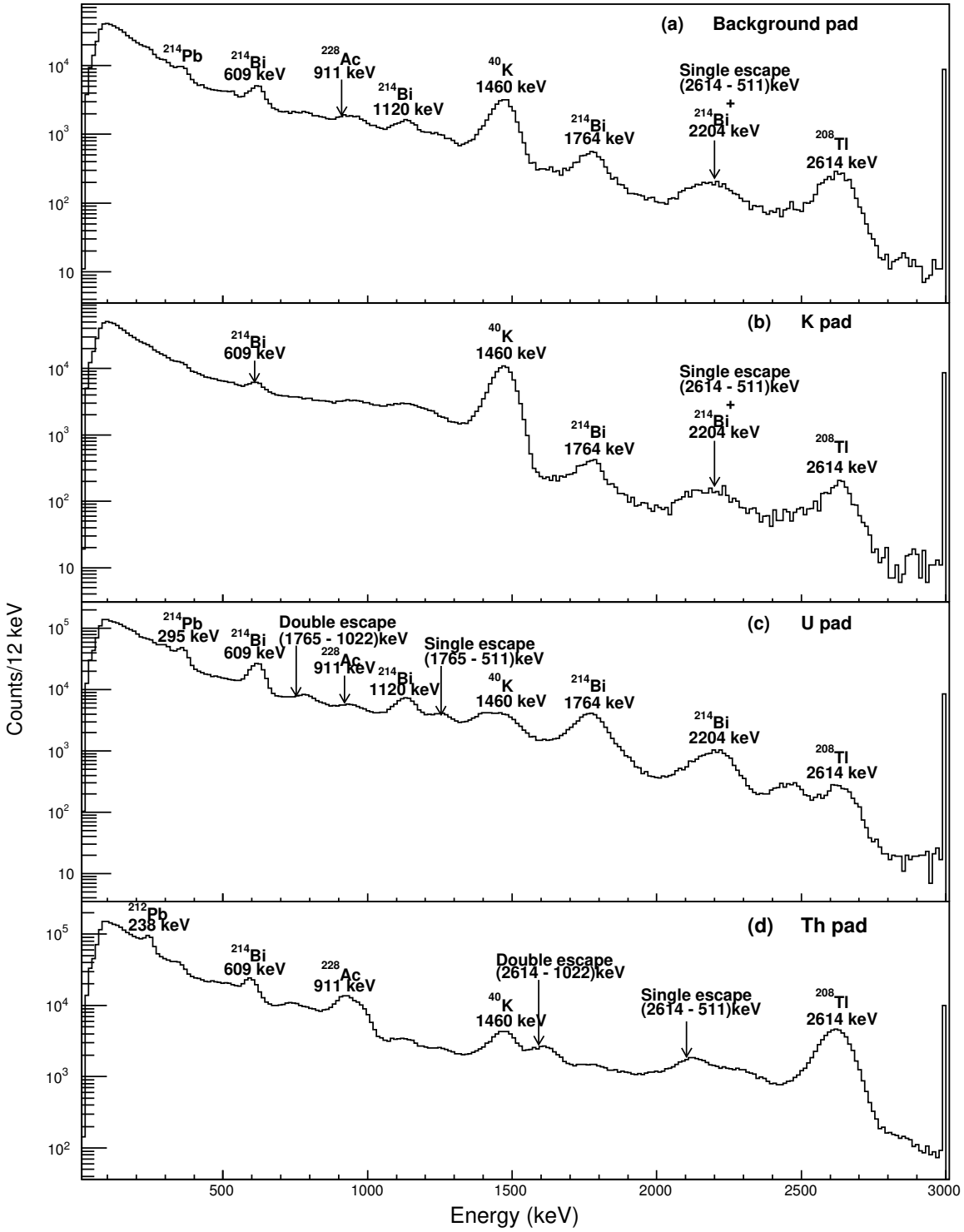

Fig. A.2: Spectra obtained from four calibration pads ^{40}K, ^{232}Th, ^{238}U and background measured with the PGIS-128 spectrometer for 600 s. At high $\gamma-$ray energies, the single and double escape peaks are prominent. Photo peaks are broad due to poor pulse height resolution of the NaI(Tl) detector.

A.2 Gamma dose-rates for a 5 μCi ^{133}Ba source

Eq. A.1 was used for calculation of gamma dose-rates using a 5 μCi ^{133}Ba source at various source-detector distances. ^{133}Ba decay data (Table A.4) and mass energy absorption coefficients used to calculate dose-rates were obtained from BNL National Nuclear Data (BNL, 2015) and NIST Standard Reference Database (NIST, 2004), respectively. Only photons with yields greater than 1% were considered. The fifth energy listed is the average of two closely lying energy peaks (0.2759 and 0.2764 MeV).

$$x = 5.263 \times 10^{-6} A \sum \frac{(y_i E_i \, (\mu_{en}/\rho) \, i)}{r^2} \tag{A.1}$$

where,

x is the dose rate evaluated at each energy

A is activity of the source in Bq

y represents the yield of photons

E is photon energy in MeV

(μ_{en}/ρ) is mass energy absorption coefficient in cm^2/g, for the photons in air

r is distance in cm

Table A.4: ^{133}Ba decay data and mass energy absorption coefficients in air

^{133}Ba γ-Energies	Fractional yield	Interpolated (μ_{en}/ρ)air
0.0123	0.0143	3.1607
0.0532	0.0214	0.0376
0.0796	0.0266	0.0242
0.0810	0.3290	0.0241
0.2759	0.1243	0.0282
0.3029	0.1834	0.0287
0.3560	0.6205	0.0291
0.3838	0.0895	0.0294

Appendix B

Surveyed Areas and Field Samples

B.1 General area of study and map legends

S1. South coast road, Gazi.

S2. Indian Ocean coastline, Munje.

S3. Coastal mangrove, Bodo.

S4. Kwale Sugar Company, Ramisi.

S5. Sand harvesting site, Ramisi.

S6. Overlooking Kiruku Hill from Mrima.

S7. Overlooking Mrima Hill from Bumbuni.

S8. South coast rd, Mwangwei Junction approach.

Fig. B.1: Photography on various sites and locations within the study area.

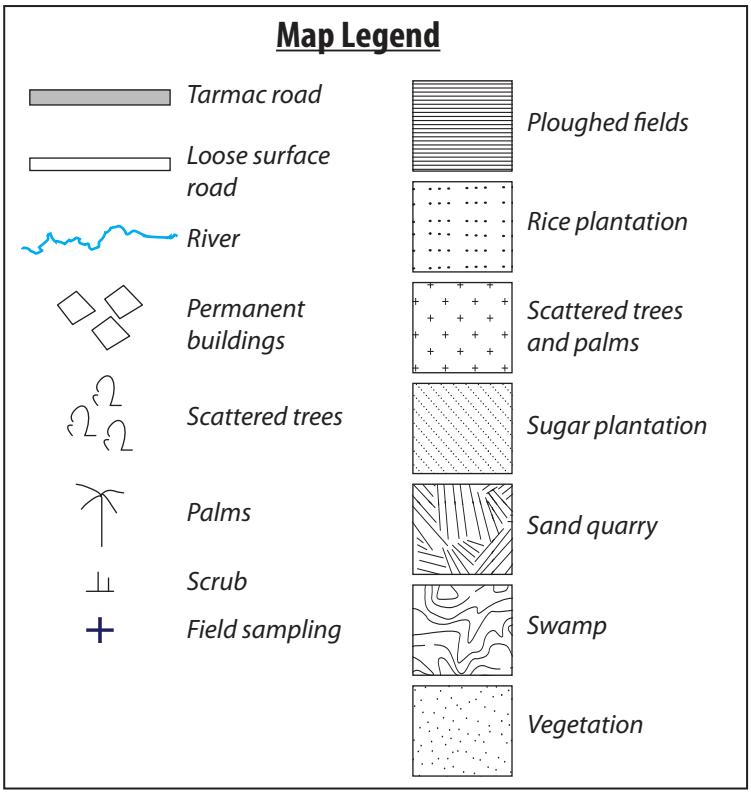

(a)

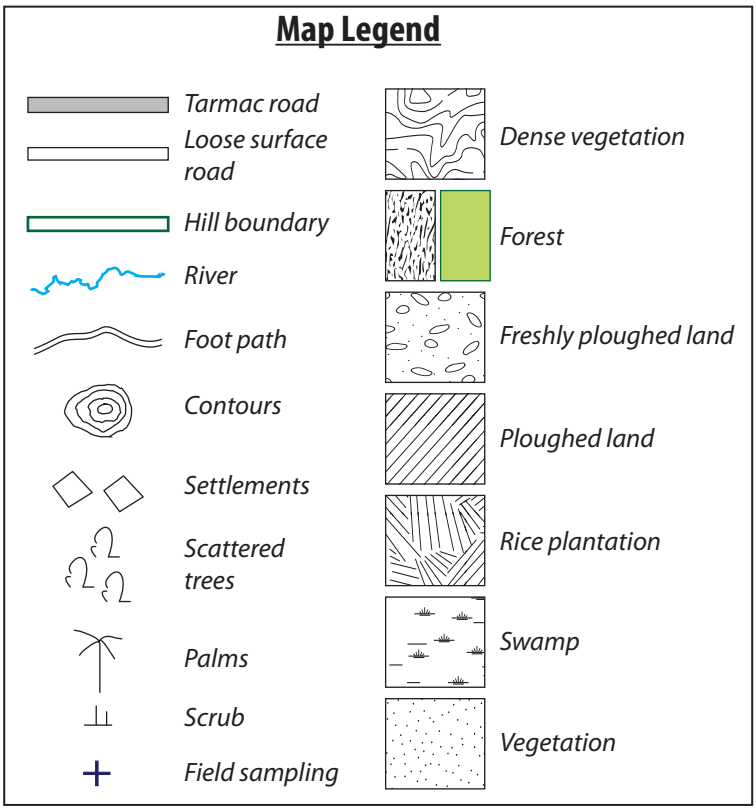

(b)

Fig. B.2: Map legend for (a) the south coast road and environs survey and (b) the alkaline complex of Jombo survey.

B.2 South coast paved road and the environs

South coast paved road, Gazi (Area representing boundary point between background and elevated dose-rates).

South coast paved road toward Ramisi. Illustrating difference between road murram and roadside soil.

Side paved road intersection at Bwiti Junction (gate 07, Fig. 5.4) illustrating weathered tarmac exposing road murram.

Side road (unpaved) intersection at Bwiti Junction (gate 02, Fig. 5.4) illustrating exposed road murram.

Bus stop at Mwangwei Junction (gate 01, Fig. 5.5 a) illustrating weathered tarmac exposing road murram.

Side road intersections at Mwangwei Junction illustrating road murram and human activity i.e. merchandising.

Side paved road intersection at Mrima TM Junction (gate 03, Fig. 5.5 b) illustrating weathered tarmac.

Mrima TM Junction roadside bus stop (gate 01, Fig. 5.5 b) illustrating exposed road murram.

Fig. B.3: Photography of the south coast paved road, side road intersections and roadside features. The murram (laterite) roadbeds were found to contain enhanced levels of ^{238}U and ^{232}Th.

B.3 Mrima and Kiruku Hills and the environs

Mrima Hill. Also illustrated is the proximity of the south coast paved road to the hill.

Kiruku Hill. Also illustrated is the thick undergrowth masking the hill.

Dry weather murram road at the base of Mrima Hill. Also illustrated is the weathering and run-off of top soil.

Rock outcrops and bares soils on Kiruku Hill.

Dry weather murram road in Menzamwenye, east of Mrima Hill. Also illustrated is the difference in soil type.

Kiruku Hill southern and northern rock samples. Also illustrated is weathering on the surfaces.

Height correction measurements for the PGIS-128 gamma spectrometer at the base of Mrima Hill.

Human settlement and land ploughing along the northern hillslopes of Kiruku Hill.

Fig. B.4: Photography on the Mrima and Kiruku Hills and environment features.

B.4 Sample locations and preparations

Table B.1: Field sampling (number of samples are indicated in brackets)

Site	Samples	GPS coordinates
South coast roadsides and adjoining environs		
Ramisi Islamic Centre	Soil (1), swamp sediment (1)	4.519583 °S, 39.412000 °E
Ramisi sand quarry	Quarry sand (1)	4.517639 °S, 39.397556 °E
Bwiti junction	Soil (2)	4.535917 °S, 39.332972 °E
		4.534306 °S, 39.333111 °E
	Soil (1), swamp sediment (1)	4.535250 °S, 39.332861 °E
Bodo	Soil (1), ocean sediment (1)	4.549722 °S, 39.412500 °E
	Ocean rock (1)	
Munje	Soil (1)	4.523528 °S, 39.465139 °E
	Beach sand (1)	4.523556 °S, 39.464806 °E
Mrima-Kiruku complex		
Marenji farm	Soil (1)	4.510611 °S, 39.237972 °E
Menzamwenye road tunnel	Soil (1)	4.489806 °S, 39.218889 °E
Menzamwenye quarry	Rock (1)	4.467833 °S, 39.195806 °E
Bumbuni open field	Soil (1), stream sediment (1)	4.497194 °S, 39.273028 °E
	Soil (1)	4.498194 °S, 39.274861 °E
Ndzovu river	Soil (1), river sediment (1)	4.500889 °S, 39.276639 °E
Bumbuni Mrima homestead	Soil (1)	4.489111 °S, 39.269694 °E
Kiruku Hill	Soil (1), rock (1)	4.468639 °S, 39.294500 °E
	Soil (1), rock (1)	4.467667 °S, 39.295222 °E
	Soil (1), rock (1)	4.467083 °S, 39.295639 °E
	Soil (1), rock (1)	4.466306 °S, 39.296472 °E
	Soil (1), rock (1)	4.462250 °S, 39.294306 °E

Fig. B.5: Laboratory equipment and various sample processing stages.

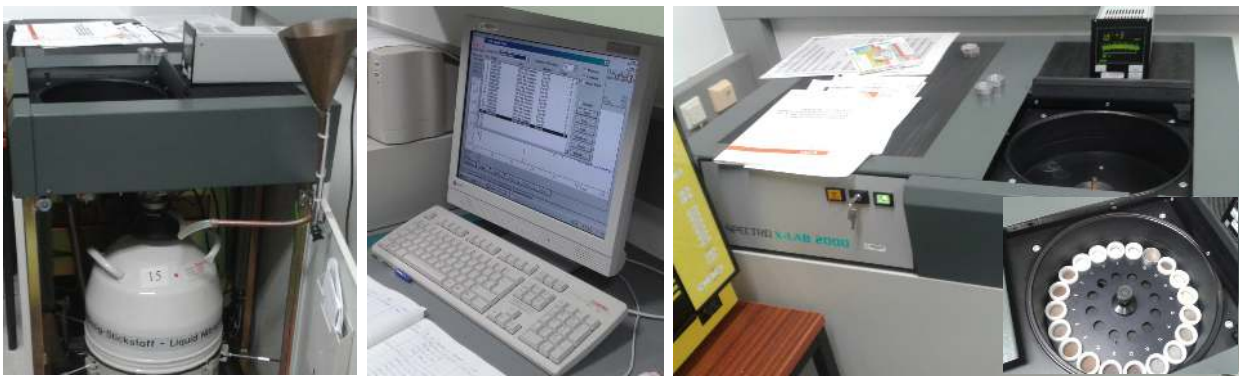

Fig. B.6: Spectro X-lab spectrometer for EDXRF measurements.